The Atmospheric Impact of Energy and Food Production

by

Alexander Gvakharia

A dissertation submitted in partial fulfillment
of the requirements for the degree of
Doctor of Philosophy
(Applied Physics)
in The University of Michigan
2019

Doctoral Committee:

Assistant Professor Eric A. Kort, Chair
Assistant Professor Andrew P. Ault
Associate Professor Mark Flanner
Assistant Professor Gretchen Keppel-Aleks
Professor Richard B. Rood

Alexander Gvakharia

agvak@umich.edu

ORCID iD: 0000-0003-1260-4744

ACKNOWLEDGEMENTS

First and foremost I would like to thank Eric Kort for being a superb mentor and advisor. When I started grad school I never imagined my research would involve flying around the country to tackle some of the most important problems the world faces today. The amazing opportunities and guidance Eric has provided over the past five years have been critical for my development as a scientist and thinker. I also want to thank the rest of my committee, Andrew Ault, Mark Flanner, Gretchen Keppel-Aleks, and Richard Rood for all their advice and insight.

I am honored to have worked with so many brilliant collaborators and colleagues. I want to thank Colm, Jeff, Tim, Sonja, and all the excellent NOAA Corps pilots. I also want to thank Steve, Jason, Justin, Josh, and everyone else at Scientific Aviation. Also thanks to Mark, Dave, Barry, Mike, and the rest of Aerodyne Research Inc. for their training and troubleshooting. And of course, thanks to all my groupmates, John, Mackenzie, Kim, Sharon, Emily, Martin, Genny, Alan, Yaoxian, and Daniel.

I want to recognize all the teachers in my life, from kindergarten through higher education. Their patience and dedication helped me foster a lifelong love of learning, and for that I will be forever grateful.

I am blessed to have so many incredible friends, in grad school and elsewhere. I'd like to thank my friends from Virginia, Tbilisi, North Carolina, the whole SI 2012 cohort, friends in Chicago, my friends from Detroit, California, from the West Coast to the whole East, from D.C. and down in Maryland, all over the whole globe.

I want to thank the Sutherland family for welcoming me as one of their own. I

want to thank my family in Georgia, my aunts, uncles, and cousins for all their love and encouragement despite being so far away. I'd like to thank Nick for being a wonderful brother and friend. I will never be able to sufficiently thank my parents Ira and Aka for all that they sacrificed to give me and my brother opportunities they never had. And of course, I want to thank my absolutely fantastic wife Lindsay. I could not have made it this far without her love and support.

TABLE OF CONTENTS

LIST OF FIGURES

Figure

LIST OF TABLES

Table

ABSTRACT

Fossil fuel extraction and modern industrial agricultural practices both emit greenhouse gases and pollutants, including methane (CH_4), nitrous oxide (N_2O), ethane (C_2H_6), and black carbon (BC). Our understanding of emissions magnitudes, processes that control these emissions, and expected future emissions behavior from these sources and of these important atmospheric compounds have large uncertainty. Accurate, precise measurements made from aircraft can provide essential insights into emissions and their impact on climate and air quality. This thesis presents airborne observations using high-precision spectroscopy of atmospheric greenhouse gases and pollutants to quantify emissions. First, with airborne measurements we assess natural gas flaring efficiency of CH_4, C_2H_6, and BC in the Bakken Shale region of North Dakota. We discover emissions from flares exhibit a heavy-tailed distribution and superemitter behavior with a small number of inefficient flares dominating the total source. This skewed distribution translates to total flaring emissions of CH_4 and C_2H_6 that are 2.5 times higher than if standard flare efficiency is assumed. While we observe a skewed distribution for BC, emissions are lower than previous estimates and there is no significant correlation with CH_4 emissions. Next, we describe the development and evaluation of an airborne system using an N_2O, CO_2, CO, and H_2O laser spectrometer. Ambient pressure-related artifacts in the instrument are corrected for with a mass flow-controlled frequent calibration technique to achieve an 88% duty cycle with high precision and accuracy. The resultant flight system represents the current state-of-the-art airborne N_2O system. Finally, with this new system and

a series of flights, emissions from agricultural activity and fertilizer production are evaluated in the Lower Mississippi River Basin. The quantification of emission rates from two productive fertilizer plants finds good agreement with reported emissions of N_2O and CO_2, but a large underestimation in CH_4, suggesting significant natural gas leakage. We calculate N_2O emissions fluxes from cropland using the airborne mass balance technique, a first application of this method for N_2O. The impact on emissions by associated factors—crop type, fertilizer application, soil moisture, and soil temperature—is investigated. We find the strongest predictors in a multiple linear regression are soil moisture and crop type. An average early-growing season N_2O flux of 1.8±1.4 g N_2O-N ha^{-1} hr^{-1} is quantified for the region. The results demonstrate the ability to evaluate N_2O emissions at regional scales from sources with large environmental heterogeneity using airborne observations. This thesis highlights the utility of aircraft measurements for investigating emissions of greenhouse gases and pollutants at varying spatial scales and from diverse sources associated with energy and food production supply chains.

CHAPTER I

Introduction

1.1 Humans, Energy, and Food

The world has seen significant advancements in technology, medicine, science, and international cooperation, especially since the second half of the 20th century (*Rosling et al.*, 2018; *Pinker*, 2018). On average we live longer than our predecessors and enjoy more widespread availability of energy and food. In 1960 the global average life expectancy was 52 years and by 2016 it was 72 years, a 40% increase (*Roser*, 2019; *The World Bank*, 2016b). Over the same period there has been a steady increase in food supply per capita and a decrease in undernourishment, particularly as meat and dairy have become globally more prevalent (*FAO*, 2019). As for energy supply, since 1990 the global share of people with access to electricity has gradually risen from 71% to 87% (*The World Bank*, 2016a). The world's population has grown from ∼4 billion in 1973 to 7.55 billion in 2017, and is projected to reach ∼9.8 billion by 2050 (*United Nations*, 2017). Figure 1.1 shows this consistent growth in global population, energy use, and food supply. Although the global population increased by a factor of 1.88 since 1973, the total annual energy consumption in the world increased by a factor of 2.05 (*IEA*, 2018a; *Ritchie and Roser*, 2019). If energy demand continues at this pace, total consumption is expected to double again by 2050, despite a potential population increase by 1.3 times (*Lewis and Nocera*, 2006). Similarly, the food supply

will have to sustain more mouths at a growing rate. The global expansion of energy and agricultural production has resulted in increased emissions of greenhouse gases (GHGs) and other associated pollutants, which significantly affect the climate and warm the earth's surface (*Myhre et al.*, 2013).

Anthropogenic emissions of GHGs have perturbed the planetary energy balance since pre-industrial times (*Myhre et al.*, 2013; *Prather et al.*, 2013). Three of the most impactful GHGs are carbon dioxide (CO_2), methane (CH_4), and nitrous oxide (N_2O). Since 1750 these three have contributed 88% of the increase in global radiative forcing due to long-lived gases (*Hofmann et al.*, 2006; *Montzka et al.*, 2003). As of 2017 the total radiative forcing from GHGs was an estimated 3.06 W m^{-2}, with CO_2, CH_4, and N_2O contributing 66%, 17%, and 6% respectively (*Butler and Montzka*, 2018). CH_4 and N_2O can experience feedback due to climate change, particularly in the tropics, with rising temperatures causing higher CH_4 emissions from wetlands and rice crops, and higher N_2O emissions from warmer soils (*Tian et al.*, 2015; *Reay et al.*, 2018). Climate change can damage natural resources, displace humans, and pose significant risks to financial security and health. Climate change adversely affects agriculture, harming crop yields and increasing the severity and frequency of extreme weather events (*Lipper et al.*, 2014). The percentage of global undernourishment has actually slightly *risen* in the past three years, following a decade of decline (*Parry et al.*, 2004; *FAO et al.*, 2018). Pollutants that affect air quality and mortality, such as black carbon (BC) and ethane (C_2H_6), have also experienced increased emissions. Higher temperatures, reduced air and food quality, and increased energy demand are just a few of the serious ramifications of climate change (*FAO et al.*, 2018; *Duffy et al.*, 2019; *Haines and Ebi*, 2019). Improved observations of GHGs and pollutants such as CH_4, N_2O, C_2H_6, and BC are valuable for quantifying the magnitude and rate of emissions. A better understanding of emissions can then be used to assess the effectiveness of mitigation policies and develop future climate scenarios.

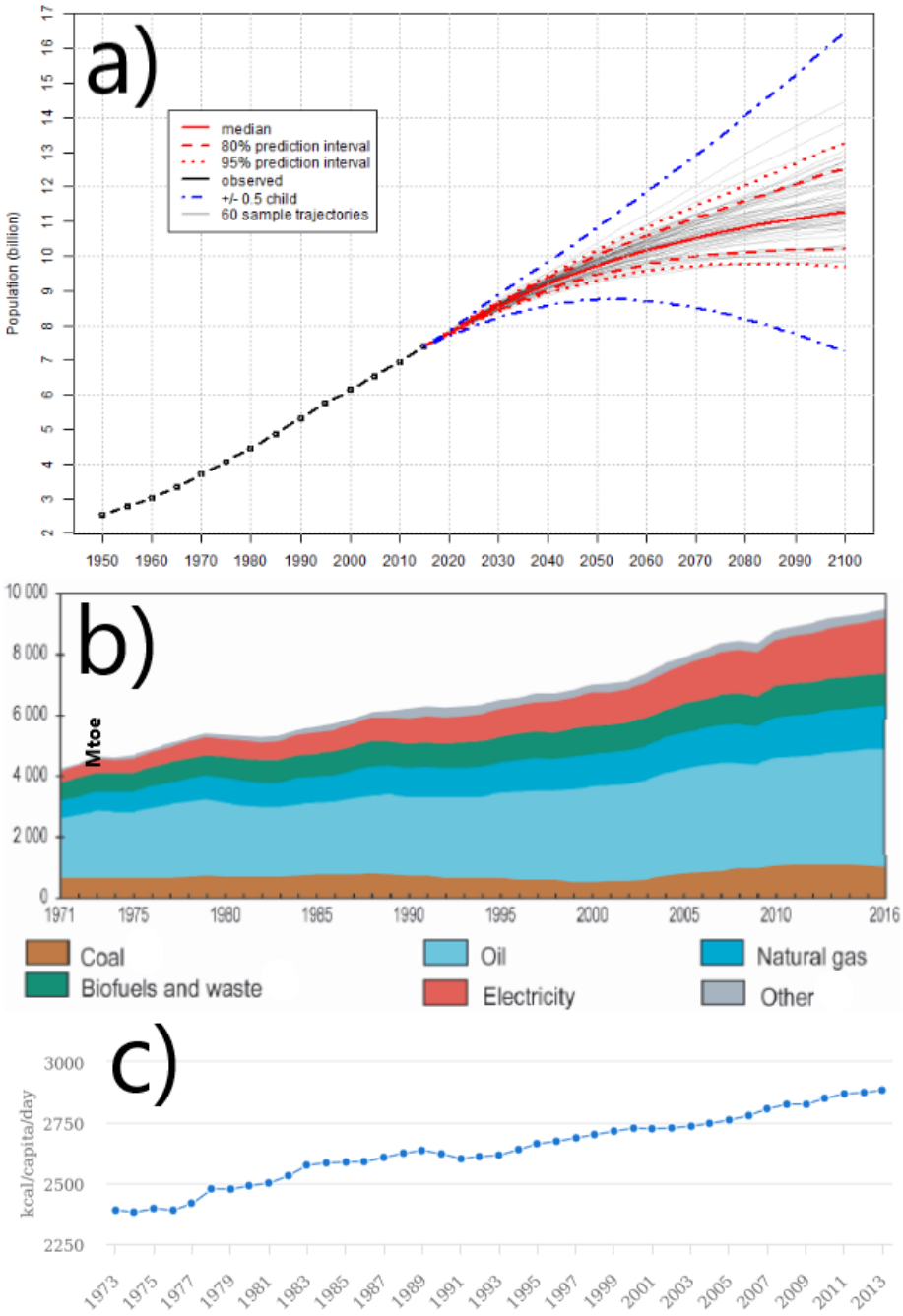

Figure 1.1: Growth in a) global population in billions of people, including projections to 2100, b) energy consumption in million tons of oil, and c) food consumption in kcalorie/capita/day. Time scales are not identical. Panel a) adapted from *United Nations* (2017), b) adapted from *IEA* (2018a), and c) adapted from *FAO* (2019).

1.2 Greenhouse Gases and Pollutants

1.2.1 Methane

Methane is often referred to as the second most important atmospheric GHG after CO_2, having the next highest radiative forcing impact and additional indirect climate effects (*Wuebbles and Hayhoe*, 2002; *Myhre et al.*, 2013). It has a global warming potential (GWP) of 34 over 100 years (i.e. a unit mass of CH_4 contributes to time-integrated radiative forcing 34 times more than an equal mass of CO_2) (*Myhre et al.*, 2013). Using top-down methodology (assessing GHG emissions through observational data of atmospheric concentrations), total emissions of CH_4 in 2012 were an estimated 568 Tg yr^{-1}, with 61% attributed to anthropogenic activity (*Saunois et al.*, 2016). Wetlands account for the largest single source, 30% of total emissions and 78% of natural emissions (*Saunois et al.*, 2016). The remaining natural sources include termites, the ocean, and geological processes (*Ciais et al.*, 2013; *Saunois et al.*, 2016). Fossil fuels comprise one-fifth of total CH_4 emissions and one-third of anthropogenic sources, the rest being livestock, landfills, biomass burning, and rice cultivation (*Saunois et al.*, 2016). The primary sink for CH_4 is oxidation by reacting with the hydroxyl radical OH (*Le Texier et al.*, 1988). CH_4 oxidation can lead to further reactions and emit additional atmospheric products including tropospheric ozone, formaldehyde, and CO (*Wuebbles and Hayhoe*, 2002; *Amann et al.*, 2011; *Shindell et al.*, 2012). Although CH_4 has an average atmospheric lifetime of about 9 years, its reactive nature amplifies the feedback effect of emissions and extends the lifetime of CH_4 perturbations to $\sim$12 years (*Myhre et al.*, 2013; *Holmes*, 2018).

Figure 1.2 shows the major sources, sinks, and uncertainties in the CH_4 budget for annual emissions from 2003–2012. Many of the sources and sinks have high uncertainties, and there are large discrepancies in the CH_4 budget between top-down and bottom-up (where emissions are attributed to appropriate sources from various

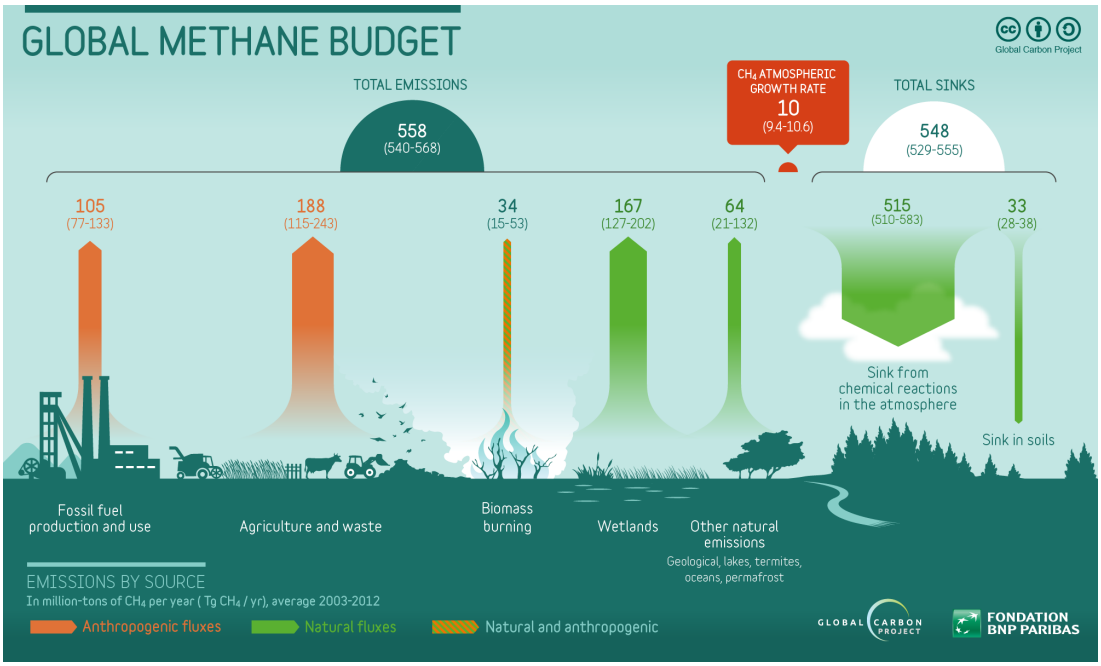

Figure 1.2: Sources and sinks for CH_4 with uncertainty ranges. Red arrows denote anthropogenic fluxes, green arrows denote natural fluxes, striped arrow denotes a mixed source. Figure adapted from the Global Carbon Project (*Saunois et al.*, 2016).

sectors and then aggregated) estimates, with bottom-up estimates at 756 Tg yr^{-1} in 2012 (*Saunois et al.*, 2016). Atmospheric CH_4 concentrations have been rising since 2007, after experiencing a brief plateau from 2000–2007 following a long period of growth (*Dlugokencky et al.*, 2009; *Nisbet et al.*, 2014). Possible explanations for the renewed increase include higher emissions from wetlands (*Schaefer et al.*, 2016; *Nisbet et al.*, 2016), increased emissions from fossil fuels (*Hausmann et al.*, 2016; *Worden et al.*, 2017), and decline in OH concentration (*Rigby et al.*, 2017). The CH_4 trends are not well understood, and small changes in sources or sinks on the order of a few percent can have large implications for total atmospheric concentrations and budget, necessitating better constraints on key CH_4 processes (*Turner et al.*, 2017, 2019).

1.2.2 Nitrous Oxide

Nitrous oxide is another important anthropogenic greenhouse gas, with the third highest warming impact after CO_2 and CH_4 and a GWP of 298 (*Myhre et al.*, 2013). In the troposphere, N_2O is fairly inert, with a relatively long average lifetime on the order of 120 years (*Portmann et al.*, 2012; *Ciais et al.*, 2013). Once it is transported to the stratosphere it can react with excited oxygen, producing stratospheric NO and NO_2 which in turn react with ozone, depleting the stratospheric ozone layer and significantly increasing the overall impact of N_2O on the climate and public health (*Ravishankara et al.*, 2009; *Ghormley et al.*, 1973; *Portmann et al.*, 2012; *Stolarski et al.*, 2015). Globally, N_2O emissions are an estimated $\sim$18 Tg N_2O-N yr^{-1} (with nitrogen atoms accounting for 28 g/mol of N_2O's 44 g/mol molar mass), 40% of that due to anthropogenic activities including agriculture, fossil fuel combustion, and biomass burning (*Ciais et al.*, 2013). These estimates have high uncertainty with total emissions ranging from 8–31 Tg N_2O-N yr^{-1}, as there is high spatial and temporal variability in N_2O emissions (*Brown et al.*, 2001; *Monni et al.*, 2007; *Davidson and Kanter*, 2014). Figure 1.3 illustrates the sources, sinks, and uncertainties in the N_2O budget.

Agricultural and natural soils are the primary sources of N_2O, accounting for $\sim$60% of annual emissions (*Ciais et al.*, 2013). Microbial activity is responsible for the main mechanisms that emit N_2O from soils. Large amounts of nitrogen are cycled via nitrification and denitrification, and a very small fraction is lost to the atmosphere as N_2O. Through nitrification, nitrifying bacteria oxidize ammonium and ammonia to nitrite and nitrate. Some gaseous N_2O is created and lost to the atmosphere as part of the process (*Smith et al.*, 2003; *Opdyke et al.*, 2009). During denitrification, when oxygen in soil is limited, anaerobic bacteria can also produce N_2O, which is subsequently lost to the atmosphere, as they reduce nitrate to N_2 (*Smith et al.*, 2003; *Opdyke et al.*, 2009)

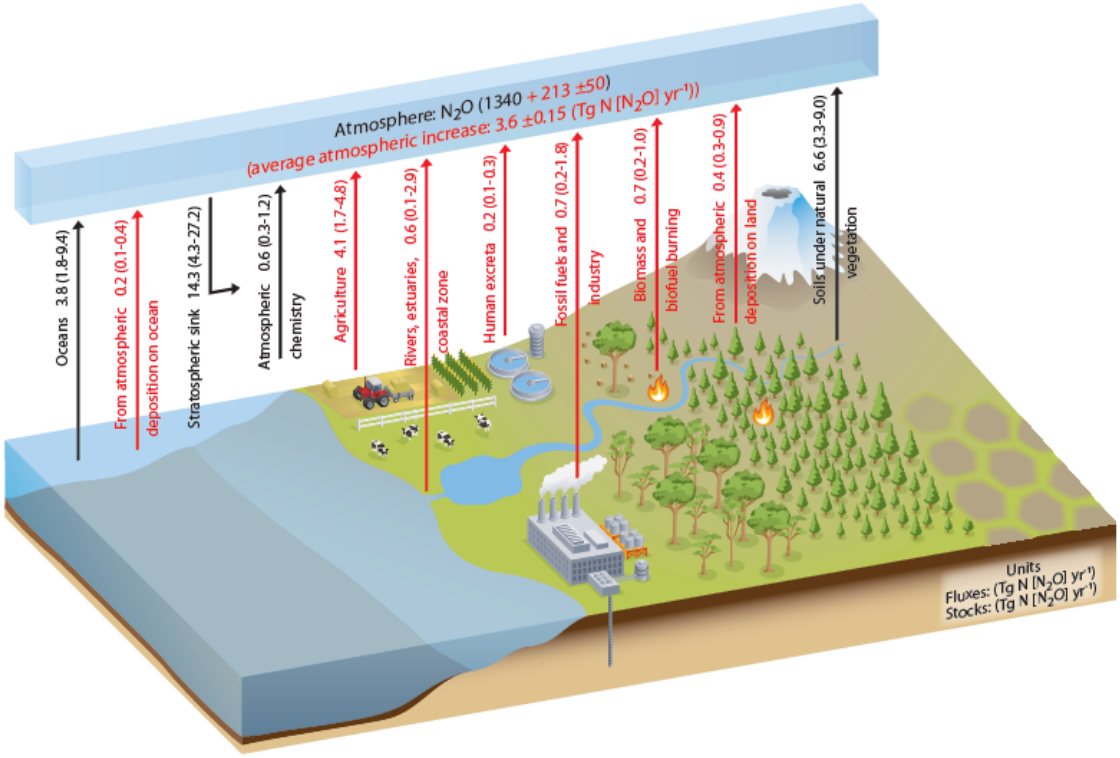

Figure 1.3: Schematic of the N_2O budget. Black arrows denote natural processes, red arrows denote anthropogenic sources. Figure adapted from *Ciais et al.* (2013).

Nitrification and denitrification tend to occur simultaneously under most soil conditions (*Braker and Conrad*, 2011; *Zhang et al.*, 2015), and the amount of net emitted N_2O varies depending on microbe and soil type, as microbes can exhibit a range of genetic diversity in various soils (*Braker and Conrad*, 2011; *Schmidt and Waldron*, 2015; *Hu et al.*, 2015; *Hink et al.*, 2018), with a possibility that generations of agricultural land use has optimized these bacteria to be more effective N_2O emitters (*Schmidt and Waldron*, 2015). Nitrification and denitrification rates can vary with changes in soil moisture, soil type, fertilizer type, and other environmental factors (*Smith et al.*, 2003; *Hu et al.*, 2015). The more excess nitrogen compounds are applied to soil, the more is available for microbes to nitrify or denitrify and emit N_2O (*Butterbach-Bahl et al.*, 2013; *Hu et al.*, 2015). Since pre-industrial times humans have more than doubled the amount of reactive nitrogen available to ecosystems through the use of fertilizer (*Melillo and Yohe*, 2014; *Lu and Tian*, 2017). Analyses have suggested approximately 2% of excess applied nitrogen is lost to the atmosphere as N_2O (*McElroy and Wang*, 2005; *Davidson*, 2009; *Grace et al.*, 2011). Global soil N_2O emissions could be responsible for up to 10 Tg N_2O-N yr^{-1} with 3.3 Tg emitted from croplands, accounting for 82% of the increase in soil N_2O emissions since pre-industrial times (*Tian et al.*, 2018).

1.2.3 Ethane

After CH_4, ethane is the second most abundant atmospheric hydrocarbon. While technically a greenhouse gas, its direct warming impact is significantly weaker than other gases such as CH_4 or N_2O. It modestly contributes to radiative forcing on the order of mW m^{-2} (*Hodnebrog et al.*, 2018). C_2H_6 also has a relatively shorter lifetime, on the order of 2-6 months (*Boissard et al.*, 1996; *Blake et al.*, 2003; *Hodnebrog et al.*, 2018). The main process by which C_2H_6 is removed from the troposphere is by oxidation, reacting with the hydroxyl radical OH (*Singh and Hanst*, 1981; *Blake and*

Rowland, 1986; *Rudolph*, 1995). Additional processes triggered by the oxidation of C_2H_6 result in the formation of compounds which all contribute to smog, including acetaldehyde, peroxyacetyl nitrate, and ozone, negatively impacting air quality and posing severe health risks (*Singh and Hanst*, 1981; *Aikin et al.*, 1982). Since CH_4 is also removed by oxidation, C_2H_6 increases the lifetime of CH_4, enhancing its perturbation to the climate (*Blake and Rowland*, 1986; *Collins et al.*, 2002). Through these indirect effects C_2H_6 has a GWP of ∼10 over 100 years (*Hodnebrog et al.*, 2018).

The main sources of C_2H_6 are fugitive emissions from fossil fuels (e.g. leaks, venting, and flaring), biomass burning, and biofuels, with more sources and thus higher emissions in the northern hemisphere (*Rudolph*, 1995; *Boissard et al.*, 1996). In 2008 *Xiao et al.* (2008) estimated C_2H_6 emissions of 13 Tg yr^{-1} with 60% due to fossil fuel production, 20% from biomass burning, and 20% from biofuel use, and 80% of all global sources located in the northern hemisphere. From 1984 to 2010 global C_2H_6 emissions steadily declined from 14.3 Tg yr^{-1} to 11.3 Tg yr^{-1}, a 21% decrease, possibly due to decreased emissions from fossil fuel production (*Simpson et al.*, 2012). Beginning in 2010 a measurement station in the Swiss Alps observed an increase in atmospheric concentration of C_2H_6, implying underestimation in emissions inventories (*Franco et al.*, 2015). This trend has continued with an annual increase in northern hemisphere C_2H_6 emissions of 0.42 Tg yr^{-1} from 2009 to 2014 (*Helmig et al.*, 2016). Figure 1.4 shows daily C_2H_6 observations from January 2003 to December 2014 from a measurement site in Toronto, Canada, though other locations in North America and Europe have observed similar trends (*Franco et al.*, 2016). The significant increase in North American oil and natural gas production over the past decade is a likely contributor to the recent reversal in C_2H_6 emissions (*Kort et al.*, 2016; *Helmig et al.*, 2016; *Franco et al.*, 2016). Since C_2H_6 shares many of the same thermogenic sources as CH_4 without any of its biogenic sources, C_2H_6 can be used to attribute CH_4 emissions to fossil fuel-related activity (*Yacovitch et al.*, 2014; *Smith et al.*, 2015; *Kort et al.*,

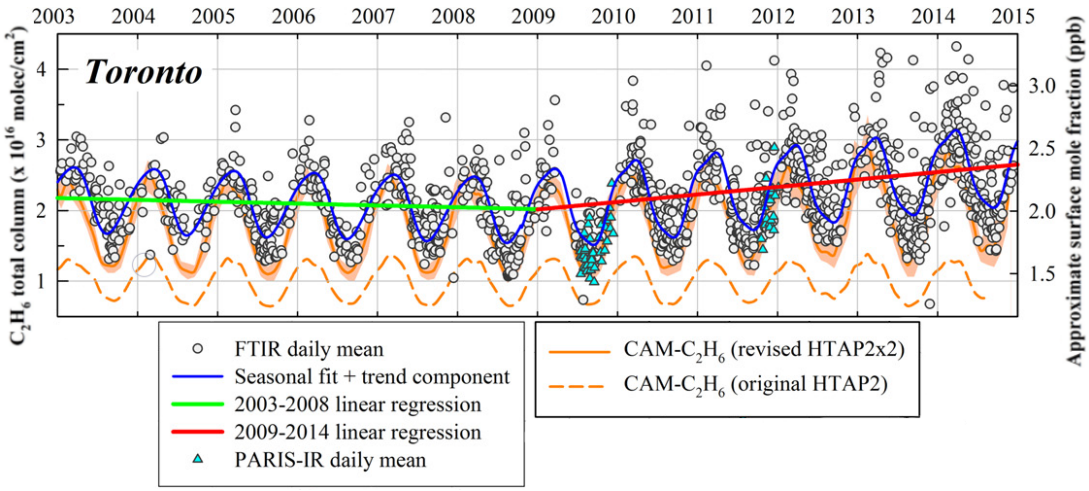

Figure 1.4: C_2H_6 observations from 2003-2015 in Toronto, Canada. Grey circles and cyan triangles indicate daily mean observations from two different spectrometers, blue curve fits the observations. The green line shows decline in C_2H_6 from 2003–2008, red line shows increase in emissions starting in 2009. Dashed and solid orange curves are simulated emissions from a model using original and revised emissions inventory, respectively. Figure adapted from *Franco et al.* (2016).

2016).

1.2.4 Black Carbon

Black carbon is an atmospheric pollutant, a byproduct of incomplete combustion (*Ramanathan and Carmichael*, 2008). Sources include residential heating and cooking, wildfires, diesel engines, and gas flaring (*Ramana et al.*, 2010; *Bond et al.*, 2013). The net radiative forcing impact of BC is an estimated ∼1 W m^{-2} (*Bond et al.*, 2013). BC is highly absorptive of solar radiation, warming the atmosphere by absorbing reflected sunlight and reducing the earth's albedo, or reflectivity (*Ramanathan and Carmichael*, 2008). BC can also mix with clouds and deposit on snow and ice, further reducing albedo and triggering a positive feedback loop, accelerating the rate of snow melt (*Flanner et al.*, 2007; *Ramanathan and Carmichael*, 2008). In 2000 total emissions of BC were estimated to be 7.5 Tg yr^{-1} with an uncertainty range of 2–29 Tg (*Bond et al.*, 2013). BC has many complex interactions with the climate system,

capable of both cooling and warming effects, and can have large spatiotemporal variability, aging with photochemical activity and getting coated with other atmospheric species (*Moffet and Prather*, 2009; *Bond et al.*, 2013). This complexity has led to some inconsistency in estimates of radiative forcing and total budget (*Bond et al.*, 2013; *Myhre et al.*, 2013; *Wang et al.*, 2014b), necessitating more measurements of BC emissions from a variety of sources and under different meteorological conditions (*Moffet and Prather*, 2009).

In addition to climate effects, airborne BC poses respiratory and cardiovascular risks, making it an indicator for air quality and mortality (*Janssen et al.*, 2011; *De Prins et al.*, 2014). BC is removed from the atmosphere by precipitation and deposition on surfaces, giving it a short atmospheric lifetime on the order of days to weeks (*Amann et al.*, 2011). Thus, reducing emissions from BC sources could have a near-immediate impact on climate and health with the largest benefits to the source regions (*Anenberg et al.*, 2011). A reduction in BC emissions would also reduce the atmospheric concentration of other products such as CO, NO_x, and volatile organic compounds, which are major precursors to tropospheric ozone and are coemitted with BC (*Anenberg et al.*, 2012). The improvement in air quality could avoid up to 5 million premature deaths in 2030 (*Anenberg et al.*, 2012). Solely in terms of reducing radiative forcing from anthropogenic sources, mitigating BC emissions may not be the best strategy, as coemitted products have some cooling impact and there is difficulty in efficiently eliminating BC sources in both developed and developing countries (*Bond and Sun*, 2005). Still, there are plenty of possibilities to reduce radiative forcing and diminish climatic interference, especially with improved understanding of combustion sources and reduced uncertainty in emissions (*Bond and Sun*, 2005; *Shindell et al.*, 2012).

1.3 Changes in Energy and Agriculture

1.3.1 Fossil Fuels

The fossil fuel industry is one of the largest sources of anthropogenic GHGs, capable of emitting at all stages in the supply chain from drilling to distribution (*Balcombe et al.*, 2018). Fossil fuel production has drastically changed and increased with technological advancements in horizontal drilling and hydraulic fracturing allowing "unconventional wells" to produce from previously inaccessible reserves of shale gas and tight oil, particularly in the US (*Wang et al.*, 2014a). Figure 1.5 shows domestic oil and gas production in the US over several decades along with what fraction of total production comes from tight oil and shale gas. From 2005–2017 US natural gas gross withdrawals increased by 42% while oil production rose by 80% (*EIA*, 2019a,b). The US is the second largest energy producer and consumer in the world after China, accounting for 14% of all energy production and 16% of consumption in 2016 (*IEA*, 2018b). The US owes 33% of its energy production to natural gas and is responsible for 20% of the world's total natural gas production (*IEA*, 2018a). In the near future the United States, already a net natural gas exporter, is poised to become a net total energy exporter (*EIA*, 2019d). The production of shale gas is expected to continue to rise while production from other sources diminishes, with a projected 90% of global natural gas extracted from shale reservoirs by 2050, much of it from the US (*IEA*, 2018c).

The oil and gas industry's growth has also led to increased flaring. Gas that wells cannot capture and process due to insufficient storage or infrastructure is combusted, emitting CO_2 rather than hydrocarbons and volatile organic compounds. From 2012–2016 the annual global gas volume flared rose from ∼140 billion cubic meters (*Elvidge et al.*, 2016) to ∼148 before dropping back down to ∼140 BCM in 2017 (*The World Bank*, 2017). Flaring is not 100% efficient, and through incomplete combustion it

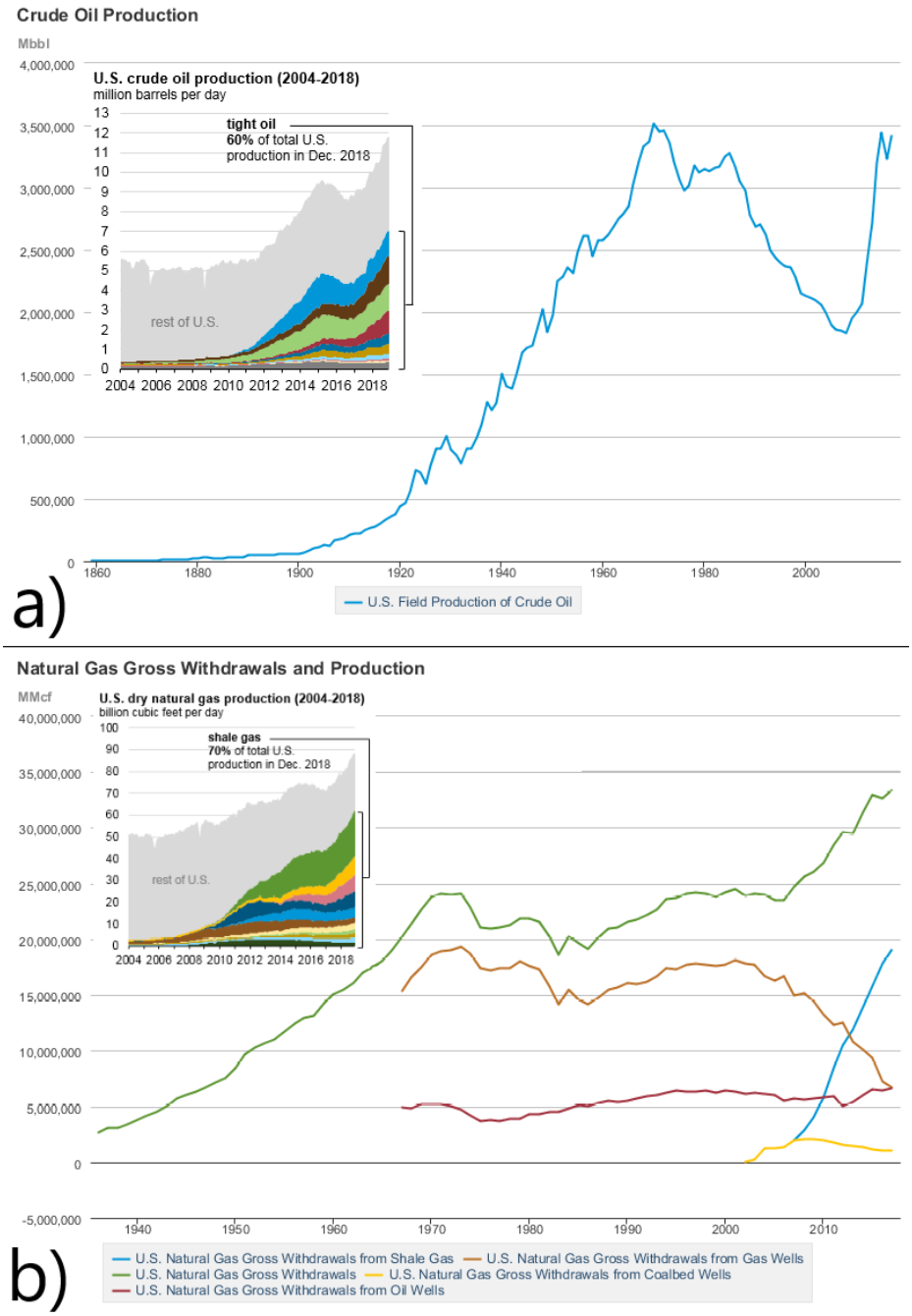

Figure 1.5: a) US crude oil production from 1859–2017 in thousand barrels per year. Insets shows tight oil as fraction of production in million barrels per day. b) US natural gas gross withdrawals (green) from 1937–2017 in million cubic feet per year, split by shale gas (blue), conventional gas (brown), oil wells (red), and coalbed wells (yellow). Inset shows shale gas as fraction of production in billion cubic feet per day. Colors of both insets denote different production regions in the US. Figure adapted from *EIA* (2019a,b,c).

emits CH_4, C_2H_6, BC, and other VOCs. Flaring emissions have high uncertainty since emission factors used to estimate emissions are based on limited measurements or laboratory settings (*Allen et al.*, 2016). Variability in flare types and operating conditions, for instance temperature, flame control, and spatial compactness, can affect emissions and the flare height and heat allows pollutants to transport easily in the atmosphere (*Abdulkareem et al.*, 2009; *Fawole et al.*, 2016). The increase in flaring may have a large impact on BC emissions (*Schwarz et al.*, 2015; *Weyant et al.*, 2016). Flaring contributes 3% of global BC emissions but dominates in the Arctic, accounting for 42% of annual mean surface concentrations (*Stohl et al.*, 2013).

Given the recent increase, how well are we keeping track of fossil fuel emissions? Observational data has routinely found that inventories are underestimating total emissions and that sources can exhibit a heavy-tailed characteristic, where a small set of emitters is disproportionately responsible for a large fraction of total emissions (*Brandt et al.*, 2014; *Balcombe et al.*, 2018). This "superemitter" phenomenon can result in 5% of sources being responsible for 50% of emissions and needs to be better understood to improve mitigation and efficiency in oil and gas systems (*Brandt et al.*, 2016). Studies in multiple oil and gas production basins around the US have observed superemitters, with the top percentile of emitters accounting for up to 25–30% of total regional emissions (*Caulton et al.*, 2014b; *Frankenberg et al.*, 2016b). The possibility for high CH_4 emissions due to leakage from natural gas systems threatens to outweigh any climate benefits of switching fuel consumption in the US from oil and coal to natural gas. In the past decade the use of coal in electricity generation has decreased in the US, with natural gas and renewable energy sources such as solar power increasing their share (*EIA*, 2019d). For the US, prioritizing natural gas over coal for electric power, or gasoline and diesel for transportation purposes, provides both energy independence and the potential for lower GHG emissions due to lower carbon content (*Alvarez et al.*, 2012). Accurate tracking of emissions is necessary to

evaluate the benefits of fuel-switching (*Schwietzke et al.*, 2014). It is not sufficient to estimate emissions purely by a bottom-up method, they need to be validated and reconciled with top-down methodologies utilizing atmospheric observations, remote sensing data from satellites, and output from climate models in concert (*Nisbet and Weiss*, 2010; *Kort et al.*, 2014; *Zavala-Araiza et al.*, 2015).

1.3.2 Agriculture

The agricultural sector is a significant source of atmospheric GHGs, accounting for around 12% of total anthropogenic emissions (*Smith et al.*, 2014). In the US, agricultural sources contribute 9% of all national GHG emissions including 40% of CH_4 and 80% of N_2O as of 2016 (*EPA*, 2018). The amount of global cropland has considerably expanded over time, with 40% of the earth's non-ice land area devoted to agriculture (*Foley et al.*, 2011). In recent decades a global rise of sugars, oils, fats, and meats in diets has resulted in increased agricultural productivity and emissions (*Tilman and Clark*, 2014). Figure 1.6 shows fertilizer use over time in the US, with a 40 times increase between 1940 and 2015 (*Cao et al.*, 2018). Mitigation requires some combination of altering diets to reduce demand for crops and livestock that contribute higher emissions as well as slowing down or ideally ceasing land expansion by improving the efficiency of crop production, especially in underperforming regions. Continued intensification, or improving crop yields per area cropland, is a promising avenue to mitigation and since 1961 has avoided an estimated one-third of total post-industrial anthropogenic GHG emissions (*Burney et al.*, 2010). With proper technological and management improvements it is possible to decouple emissions and yields, optimizing high yields and low emissions up to a certain point (*Bennetzen et al.*, 2016). If consumption and diets stay constant, emissions will likely increase until 2055 as more people worldwide consume higher value foods and developing nations advance their agricultural infrastructure and production (*Popp et al.*, 2010;

FAO, 2017).

A better understanding of agricultural emissions can improve mitigation strategies, especially if good estimates are available for regional and food-specific impacts, particularly in wealthier developed nations (*Aleksandrowicz et al.*, 2016). Regarding N_2O, there is large uncertainty in emissions estimates and inventories (*Bouwman et al.*, 1995). One reason for difficulty in creating a N_2O budget is there are several components in the nitrogen cycle and many agricultural sources of N_2O, including direct emissions from soils, emissions from animal waste, and indirect emissions from leaching/runoff of nitrogen into water systems, all contributing to total uncertainty (*Mosier et al.*, 1998). There is high spatial and temporal variability in N_2O emissions that needs to be considered, making it difficult to use emissions from one area and time as representative of an entire national region and year (*Monni et al.*, 2007; *Nevison et al.*, 2018). Agricultural productivity and emissions are also affected by the climate. In the US, temperature and precipitation trends can explain 70% of variation in yields, and future climate scenarios could cause large drops in productivity (*Liang et al.*, 2017). Direct observations of N_2O emissions are limited in some geographical areas and production sectors (*Reay et al.*, 2012). Quantifying N_2O fluxes from key regions and sectors is needed to guide mitigation strategies, reduce discrepancies in top-down and bottom-up estimates, and better understand the dynamic and complex interactions between agricultural emissions, nitrogen availability in ecosystems, and climate change (*Reay et al.*, 2012; *Wollenberg et al.*, 2016).

An ideal monitoring system would measure throughout the year in various fields, even once per day (*Bouwman et al.*, 2002). Though that might be impractical, better knowledge of emissions from crop production is essential for life cycle assessments to investigate agricultural systems (*Brentrup et al.*, 2000). A major goal for the agricultural sector is to develop best management practices to optimize nitrogen uptake by maximizing yield but reducing emissions. This can be done by identifying and quan-

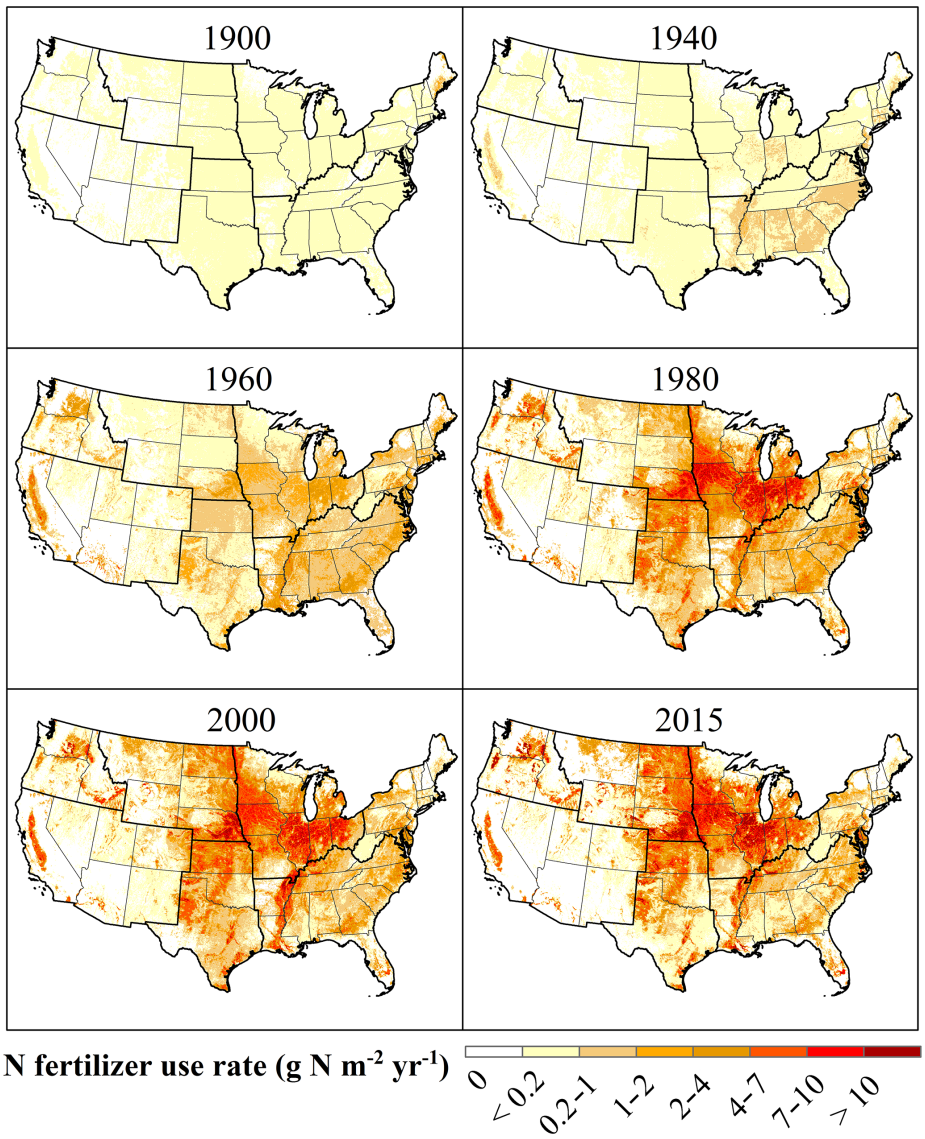

Figure 1.6: Growth in annual N fertilizer use rate in the US from 1900 to 2015. Resolution is 5 km by 5km grid cells. Figure adapted from *Cao et al.* (2018).

tifying sources of emissions and reducing the uncertainty of measurements, improving on the default emission factors used in inventories which do not always account for specific crop type, fertilizer type, and other underlying factors (*Brentrup et al.*, 2008; *Signor and Cerri*, 2013). Identifying agricultural systems with inefficient nitrogen use would facilitate optimization and mitigation, so the ability to estimate emissions for entire crop fields is highly valuable (*Desjardins et al.*, 2001; *Clark and Tilman*, 2017; *Zhang et al.*, 2013). Optimizing factors such as fertilizer type (urea, ammonium nitrate, potash, etc.) and production technique can substantially reduce emissions in the fertilizer supply chain (*Hasler et al.*, 2015). N_2O emissions from croplands exhibit a large seasonality effect with emissions typically occurring in bursts during several key periods in the crop cycle (planting and fertilizing in spring, harvest in the summer, freeze/thaw in winter), making it a challenge to represent annual emissions with infrequent measurements (*Kavdir et al.*, 2008). Improving the availability of data on spatial and temporal variability in N_2O emissions and the accuracy of pertinent information including fertilizer application rates and irrigation water use is key in supply chain accounting and mitigating emissions (*Smith et al.*, 2017b). Improvements over the past few decades in energy-use efficiency and nitrogen-use efficiency have reduced the amount of N_2O emitted per unit of production, but emissions are still rising, requiring additional field research and model development to assess mitigation attempts and further improve efficiency (*Cavigelli et al.*, 2012).

1.4 Laser Spectroscopy

The absorptive property of greenhouse gases makes studying them through laser spectroscopy an appropriate choice (*Fried and Richter*, 2007; *Heard*, 2008; *Du et al.*, 2019). These instruments, used extensively in the research of atmospheric greenhouse gases, are capable of high-precision and high-accuracy measurements (*Nelson et al.*, 2002; *Curl et al.*, 2010). They are robust and can be deployed in either laboratory

or field settings, including on vehicles. The mid-IR spectrum, in the 4000–400 cm^{-1} wavenumber or 2.5–25 μm range, exhibits strong absorption features and high sensitivity, allowing for better identification of greenhouse gases than other spectral regions (*Stuart*, 2000; *Zhang et al.*, 2014). Linestrengths for some greenhouse gases can be up to 100,000 times stronger in the mid-IR than near-IR. While there are several types of laser spectrometers available, this thesis focuses on observations made with a continuous-wave, tunable infrared laser direct absorption spectrometer. Figure 1.7 diagrams the optics of such an instrument made by Aerodyne Research, Inc. Several mirrors align the beam into a 0.5 L optical cell. The 32 cm long cell has reflective mirrors on both ends which allow the incident beam to reflect 238 times before exiting the cell if aligned properly, resulting in a path length of 76 m. After exiting the cell the beam is aimed into a photodetector. Air flows in and out of the cell with a vacuum pump, holding the cell at a constant pressure. Current through the laser is adjusted to scan the laser's wavelength across a range covering absorption peaks of several greenhouse gases, allowing for multi-species analysis. The change in incident laser intensity and the intensity detected after passing through the cell is used to calculate the concentration of a species. The calculation makes use of Beer's Law, given as Equation 1.1

$$A = N \times \sigma \times L \tag{1.1}$$

where A is the fractional absorption, N is the molecular number density, σ is the absorption cross section of a molecule, and L is the absorption path length. N is the desired measurement: what ratio of the air is occupied by a particular trace gas. Laser intensity measured by the photodetector is used to calculate A, σ has been calculated for a large suite of transitions (*Rothman et al.*, 2013), and the path length L is known, in this case 76 m. A long path length and strong transition are desirable to reduce noise in absorption and improve precision.

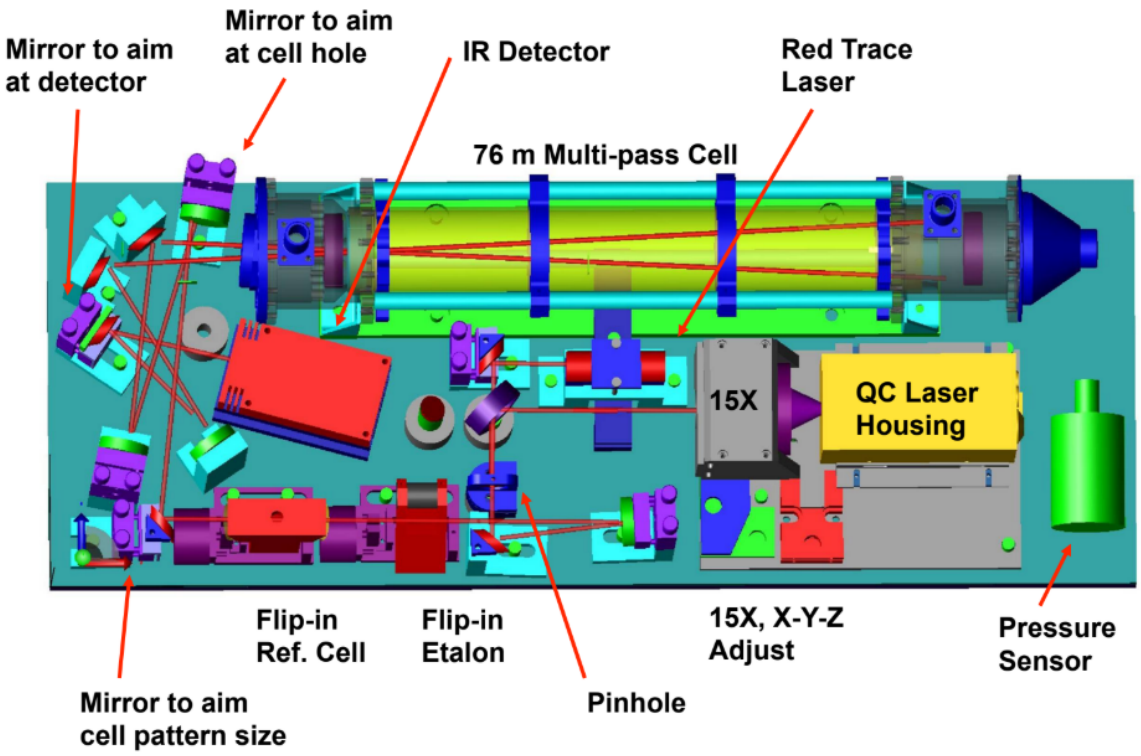

Figure 1.7: Diagram of a continuous-wave, tunable infrared laser direct absorption spectrometer. Figure adapted from Aerodyne Research Inc.

Figure 1.8 shows a screenshot of the TDL Wintel retrieval software for an Aerodyne, Inc. trace gas laser monitor. For this instrument the absorption peaks cover a wavenumber range of 2227.4–2227.9 cm^{-1}. The laser frequency is periodically stabilized by frequency locking, where the absorption peak of a specific reference gas, in this case N_2O, is set to an appropriate position or channel. For instruments that frequency lock using a gas with small absorption profiles due to low atmospheric ambient values, such as C_2H_6, a reference cell is flipped in during frequency locking, as indicated in Figure 1.7. Temperature, electric interference, and other factors can cause drift in the instrument over time, affecting the trace gas measurement (*Werle*, 2011; *Smith et al.*, 2013). Periodic sampling of either a reference gas with a known composition or a zero gas with no detectable trace species can be used to adjust for the drift and maintain accuracy, and the instrument's software can automate the calibration. The interface also provides real-time monitoring of measurements, allowing for adjustment of sampling strategy or route if the instrument is deployed on a mobile platform such as a van or an airplane.

1.5 Airborne Observations

For decades, airborne measurements have been a valuable tool for quantifying emissions of atmospheric trace gases (*White et al.*, 1976). Airborne campaigns allow for large regional coverage, can characterize the boundary layer in-flight with a vertical profile, and can assess emissions from difficult-to-reach sources including offshore platforms (*Nara et al.*, 2014; *Flamant et al.*, 2018) or remote wells far away from major roads (*Cambaliza et al.*, 2014). Airborne observations can be used to quantify emissions from urban sources (*Mays et al.*, 2009; *Turnbull et al.*, 2011; *Cambaliza et al.*, 2014) or fossil fuel production (*Karion et al.*, 2015; *Peischl et al.*, 2015a), and have been used to study a variety of gases and pollutants including ozone (*Trainer et al.*, 1995), N_2O (*Xiang et al.*, 2013), CH_4 (*Peischl et al.*, 2016), BC (*Schwarz et al.*,

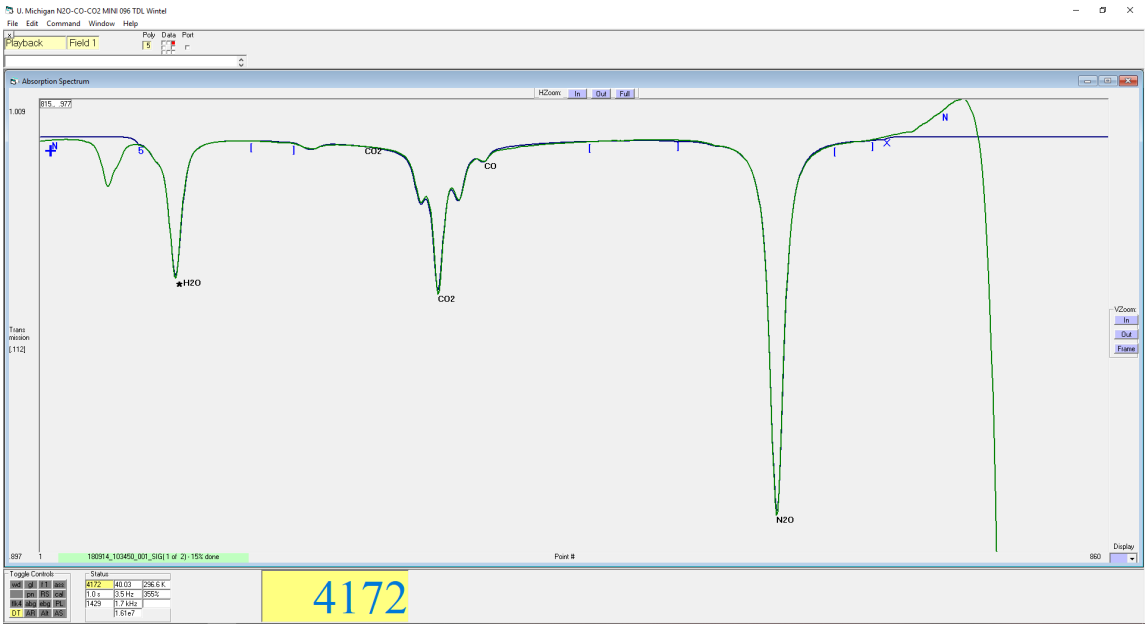

Figure 1.8: Screenshot of TDL Wintel interface showing the absorption spectra of H_2O, CO_2, CO, and N_2O in green, with line of best fit in blue.

2015; *Weyant et al.*, 2016), and C_2H_6 (*Smith et al.*, 2015; *Kort et al.*, 2016).

A common approach is the mass balance method, illustrated by Figure 1.9. The plane flies downwind of an emissions source, sampling the plume throughout the transect. This technique assumes the mixing layer is well-mixed, with a consistent boundary layer height, and relies on steady unidirectional winds. The emissions flux in mol/s calculated with the mass balance method is given by Equation 1.2

$$flux = \nu\, cos\theta \int_{x_i}^{x_f} X \,\mathrm{d}x \int_{z_g}^{z_{PBL}} n_{air} \,\mathrm{d}z. \tag{1.2}$$

where $\nu\, cos\theta$ is the horizontal wind component perpendicular to the airplane's heading, x_i and x_f define the width of the flight transect over ground, X is the molar fraction enhancement over background during the transect, z_g and z_{PBL} define the distance between ground level and the planetary boundary layer, and n_{air} is the molar density of air. This equation can be adjusted and used with several approaches

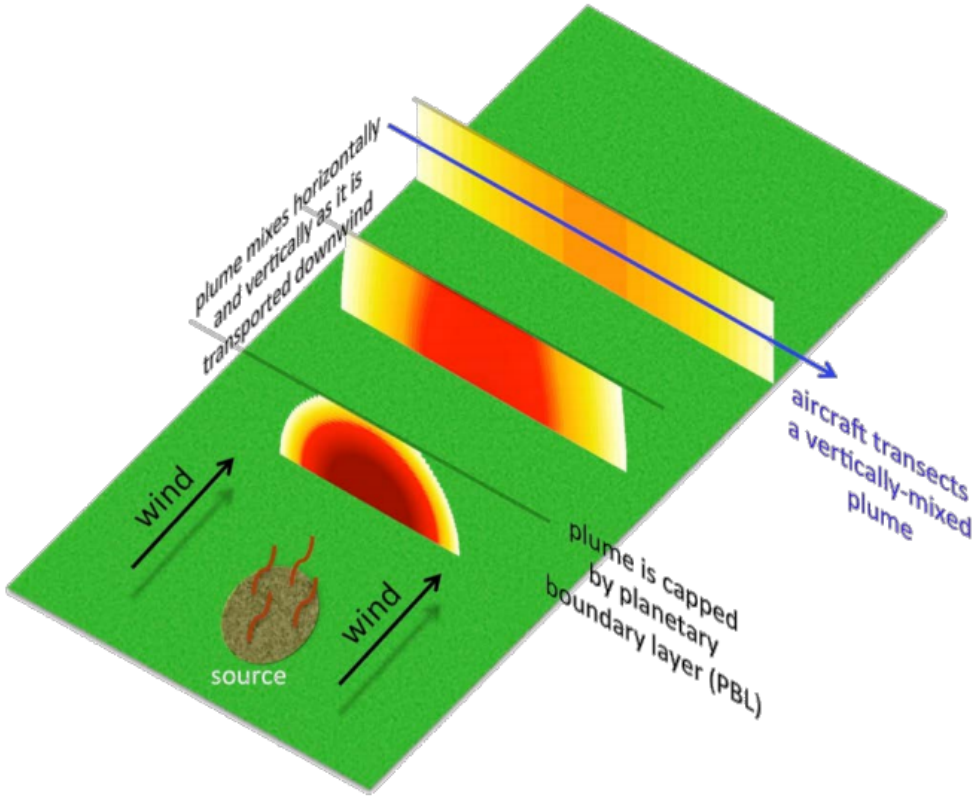

Figure 1.9: Illustration of the airborne mass balance technique. Figure adapted from *Peischl et al.* (2015b).

depending on background choice or complexities in the mixed layer height.

When deploying laser spectrometers on airplanes, careful considerations must be made with regard to power draw, weight, accessibility, and safety (*Richter et al.*, 2013). The instrument and all related equipment must be secured and strapped in. All parts of the flow scheme including tubing and gas regulators must be checked pre-flight to ensure no leaks are present, since in-flight tightening may not be feasible. Test flights are also needed to assess in-flight performance.

1.6 Dissertation Outline

This thesis presents assessments of atmospheric emissions of greenhouse gases from oil, gas, and agricultural sources using continuous airborne observations. Chapter II

examines the efficiency of natural gas flares from oil wells in the productive Bakken Shale region of North Dakota, published as *Gvakharia et al.* (2017). Flaring efficiency is reported for CH_4, BC, and for the first time, C_2H_6. Flares appear to follow a non-normal distribution with higher-emitting flares contributing to a larger fraction of total emissions, a superemitter behavior characterized by other sources in the oil and gas sector. Even with the skewed distribution, BC emissions are lower compared to reported emissions from the region and do not strongly correlate with CH_4 emissions. For CH_4 and C_2H_6, however, flaring could contribute $\sim$20% of total regional emissions, more than double the value if a standard flaring efficiency is assumed.

Chapter III details the development and testing of an airborne system to measure N_2O, CO_2, CO, and H_2O, published as *Gvakharia et al.* (2018). The main component is a trace gas laser monitor that previous literature suggested was sensitive to variations in pressure during airborne operation. A repeatable pressure artifact is confirmed in test flights and corrected for by extending on previous calibration approaches with a flow-controlled system and frequent calibrations, accounting for drifts on short time scales. Calibrated CO_2 and H_2O data are compared with a different flight-tested spectrometer, showing good agreement and validating the technique. In-air 1σ precision of the instrument is comparable to laboratory operation, making it suitable for airborne studies.

Chapter IV presents airborne observations made using the system described in the previous chapter to quantify agricultural emissions in the fecund Lower Mississippi River Basin. N_2O, CO_2, and CH_4 emission fluxes are calculated for two fertilizer plants that together account for a significant fraction of US fertilizer production. Observed N_2O and CO_2 emission rates agree well with reported values but observed CH_4 emissions are several orders of magnitude higher than expected. Regional N_2O fluxes are quantified using the mass balance technique for the first time. These fluxes are compared with several emissions drivers: crop type, applied fertilizer, soil

moisture, and soil temperature. Finally, Chapter V summarizes the main thesis results and discusses future research directions.

CHAPTER II

Flaring: CH_4, C_2H_6, and BC emissions from natural gas flares in the Bakken Shale, ND

Abstract

Incomplete combustion during flaring can lead to production of black carbon (BC) and loss of methane and other pollutants to the atmosphere, impacting climate and air quality. However, few studies have measured flare efficiency in a real-world setting. We use airborne data of plume samples from 37 unique flares in the Bakken region of North Dakota in May 2014 to calculate emission factors for BC, methane, ethane, and combustion efficiency for methane and ethane. We find no clear relationship between emission factors and aircraft-level wind speed, nor between methane and BC emission factors. Observed median combustion efficiencies for methane and ethane are close to expected values for typical flares according to the US EPA (98%). However, we find that the efficiency distribution is skewed, exhibiting log-normal behavior. This suggests incomplete combustion from flares contributes almost 1/5 of the total field emissions of methane and ethane measured in the Bakken shale, more than double the expected value if 98% efficiency was representative. BC emission factors also

have a skewed distribution, but we find lower emission values than previous studies. The direct observation for the first time of a heavy-tail emissions distribution from flares suggests the need to consider skewed distributions when assessing flare impacts globally.

2.1 Introduction

Over 140 billion cubic meters (BCM) of gas is globally flared each year (*Elvidge et al.*, 2009). Flaring is used to dispose of gas at production and processing facilities that lack infrastructure and means to capture or use the gas. The United States flares about 8 BCM per year, with almost half of that coming from North Dakota alone (*EIA*, 2016). From 2004 to 2014, the amount of gas annually flared in North Dakota increased from 0.08 BCM to 3.7 BCM, and in 2014 about 28% of North Dakota's total produced natural gas was flared (*North Dakota State Government*, 2016). Flaring has implications for the atmosphere. Although ideally gas would be captured instead of lost, it is preferable to flare rather than vent, since flaring destroys methane (CH_4) and volatile organic compounds which affect air quality, converting them to CO_2. CH_4 is a potent greenhouse gas, the 2nd most important anthropogenic greenhouse gas behind CO_2 based off integrated radiative forcing (*IPCC*, 2013; *Shindell et al.*, 2009). Flaring is not 100% efficient, and through incomplete combustion it can be a source for CH_4 and VOCs (*Ismail and Umukoro*, 2012; *Simpson et al.*, 2012). Flaring can also create black carbon (BC) as a byproduct, an anthropogenic forcer of climate with public health implications (*Bond et al.*, 2013; *Stohl et al.*, 2013; *Schwarz et al.*, 2015; *Anenberg et al.*, 2012). The World Bank recently introduced a "Zero Routine Flaring" initiative to end flaring worldwide by 2030 through government incentives and institutional cooperation, hoping to mitigate economic losses due to flaring and relieve its burden on the atmosphere (*The World Bank*, 2016c).

Inventories that account for flaring often use a combustion efficiency value of 98%

of the initial gas, citing an EPA technical report (*EPA OAQPS*, 2012; *EPA*, 1998). This efficiency value assumes flare stability, and can decrease based on wind speed and other factors such as flow rate or aeration. Studies have investigated flare efficiency in laboratories using scaled-down flare simulations in a controlled environment, reporting 98–99% flare combustion efficiency (*Johnson and Kostiuk*, 2000, 2002), but there have been few field studies done to assess flare efficiency and directly measure emissions in a real-world environment. Thus, scaled-up laboratory results may not be representative of real-world flaring. A study of two flare sites in Canada calculated an average observed combustion efficiency of 68 ± 7%, much lower than the assumed efficiency (*Leahey et al.*, 2001). One remote sensing study in the Netherlands found high efficiencies of 99% but only analyzed three flares, with up to 30% error in the measured gas concentrations, and noted the lack of in situ data (*Haus et al.*, 1998). There was also a comprehensive study to observe industrial flare emissions and efficiency but the tests were conducted at a flare test facility, not directly at well sites (*Knighton et al.*, 2012). To our knowledge the only extensive study of in situ flare efficiency for CH_4 sampled ten flares in the Bakken Shale in North Dakota and one in western Pennsylvania (*Caulton et al.*, 2014a). This study reported high flare efficiencies up to 99.9% but based on their identification techniques, they acknowledged a possible bias towards larger, brighter burning, and thus more efficient, flares.

Black carbon emissions from gas flaring have been investigated, but there are not many studies that use direct observations of flaring. *Schwarz et al.* (2015) quantified total field emissions of BC and derived an upper-bound on BC emission factor for flaring from the Bakken using the same aircraft campaign data as used in this paper. Their emission factor was obtained using BC flux calculated with a mass balance technique for the entire field. Hence, it did not target individual flares. It includes all BC sources in the region (e.g. diesel trucks, generators, limited agriculture, etc.) and is expected to provide an upper bound. *Weyant et al.* (2016) calculated BC emission

factors from targeted flares in the same region and found an average value well below the upper bound of *Schwarz et al.* (2015), and to our knowledge is the only previously published peer-reviewed study of BC emissions from flaring that directly sampled flares. BC emission factors have been shown to vary based on fuel chemistry and stability of the flare, necessitating the use of specific emission factors or a distribution rather than using a single average value as representative (*McEwen and Johnson*, 2012).

The lack of direct, in situ observations of flaring efficiency suggests that estimates of emissions from incomplete combustion may be inaccurate. Also, using a single value for flaring emission factors or combustion efficiency does not take into account the various parameters that may affect a flare (*Kahforoushan et al.*, 2010), and a statistically robust sample of flaring efficiency would help identify a representative distribution. Total fugitive emissions from oil and gas production and leakage can be a substantial source of atmospheric CH_4 and are underrepresented in inventories (*Brandt et al.*, 2014). Studies have observed non-normal distribution of CH_4 emissions in some fields, where less than 10% of sampled sources contributed up to 50% of the sampled emissions (*Yuan et al.*, 2015; *Mitchell et al.*, 2015; *Allen*, 2014; *Brandt et al.*, 2016; *Frankenberg et al.*, 2016b). A study of flare emissions using Greenhouse Gas Reporting Program and Gas Emission Inventory data found that 100 flares out of 20,000 could be responsible for over half the emissions in the US, but this conclusion results from the non-normal distribution of gas volume flared and not from a skewed flare combustion efficiency (which is not represented) (*Allen et al.*, 2016). In addition to the non-normal distribution of gas volume flared, there may be a skewed distribution of emissions from incomplete combustion in flares based on efficiency as well.

We present an analysis of combustion efficiency and emission factors of CH_4, BC, and C_2H_6 for thirty-seven distinct flares in the Bakken Shale Formation in North

Dakota using data obtained during a May 2014 aircraft campaign, to our knowledge the largest study of flaring emissions in the field based on number of flares and the first to include C_2H_6. This gives us sufficient statistics to obtain an efficiency distribution and determine the implications for total fugitive emissions from incomplete combustion in actual field conditions.

2.2 Methods

2.2.1 Flights and Instrumentation

All observations used in this analysis were made as part of the TOPDOWN 2014 (Twin Otter Projects Defining Oil/gas Well emissioNs) study, and were collected onboard a National Oceanic and Atmospheric Administration (NOAA) DHC-6 Twin Otter aircraft (*Peischl et al.*, 2016; *Schwarz et al.*, 2015; *Kort et al.*, 2016). This campaign focused on understanding the atmospheric impact of fossil fuel extraction activities. 17 research flights were conducted on 11 separate days between May 12–26, 2014, totaling 40 hours. Flights were typically 3–3.5 hours in duration, and were primarily conducted at low-altitudes (400–600 magl) within the planetary boundary layer at an average speed of 65 m/s. Vertical profiles were performed in each flight to define the mixed layer height. Flights dedicated to mass balance conducted transects around the Bakken region, and although a few flares were sampled during these transects, most of the flares were identified on "mowing-the-lawn" flights that swept across the region to target point sources as well as some flights dedicated to point source identification. Flares were circled multiple times during these flights between 400–600 magl although some were sampled higher up, around 1000 magl. Flares were not specifically targeted for any particular characteristic such as size, brightness, or flaring volume. Flares were sampled over the entire region rather than in a particular cluster, giving low spatial sampling bias. However, due to the nature of the sampling,

brighter flares were more easily identifiable from the plane and thus more likely to have been targeted. Not all passes by a flare produced a well-defined peak that could be used in the efficiency analysis. Many of the flares were sampled at a distance on the order of hundreds of meters to kilometers downwind. This gave the flare plume time to disperse and allowed us to measure large plumes over a time period of 10–20 seconds, providing more data per plume than if we sampled closer and lower.

CH_4, CO_2, carbon monoxide (CO), and water vapor (H_2O) were measured with a Picarro 2401-m cavity ringdown spectrometer with a sampling rate of 0.5 Hz. CH_4 was measured with an accuracy of $\pm$1.4 ppb and precision of $\pm$0.2 ppb; CO_2 with an accuracy of $\pm$0.15 ppm and precision of $\pm$0.03 ppm (*Karion et al.*, 2013, 2015). An Aerodyne mini direct absorption spectrometer was used to continuously measure C_2H_6, deployed as described previously in literature (*Yacovitch et al.*, 2014; *Smith et al.*, 2015) along with hourly measurements of a standard gas to confirm stability (*Kort et al.*, 2016). Sampling was conducted at 1 Hz with precision of < 0.1 ppb and average accuracy of $\pm$0.5 ppb (*Kort et al.*, 2016). Due to the Aerodyne ethane instrument having a response time of 1 second, compared to the Picarro's 2 second response time, there were sharper, narrower peaks in C_2H_6 than CO_2 and CH_4. To enable a point-by-point comparison of C_2H_6 to CO_2, a weighted moving average (WMA) was applied to the C_2H_6 data. The total integrated value of the C_2H_6 peak did not significantly change with the WMA filter, indicating conservation of mass with the method.

All trace gases are reported as dry air mole fractions, converted from the measured wet air mole fractions using water vapor observations from the Picarro. A single-particle soot photometer (SP2 by Droplet Measurement Technology Inc., Boulder, CO) was used to measure refractory black carbon (rBC) for particles containing rBC in the mass range of 0.7–160 fg. The SP2 provided 1-second rBC mass-mixing ratios with systematic uncertainty of 25% (*Schwarz et al.*, 2010, 2015). Two differential

GPS antennae on the fuselage of the Twin Otter provided aircraft heading, altitude, latitude, longitude, ground speed, and course over ground. Wind speed was calculated as described in *Conley et al.* (2014), with estimated uncertainties of ±1 m/s in magnitude and ±6° in direction. A Rosemount de-iced Total Temperature Sensor, model number 102CP2AF, measured ambient temperature. Calibration before and after the field project indicate measurement performance with precision of ±0.2 °C and accuracy of ±1.0 °C.

2.2.2 Flare Identification

We identified flares in the following ways. During the science flights, all significant events were logged, including when the plane flew by a flare. These flight notes thus provide times when a flare was visually confirmed, and these flare plumes were identified in the data for the corresponding flight and flagged. After locating all the flares confirmed by the flight notes, we searched through the remaining data to find plumes that could be possible flares but were not noted during the flight, such as smaller flares that might have been hard to see on the ground. To identify the other possible flare plumes, we looked for peaks in CO_2 where ΔCO_2, the peak enhancement, was greater at its maximum point than 4σ of the CO_2 background variability, indicating a statistically significant elevation of CO_2 as a result of combustion from a flare. We also looked for a peak less than 20 seconds in time. At a mean ground speed of 65 m/s this corresponds to a source about 3 km away using Gaussian plume theory (*Zannetti*, 1990), which is about the distance we tended to sample where the plume still presented a robust signal above background. Figure 2.1 shows the research aircraft flight paths, known flare locations (*North Dakota State Government*, 2016), and where we sampled plumes.

To verify if these additional plumes identified in the data were indeed caused by flaring, we co-plotted the locations of these events with all nearby wells with reported

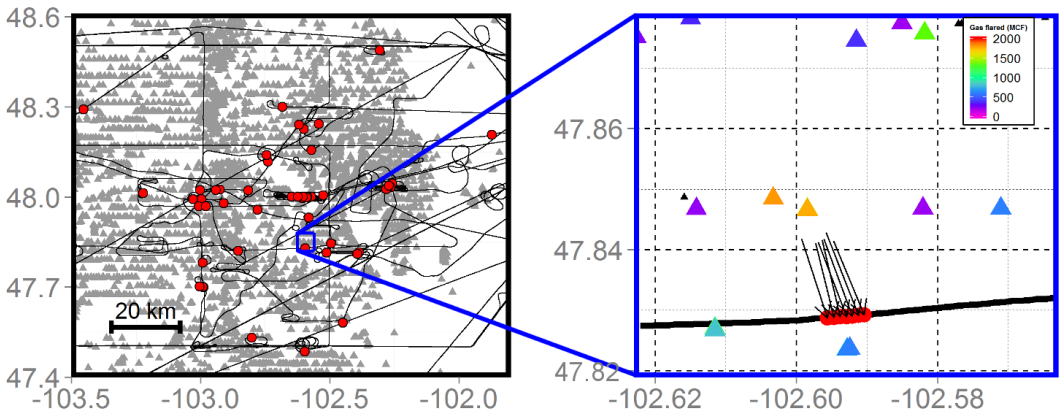

Figure 2.1: Left panel shows flight paths (black lines), wells with known flaring (grey triangles) (*North Dakota State Government*, 2016), and flare plume locations (red points) from the TOPDOWN 2014 campaign in the Bakken field in northwest North Dakota. Times when the plane circled around an area multiple times to repeatedly sample can be seen in the middle of the region. Right panel is zoomed in on a single flare plume, with flight path (black line), flare plume (red points), and wells with reported flaring (filled triangles with corresponding monthly flaring amounts). The arrows indicate the wind direction. We used the wind direction, distance from well, and flaring amount to verify that the plume was caused by flaring.

flaring and other CO_2 producers such as processing facilities and gas plants using the EPA GHG Reporting Program as seen in Figure 2.1. Certain flare locations were cross-checked with additional data from the VIIRS Active Fire Map and North Dakota Oil and Gas ArcIMS Viewer. Then, using Gaussian plume theory, we estimated how far away the source of a plume was based on the plume width and wind conditions, matching the plume to a possible flare source (*Zannetti*, 1990). Although the science flights were conducted on days with steady winds, leading to low variability in wind speed and direction, we accepted plumes that were within 20% of the theoretical distance to account for deviation in other factors such as not flying directly in the center of the diffused plume. If a plume was located downwind from a well with flaring, was not downwind of another CO_2 source, and had a width and distance consistent within 20% of Gaussian plume theory, we considered it likely due to a flare source. If a plume was not downwind of a flare at a distance consistent with Gaussian

plume theory, or had interference from another CO_2 source, we omitted it from the analysis. 39 flare plumes were identified with the flight notes, and out of 17 additional plumes in the data, 13 were accepted using our verification method and 4 rejected for a total of 52 flare plumes from 37 unique flares.

Other sources for methane or black carbon closely co-located with flares (such as diesel engines or fugitive losses from production wells) could contribute to the observations we are attributing to flaring, and we assess their potential impact on our analysis here. Using gas composition data from over 550 samples, the average chemical plume from the Bakken is 0.7% CO_2, 3.7% N_2, 49% CH_4, 21% C_2H_6, and the rest in higher-order hydrocarbons (*Brandt et al.*, 2015). This results in a molecular weight of about 29 g/mol, close to that of air and nearly double the weight of natural gas from other fields with higher CH_4 ratios (*Weyant et al.*, 2016). An unburned source of gas is therefore neutrally buoyant compared to a hot flare exhaust plume which will rise in the atmosphere (*Beychok*, 2005). However, the flare plume can entrain these other sources, mixing them as the buoyant plume rises in the atmosphere. If we assume a flare converts 98% of its hydrocarbons to CO_2, and that enhancements near a well pad due to other emissions are 50 ppm CH_4 and 415 ppm CO_2, then if the flare plume entrained a volume equal to its own (50% dilution) the resulting CH_4/CO_2 slope measured by the aircraft (see Figure 2.2) would change by less than 1%, smaller than the uncertainty range in fitting the slope. Considering typical values for methane and CO_2 enhancement (40 ppb and 5 ppm on average, respectively), we estimate the slope error (and thus error on calculated emission factors) would be less than 1% with 10% as an upper bound. Adjusting the flare efficiency in this estimation does not significantly affect the result (using a 90% combustion efficiency, all else equal, would also have an impact of 1% on the slope). Although we cannot definitively rule out all potential contributions from such sources to the plumes we are analyzing, these considerations of possible entrainment suggest it is not significant in this analysis,

though the potential impact would suggest our results may represent a lower bound for combustion efficiency.

2.2.3 Combustion Efficiency

Destruction efficiency and emissions factors were calculated for each flare sampled. Black carbon emission factors were determined following the methodology of *Weyant et al.* (2016), using eq. 2.1

$$EF_{BC} = 1000 \times F \frac{C_{BC}}{C_{CO_2} + C_{CH_4} + C_{BC}} \tag{2.1}$$

Here C_{CO_2}, C_{CH_4}, and C_{BC} are the mass concentrations of carbon in g/m^3 for each product with the respective background removed and F is the ratio of carbon mass to total hydrocarbon mass, calculated to be 0.79 from gas composition data for the Bakken (*Brandt et al.*, 2015). CO_2 and CH_4 data were converted from molar ratios to g/m^3 using a molar volume at standard temperature and pressure (273K, 1013 mb) to match the conditions of the BC mass concentrations. This EF_{BC} value is given in grams of BC per kg of gas, and can be converted to g/m^3 using a gas density of 1.23 ± 0.14 kg/m^3 for the composition (*Brandt et al.*, 2015). For some of the flares we did not detect a strong BC enhancement correlated with CO_2, causing skewed or negative emission factor values. To account for this, when the peak enhancement ΔBC was below the detection limit of 4σ of the background, we used a value of half the detection limit in the EF calculation as in *Weyant et al.* (2016); this was observed in a third of the plumes. The measured BC concentrations were scaled up by 15% to account for accumulation-mode mass outside of the SP2 detection range, as described in *Schwarz et al.* (2015); rBC mass in either the coarse mode or a sub-accumulation mode size range would not be accounted for by this adjustment. Generally, as in *Schwarz et al.* (2015), the accumulation mode size distribution is well-fit with a log-normal function, and any additional smaller or larger populations of BC

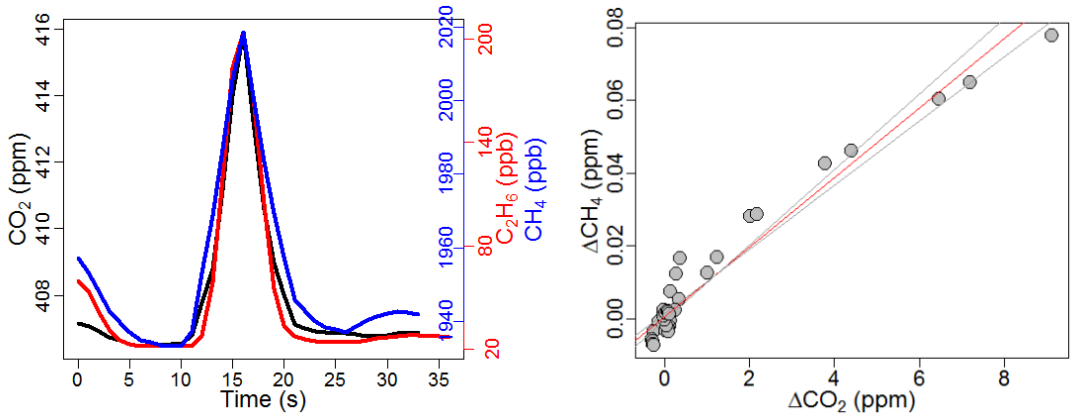

Figure 2.2: Example of a flaring plume with CO_2, CH_4, C_2H_6 time series and regression to find CH_4 EF.

particles are revealed by deviations from the log-normal fit at the smaller or larger limits of the detection range respectively. Here, there was no evidence of additional non-accumulation modes.

Emission factors for CH_4 and C_2H_6 were obtained by first calculating the peak enhancement of CH_4, C_2H_6, and CO_2. We calculated a mean background value for each plume using the concentration data from 5–10 seconds before the start and after the end of the plume, and then subtracted the background from the plume values to obtain ΔCH_4, ΔC_2H_6, and ΔCO_2. ΔCH_4 and ΔC_2H_6 were fit with a Reduced Major Axis (RMA) regression to ΔCO_2 for each peak to obtain the emission factor, in ppm CH_4 or C_2H_6 per ppm CO_2 (*Caulton et al.*, 2014a). Figure 2.2 shows an example plume from a flare and its CH_4 regression. Regressions were well-correlated with 10–20 data points in each flare plume. Uncertainty in EF for CH_4 and C_2H_6 was given by 95% confidence intervals from the regression. For all plumes, EF_{BC} from eq. 1 linearly correlated with the slope of BC vs CO_2 with an R^2 of 0.97. This fit was used to derive uncertainty in EF_{BC} from 95% confidence intervals of the regression of BC and CO_2.

We calculated the destruction removal efficiency (DRE) following the methodology of *Caulton et al.* (2014a) using eq. 2.2, with a small correction to report the value as

the fraction of gas destroyed rather than remaining.

$$DRE(\%) = \left(1 - \frac{\mu CH_4}{((X) * \mu CO_2) + \mu CH_4}\right) * 100 \tag{2.2}$$

μCH$_4$ and μCO$_2$ are the gas concentrations in ppm and X is the carbon fraction of CH$_4$ in the total fuel gas before combustion. From gas composition data for the field (*Brandt et al.*, 2015), the value of X is 0.26 $\pm$ 0.05 for CH$_4$.

This DRE calculation was done two ways. First, by integrating over the entire peak to obtain a DRE value from the total integrated amount of CH$_4$ and CO$_2$. Second, by calculating the DRE value for each point in the peak individually to get an aggregate DRE dataset as seen in *Caulton et al.* (2014a) The respective baseline values were removed from each gas concentration in both methods. Since the integral method calculates DRE using the average concentration over the sampling time of the gases in the plume, and the point-by-point mean represents the average instantaneous DRE, a significant divergence between the results would be indicative of a potential problem with the approach. For all flares the integrated DRE differed from the mean point-by-point DRE by 1% on average, demonstrating robustness between the two methods. C$_2$H$_6$ DRE was also calculated using both methods, with X = 0.23 $\pm$ 0.03 for C$_2$H$_6$. The effect of X's variability on the DRE is small and within the calculated uncertainty for DRE.

2.2.4 Detection Threshold

We compared the standard deviation of CH$_4$ background and the maximum peak CO$_2$ enhancement to calculate a "noise DRE" using eq. 2.2 to assess the impact of a potential signal produced by background variability on the DRE. The distribution suggests a sensitivity threshold around 99%. We compared the sensitivity distribution to the measured DRE distribution, and an analysis of variance between the two produced a p value of 9×10^{-7}, suggesting they are statistically significantly different.

Thus it would be difficult to distinguish measured DRE values of greater than 99% as significant compared to background variability, but values less than 99%, as we have observed, are robustly detectable with our approach. There is a trade-off between our sampling approach and the one used by *Caulton et al.* (2014a), where they flew lower and closer to the flares. With our flights, we obtained more points in each plume, allowing us to calculate regression lines for emission factors. However, we encountered a lower signal-to-noise ratio, making it more difficult to precisely measure the DRE of very efficient flares. We used the difference between 100% and the DRE calculated using the sensitivity as a proxy for DRE uncertainty in each individual flare.

2.3 Results

2.3.1 Emission Factors

Figure 2.3 shows the calculated CH_4 and C_2H_6 emission factors plotted against mean aircraft-level wind speed for all flare plumes. Previous laboratory flare studies have observed a strong nonlinear dependence of inefficiency on crosswind speed (*Johnson and Kostiuk*, 2000, 2002), and *Caulton et al.* (2014a) observed a weak relationship in the flares they sampled in the field. Considering our observed emission factors and crosswind speeds we find similar results to *Caulton et al.* (2014a). An exponential fit of our data suggests a weak dependence, with parts of the data possibly following different distinct curves. A Pearson correlation analysis of the data and the exponential fit produced a weak correlation coefficient (0.34). Gas exit velocity and flare parameters like the stack diameter can affect the inefficiency curve and may be the reason for the apparent presence of multiple curves, but unfortunately these values were not known for our sampled flares. More specific knowledge of the gas composition and flow rate would potentially be illuminating for the possible bimodal distribution in CH_4 EF of low-efficiency emitters (>30 ppb/ppm) and high-efficiency

emitters (0–20 ppb/ppm) but we can only hypothesize without detailed information on specific flares at time of our sampling.

Some flares were circled repeatedly or revisited on different days, and so we transected multiple plumes from the same flare. The calculated EF for the flare was not consistent between different plumes, suggesting fluctuation in the efficiency. *Caulton et al.* (2014a) found large overall variability in CH_4 EF and inconsistency between sampling on different days, but attribute the variability to the small sample size of their plumes. *Weyant et al.* (2016) reported inconsistent emissions of BC for flares sampled on different days, and observed large variability in BC EF for multiple passes of the same flare, citing variability in gas flow rate and gas composition as possible sources. From our data alone we cannot resolve the cause of same-flare variability, but it is apparently a feature consistent across studies.

We did not observe a clear relationship between EF and wind speed for plumes from the same flare, possibly due to factors like flow rate or exit velocity. For some flares that were sampled multiple times, we did not get a sharp, identifiable peak in CO_2 or CH_4 on every pass, and so we were not able to analyze all possible passes. The EF calculation included background points in the regression, removing these points from the fit and forcing the line through zero did not significantly affect the results. Comparing CH_4 and C_2H_6 emission factors for each plume, we found a linear relationship with a R^2 value of 0.57, as plumes with higher emissions of CH_4 had corresponding higher emissions of C_2H_6, suggesting that combustion efficiency is somewhat uniform across hydrocarbons.

Like *Weyant et al.* (2016), we did not observe a dependence between BC emission factor and CH_4 EF for each plume. Elevated CH_4 emissions from a flare do not necessarily indicate higher or lower BC emission. Adding in an ethane term to eq. 2.1 did not significantly change the BC EF calculation, as the ppm-order enhancement of CO_2 dominates the ppb-order enhancement of C_2H_6 and CH_4.

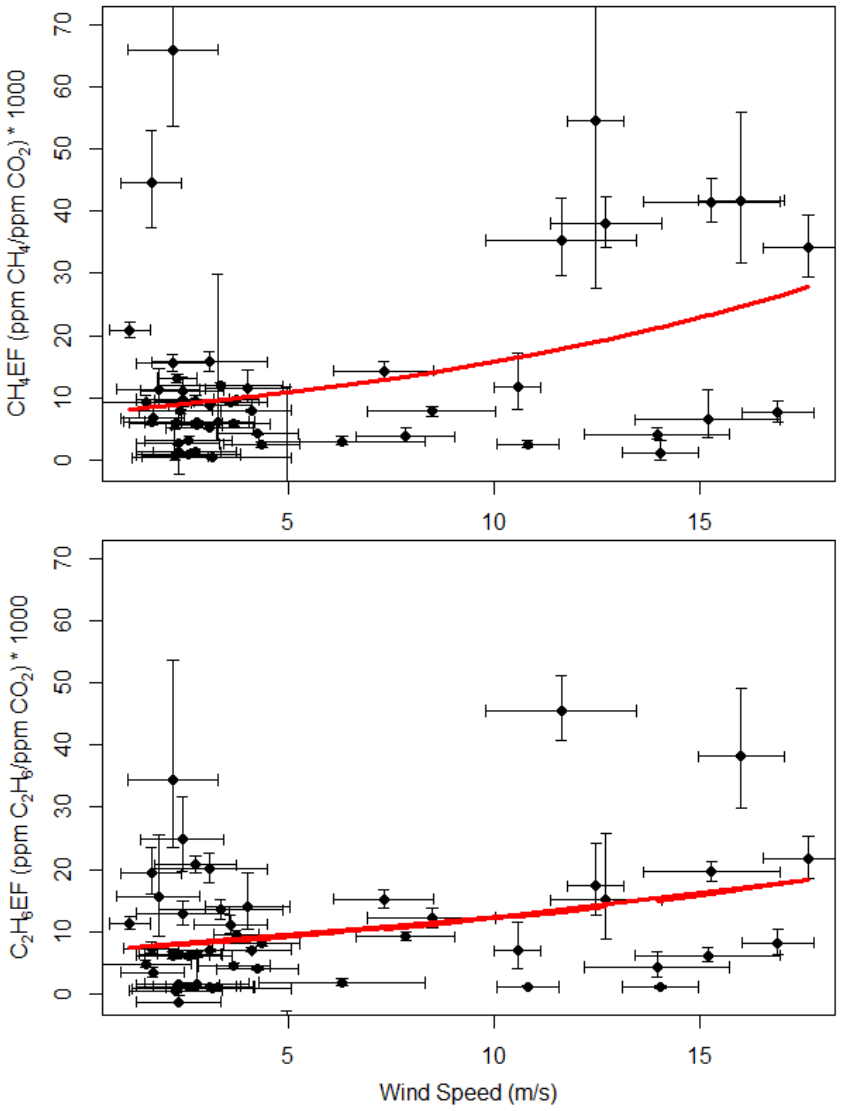

Figure 2.3: CH_4 and C_2H_6 EF plotted against wind speed for all plumes, with an exponential fit in red. Error bars represent 95% confidence intervals in EF and 1σ in wind speed.

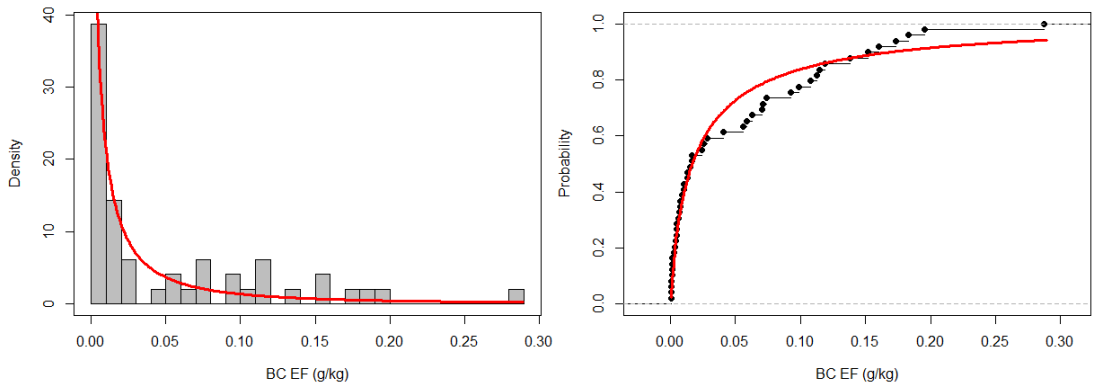

Figure 2.4: On the left, a histogram of black carbon emission factor for all flare plumes, with log-normal density (red line). On the right, distribution function of BC EF in black with log-normal distribution function in red.

Figure 2.4 shows the distribution and probability function of BC emission factor in g BC/kg gas. The distribution is right-skewed, matching the results of *Weyant et al.* (2016), and was fit with a log-normal density using a maximum-likelihood method. The log-normal distribution function is given by

$$f(x) = \frac{1}{\sqrt{(2\pi)}\sigma x} e^{-((logx-\mu)^2/(2\sigma^2))} \tag{2.3}$$

μ and σ are the mean and standard deviation of the logarithm. A Pearson correlation analysis between the BC emission factor probability distribution and the log-normal distribution resulted in a correlation coefficient of 0.96. We present the log-normal fit as a way to illustrate the skewed distribution and provide a quantitative representation. Results derived from the combustion efficiency distribution use the raw distribution, rather than an approximation with the log-normal fit.

We report BC EF from flares in g/kg, grams of BC produced per kilogram of hydrocarbons in the fuel gas. The values ranged from 0.0004 to 0.287 g/kg. We can convert from g/kg to g/m^3 using a flared gas density of 1.23 $\pm$ 0.14 kg/m^3 (*Brandt et al.*, 2015), allowing us to express BC EF in terms of gas flared volume and to compare the results with previous studies. Even with the observation of a right-

skewed distribution, our analysis finds lower BC emissions than previously reported. *Schwarz et al.* (2015) provided an estimate for all the BC sources in the Bakken of 0.57 ± 0.14 g/m^3. This upper bound on flaring is twice the highest emission value we observed (Figure 2.4). Similarly, laboratory analysis by *McEwen and Johnson* (2012) reported emissions much larger than we observe (0.51 g/m^3, off scale in Figure 2.4). The mean value of 0.13 ± 0.36 g/m^3 measured with an SP2 by *Weyant et al.* (2016) is within our observed range, though it falls within the top 20% of emitters we observed. Our observed in-field flares thus appear to have produced less BC than would be predicted from previous studies. The median, mean, and standard deviation of the mean BC emission factor we observed were 0.021 g/m^3 and 0.066 ± 0.009 g/m^3 (or 0.017 g/kg and 0.053 ± 0.008 g/kg), respectively, though given the skewed distribution care needs to be taken in interpreting these values. Given that 3.7 BCM of gas was flared in the Bakken field in 2014 (*North Dakota State Government*, 2016), applying that to the entire distribution of BC EF in g/m^3 suggests total BC emissions from flaring of 0.24 Gg BC/yr. However, the top quartile of flares contribute disproportionately, 0.17 Gg BC/yr, which is 70% of the total emissions from flares. Overall, our emission rate of 0.24 Gg BC/yr is two-thirds the rate of 0.36 Gg BC/yr calculated by *Weyant et al.* (2016) for flares and 17% of the total Bakken emission rate (1.4 Gg BC/yr) reported by *Schwarz et al.* (2015). Based on these results, using a single emission factor to estimate emissions from flares in a region does not properly represent the wide variability in emissions that may be present. Total emissions from flaring could potentially be substantially reduced if the least efficient flares alone are identified and addressed.

2.3.2 Combustion Efficiency

For methane and ethane, the percent of gas remaining provides a useful metric for flare efficiency—this is simply 100-DRE. In Figure 2.5 the distribution of percent

remaining CH_4 and C_2H_6 is illustrated and a log-normal relationship is apparent. As with emission factors, we found a linear relationship between CH_4 and C_2H_6 DRE for each plume, with a R^2 of 0.53.

A Pearson correlation analysis of the DRE probability distributions and the log-normal fit distribution produced a correlation coefficient of 0.99 for both CH_4 and C_2H_6. The distribution of CH_4 and C_2H_6 emission factors, which are theoretically consistent with the DRE calculations, also exhibit a skewed distribution though a log-normal relationship is not as apparent. The median DRE for CH_4 is 97.14 ± 0.37 using the integral method and 96.99 ± 0.23 using the aggregate dataset. For C_2H_6 the median DRE is 97.33 ± 0.27 and 97.36 ± 0.25 respectively. These median values are close to the expected efficiency (98%), but the right-skewed distribution indicates that 98% is not a representative destruction efficiency and would over-predict methane and ethane destruction.

We can assess the impact of this observed skewed distribution by considering the contribution of incomplete flare combustion to total field methane and ethane emissions. Using aircraft data and a mass balance technique, *Peischl et al.* (2016) calculated a methane flux for the Bakken region that extrapolates to an annual flux of 0.25 ± 0.05 Tg CH_4/yr. As with black carbon, we can use reported flaring gas volumes for North Dakota in 2014 (*North Dakota State Government*, 2016) and integrate the distribution of observed DRE values to produce an estimated emission of methane from incomplete combustion of 0.052 Tg CH_4/yr, or $21\% \pm 4\%$ of the total emissions reported by *Peischl et al.* (2016), using the uncertainty bound on the flux calculation. This is more than double the contribution one would find if the expected value of 98% was assumed representative of the field, which would predict emissions representing $8\% \pm 1.6\%$ of the total field emissions. *Caulton et al.* (2014a) reported much higher combustion efficiencies, and applying their median 99.98% value would suggest only a fraction of a percent ($0.13\% \pm 0.03\%$) of the total field emissions was from incomplete

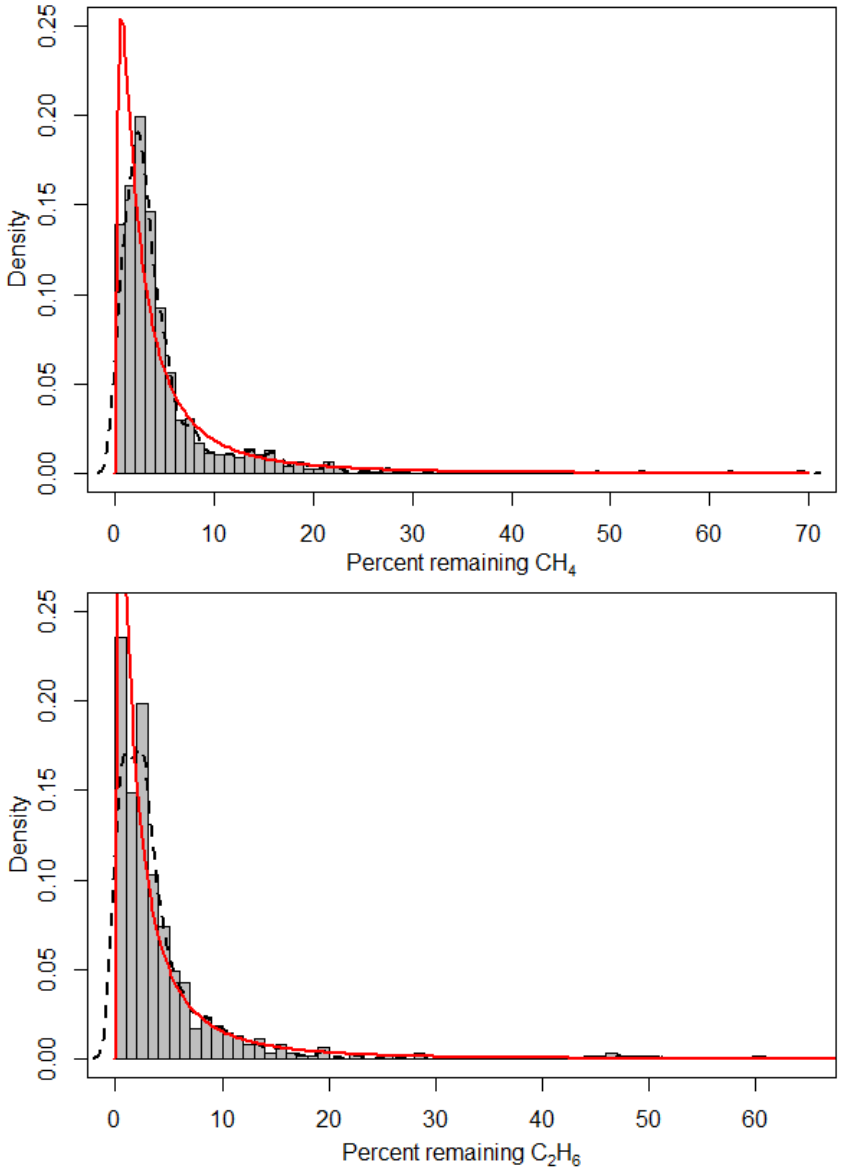

Figure 2.5: Histogram of remaining CH_4 and C_2H_6 (100-DRE) with density curve (dashed black) and log-normal fit (red). These distributions were integrated to calculate the emissions due to incomplete combustion.

combustion in flares.

We performed the same analysis for ethane, and compared with the total field emissions estimate of 0.23 ± 0.07 Tg C_2H_6/yr reported in *Kort et al.* (2016). Again our observed combustion efficiencies suggest incomplete combustion from flares contributes substantially to total field emissions, 17% ± 5% of the total emissions (0.039 Tg/yr), more than double that predicted by using 98% as a representative value.

The observed log-normal distribution results in a disproportionate impact from flares exhibiting poor combustion efficiencies. We find the top quartile of methane emitters contribute 0.036 Tg CH_4/yr, which is 69% of total emissions from incomplete flare combustion (and 14% of the total field emissions). Similarly, for ethane, the top quartile of emitters contributes 0.026 Tg C_2H_6/yr which is 66% of the total emissions from incomplete flare combustion (and 12% of total field emissions).

Why do we find higher methane emissions and lower black carbon emissions than other studies conducted in the Bakken shale (*Weyant et al.*, 2016; *Caulton et al.*, 2014a; *Schwarz et al.*, 2015)? We cannot definitively pinpoint the reason. We sampled in the same subregion of the Bakken as *Caulton et al.* (2014a), though we did not sample any of the same flares they did, and our campaign was 2 years after theirs. *Weyant et al.* (2016) did not report specific flare locations but were likely in the same subregion as well, 2 months before our campaign.

There is a difference in sampling methods, which could contribute. *Caulton et al.* (2014a) flew low and close to the flares, though specific altitudes and distances are not reported. As we did not specifically target larger (and so potentially more efficient) flares, our approach makes it more likely to sample higher emitting flares. *Weyant et al.* (2016) also likely flew closer to the flares than we did, though at a slower speed (45 m/s) than at which we typically sampled (65 m/s). We did not observe a clear correlation between sampling distance and combustion efficiency in our data, but it certainly affects variables such as plume entrainment, other emissions sources,

turbulence, and environmental factors.

The largest source of discrepancy in results is likely that relatively few flares have been sampled: 26 (85 passes) by *Weyant et al.* (2016), 10 by *Caulton et al.* (2014a), and 37 (52 passes) in our study, and thus there is large representation error. In our study we attempt a statistical sampling for greater representativeness, but given that there were over 5500 wells with reported flaring in the Bakken in 2014 (*North Dakota State Government*, 2016), 37 independent flares only represents 0.6% of active flares. Thus, we think our results should be considered in concert with the Weyant and Caulton analyses, and our data should be considered in aggregate. In doing so, it would subtly change our total estimated contribution (lower for methane and higher for black carbon), but the observed log-normal distribution result would not change.

2.4 Global Implications

Our sampling provides sufficient statistics to observe a heavy-tail distribution of combustion efficiencies. This heavy-tail characteristic has been observed and reported for methane emissions from the oil and gas sector (*Yuan et al.*, 2015; *Subramanian et al.*, 2015; *Mitchell et al.*, 2015; *Allen*, 2014; *Frankenberg et al.*, 2016b), but this represents a first observation of the heavy-tail for flaring emissions of methane and ethane. This has important implications for current and future contributions from flaring activities. To illustrate, let us consider if our observed distribution were globally representative. Globally, 143 BCM of gas is flared annually (*Elvidge et al.*, 2016). If 98% destruction removal efficiency were representative of every flare, that would correspond to a range in methane emissions of 1.14–1.90 Tg CH_4/yr for a gas composition range of 60%–100% CH_4. Applying our observed distribution, that range changes to 2.78–4.64 Tg CH_4/yr, more than doubling the amount emitted. In assessing the climate and air quality impacts of flaring, it is critical that skewed distributions are accounted for in the cases of methane, ethane, and black carbon. Although our spe-

cific observed emissions factors and efficiencies are likely only representative of the Bakken field, the observations of a skewed distribution is likely general.

CHAPTER III

FCHAOS: Frequent Calibration High-performance Airborne Observation System for continuous N_2O, CO_2, CO, and H_2O measurements

Abstract

We present the development and assessment of a new flight system that uses a commercially available continuous-wave, tunable infrared laser direct absorption spectrometer to measure N_2O, CO_2, CO, and H_2O. When the commercial system is operated in an off-the-shelf manner, we find a clear cabin pressure/altitude dependency for N_2O, CO_2, and CO. The characteristics of this artifact make it difficult to reconcile with conventional calibration methods. We present a novel procedure that extends upon traditional calibration approaches in a high-flow system with high-frequency, short-duration sampling of a known calibration gas of near-ambient concentration. This approach corrects for cabin pressure dependency as well as other sources of drift in the analyzer while maintaining a ∼90% duty cycle for 1 Hz sampling. Assessment and validation of the flight system with both extensive in-flight calibrations and comparisons with other flight-proven sensors demonstrate the validity of this method.

In-flight 1σ precision is estimated at 0.05 ppb, 0.10 ppm, 1.00 ppb, and 10 ppm for N_2O, CO_2, CO, and H_2O respectively, and traceability to WMO standards (1σ) is 0.28 ppb, 0.33 ppm, and 1.92 ppb for N_2O, CO_2, and CO. We show the system is capable of precise, accurate 1 Hz airborne observations of N_2O, CO_2, CO, and H_2O and highlight flight data illustrating the value of this analyzer for studying N_2O emissions on $\sim$100 km spatial scales.

3.1 Introduction

Continuous, 1 Hz airborne observations of atmospheric greenhouse gases and pollutants provide essential information for direct quantification of emissions (*Karion et al.*, 2015; *Peischl et al.*, 2015a; *Smith et al.*, 2015; *Kort et al.*, 2016), assessment of modeled representations of emissions and transport (*Wofsy*, 2011; *O'Shea et al.*, 2014), and validation of remote sensing observations (*Tanaka et al.*, 2016; *Inoue et al.*, 2016; *Frankenberg et al.*, 2016a). Advances in the last decade have facilitated widespread, high-precision, high-accuracy continuous airborne observations of CH_4, CO_2, CO, and H_2O (*Chen et al.*, 2010; *Karion et al.*, 2013; *Filges et al.*, 2015). These observations have proven particularly valuable for quantifying emissions from individual, large emitting point sources (*Conley et al.*, 2017; *Mehrotra et al.*, 2017) as well as constraining emissions of highly heterogeneous processes on 10–100 km scales (*Karion et al.*, 2015; *Peischl et al.*, 2015a; *Smith et al.*, 2015; *Kort et al.*, 2016). Continuous, 1 Hz airborne sampling of N_2O with high accuracy and precision has proven more elusive, with limited aircraft campaigns reporting continuous airborne N_2O (*Kort et al.*, 2011; *Wofsy*, 2011; *Xiang et al.*, 2013), systems being large and challenging to operate with frequent attention to supplies of cryogens (*Santoni et al.*, 2014), and newer systems showing large cabin pressure dependencies (*Pitt et al.*, 2016).

N_2O is a potent greenhouse gas with natural and anthropogenic sources, and is

currently the single most impactful anthropogenic ozone-depleting substance actively emitted to the atmosphere (*Ravishankara et al.*, 2009). Atmospheric emissions of N_2O have been steadily rising over time (*Myhre et al.*, 2013), but attempts to better quantify, understand, and constrain anthropogenic emissions have been hindered by high uncertainties in model estimates and limited observational constraints (*Ciais et al.*, 2013; *Davidson and Kanter*, 2014). The poor understanding of N_2O emissions processes is attributable to a combination of high spatial and temporal variability (*Monni et al.*, 2007) that is hard to observe and represent, and a lack of direct observational data of emissions sources (*Brown et al.*, 2001). The largest source of anthropogenic N_2O, contributing 66% of global N_2O emissions, is agricultural activity (*Davidson and Kanter*, 2014). Some of these emissions are a direct product of human activity, such as the fertilizer production process, which has grown to 100 Tg N yr^{-1} since the development of the Haber-Bosch process in 1908 (*Erisman et al.*, 2008). Other anthropogenic emissions, such as from applied fertilizer, are harder to observe and represent as environmental factors including soil moisture, temperature, and crop type all influence emissions (*Dalal et al.*, 2003; *Ruser et al.*, 2006; *Griffis et al.*, 2017).

A diverse range of approaches have been utilized in attempts to measure N_2O emissions (*Denmead*, 2008; *Rapson and Dacres*, 2014). Flux chambers can quantify emissions from areas on the order of square meters (*Bouwman et al.*, 2002; *Marinho et al.*, 2004; *Turner et al.*, 2008; *Chadwick et al.*, 2014). Given the heterogeneity in N_2O emission processes, extrapolation of limited flux chambers to accurately represent domains on the orders of 10–100 square km remains challenging (*Pennock et al.*, 2005; *Flechard et al.*, 2007). The eddy covariance approach deploys sensors on towers to estimate fluxes on a 1–10 km^2 scale (*Dalal et al.*, 2003; *Pattey et al.*, 2007), but not beyond that range, thus encountering similar representation challenges as flux chambers. Bottom-up modeling of emissions processes (*Del Grosso et al.*, 2006; *Tian et al.*, 2015) can represent emissions at a range of scales. The models are typically

trained and evaluated with data from flux chambers and then simulate emissions at a continental to global scale. Evaluation of these representations then can happen at the larger scales, where top-down atmospheric inversions (*Kort et al.*, 2008, 2011; *Miller et al.*, 2012; *Thompson et al.*, 2014; *Chen et al.*, 2016; *Griffis et al.*, 2017; *Nevison et al.*, 2018) have challenged modeled and inventoried emissions and often found large discrepancies exceeding 100% (*Miller et al.*, 2012). To better understand these divergences as well as to properly assess the representation of flux chamber and eddy covariance measurements, we need observational constraints at 10–100 square km spatial scales.

Continuous, 1 Hz airborne measurements can provide information at this critical spatial scale, in addition to providing observational constraints for large point sources (N_2O fertilizer production facilities present a potentially important source of N_2O emissions). To get good, useful data, aircraft studies require instruments that have high precision, a fast response time, and are relatively robust to changes in the environment (*Fried et al.*, 2008). Continuous-wave tunable infrared laser direct absorption spectrometers (CW-TILDAS) can satisfy those requirements and are an appropriate choice for airborne instrumentation (*Rannik et al.*, 2015).

Infrared laser spectrometers have been widely used in airborne studies. They often employ an in-flight calibration to correct for spectral drift that can occur over several hours of measurement (*O'Shea et al.*, 2013; *Santoni et al.*, 2014). Zero air with no gases in the absorption spectrum can also be used to adjust the spectral baseline for more accurate measurements, particularly if the desired gas has a weak absorption feature (*Yacovitch et al.*, 2014; *Smith et al.*, 2015). One recent study to measure N_2O emissions with such an instrument reported their assessment of its performance and found artifacts in the data primarily due to changes in airplane cabin pressure (*Pitt et al.*, 2016), significantly impacting the duty cycle of the analyzer and its utility during vertical profiles. To deploy a CW-TILDAS for N_2O observation as in *Pitt et al.*

(2016), problems can arise if drifts occur on a timescale faster than the conventional calibration period of 0.5–1 hour. Also, at low flow rates (0.1–1 slpm), N_2O can take a long time to equilibrate, and this can have a negative impact on the instrument's duty cycle (*Santoni et al.*, 2014). The efficacy of airborne instrumentation for N_2O measurements would benefit from improvements to such limitations.

We present the Frequent Calibration High-performance Airborne Observation System (FCHAOS), utilizing a TILDAS instrument and an updated calibration technique, to make N_2O measurements that can be utilized for calculating facility emissions, mass balance fluxes, and regional inversions. Rather than relying on spectral zeros and infrequent in-flight calibrations to correct for drift on large time-scales, we use short, frequent calibration measurements to resolve both long-term spectral drift and short-term environmental effects. This research was part of the Fertilizer Emissions Airborne Study (FEAST) campaign in spring 2017 targeting N_2O and other greenhouse gas emissions in the southern Mississippi River Valley region of the USA. In this manuscript we discuss the operation and set-up of the instrumentation involved in the airborne flight system. We discuss test flights done to assess the off-the-shelf operation and the associated flaws. We then present our solution to improve instrument performance with short, frequent calibrations and validation by in-flight calibrations and comparison with a flight-proven Picarro cavity ring-down spectrometer.

3.2 Instrumentation

3.2.1 CW-TILDAS description

The core of our system is an Aerodyne mini spectrometer. The spectrometer uses a mid-IR, continuous-wave, distributed feedback laser with a frequency of 2227 cm^{-1} (nanoplus, Germany). The laser is mounted on a copper Peltier device which keeps

the laser temperature stable at ∼17 °C and is regulated by a thermoelectric chiller held at 23 °C (Oasis 3, Solid State Cooling, USA). This laser is optically aligned into a 0.5 L astigmatic mirror multipass absorption Herriott cell (*McManus et al.*, 1995). The refraction pattern in the cell is optimized to produce a total path length of 76 meters before the beam exits the cell and is aligned into a photodetector. The cell itself is sealed and held at ∼40 Torr. The space outside of the cell is subject to variations in external pressure. The laser's output frequency can be adjusted by ramping the current, sweeping across a frequency range of approximately 2227.4–2227.9 cm^{-1}. This range contains transition lines for H_2O, CO_2, CO, and N_2O, allowing the photodetector to measure the laser transmission intensity at each of these transitions (*Nelson et al.*, 2002).

The mole fractions of N_2O, CO_2, CO, and H_2O are reported using the TDLWintel software as described in *Nelson et al.* (2002) and *Nelson et al.* (2004). The retrieval uses the Beer-Lambert law, where the absorption intensity, path length, and molar absorptivity enable calculation of gas mixing ratio. The absorption spectrum is fit in real-time with a Voigt density profile using the Levenberg-Marquardt algorithm, allowing retrievals at 1 Hz (*Nelson et al.*, 2004). The exact frequencies of the line transitions and absorption cross-sections are obtained from the HITRAN2012 database (*Rothman et al.*, 2013). Pressure and temperature data acquired from sensors in the cell are used to account for broadening effects in the fit.

3.2.2 Set-up and payload

We integrated the FCHAOS system on a single-engine Mooney M20R aircraft from Scientific Aviation. Figure 3.1 shows the flow diagram for our system. The inlet line to the instrument is ∼5 m PVDF Kynar tubing. The inlet line is rear-facing on the right wing to reduce liquid and particle contamination of the line, with the plane exhaust located on the left wing, minimizing exhaust contamination. A membrane

disc filter (Pall, USA) is also used to block particulates from entering the cell. Using a mass flow controller (MC-5SLPM-D, Alicat Scientific, USA), we set a flow rate of 1.5 slpm. The MFC is placed downstream of the filter to prevent damage due to rogue particulates. The instrument cell is pressurized on the ground to 40 Torr using a dry scroll pump (IDP-3, Agilent Technologies, USA) and a needle valve (SS-1RS4, Swagelok, USA) directly upstream of the pump for adjusting the target pressure given a defined mass flow rate. The use of mass flow control enables rapid switching between calibration gas and ambient air without inducing pressure fluctuations or ringing in the cell. The mass flow control setup is a closed system (no excess flow), thus ensuring no contamination of other inlets and minimal waste of calibration gas. Pressure-control systems that are optimally tuned may achieve similar performance, but even with an excess flow to reduce pressure pulses, it is difficult to reach similar performance as with mass flow control. Figure 3.2 illustrates respective performance in-flight of a pressure and mass flow control configuration for our instrument. Two 2 L aluminum carbon-fiber-wrapped compressed air cylinders are securely strapped in the plane. These tanks are outfitted with stainless steel regulators (51-14B-590, Air Liquide, USA) and stored calibration gases. Two three-way solenoid valves (009-0294-900, Parker-Hannifin, USA) control the air flow between the tanks and the inlet line.

The additional payload is set up on the Mooney as described in *Conley et al.* (2014) and *Conley et al.* (2017). Temperature and relative humidity are recorded with a humidity probe (HMP60, Vaisala, Finland). A cavity ring-down spectrometer (G2301-f, Picarro, USA) measures CH_4, CO_2, and H_2O as described in *Crosson* (2008). Ozone is measured with an ozone monitor (Model 202, 2B Technologies, USA). Wind speed and direction are calculated using a differential GPS method as in *Conley et al.* (2014). The Mooney aircraft is not pressurized, so the instrument experiences pressure variation as the aircraft profiles.

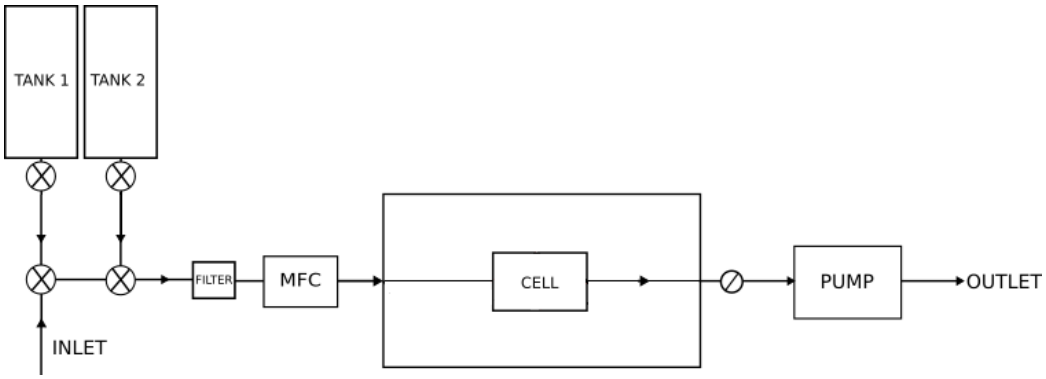

Figure 3.1: Schematic of FCHAOS, where air flows from the inlet line through the solenoid valves, past the filter to the mass flow controller (MFC), through the instrument cell, a needle valve, and finally the vacuum pump. When calibrating the solenoid valves are actuated to direct flow from each individual calibration tank into the cell directly.

Lag time between when air enters an instrument's inlet line and when it is measured in the cell is determined by breathing close to the inlet tube and recording sharp rises in CO_2 and H_2O mixing ratios. For FEAST lag times were measured at 3 s and 5 s for the FCHAOS and Picarro G2301-f respectively, values confirmed in flight by comparing variability with temperature and RH data from the humidity probe. These lag times are used in post-processing to match avionics and GPS data with the co-located molar ratios from the FCHAOS and G2301-f. Though lag times will vary with altitude, given the flow-rates, inlet line volumes, and altitude range of the Mooney aircraft it is essentially constant for the data presented in this manuscript.

3.2.3 Calibration

We performed pre-flight calibrations on the ground for both the FCHAOS and Picarro G2301-f using two air cylinders calibrated to a NOAA WMO greenhouse gas scale (X2007, X2004A, X2014A, X2006A for CO_2, CH_4, CO, and N_2O respectively) (*WMO*, 2015). Both cylinders had mixing ratios of CO_2 (*Zhao et al.*, 1997; *Zhao and Tans*, 2006; *Tans et al.*, 2017), CH_4 (*Dlugokencky et al.*, 2005), CO (*Novelli et al.*, 2003), and N_2O (*Hall et al.*, 2007) near ambient atmospheric levels, with one as a

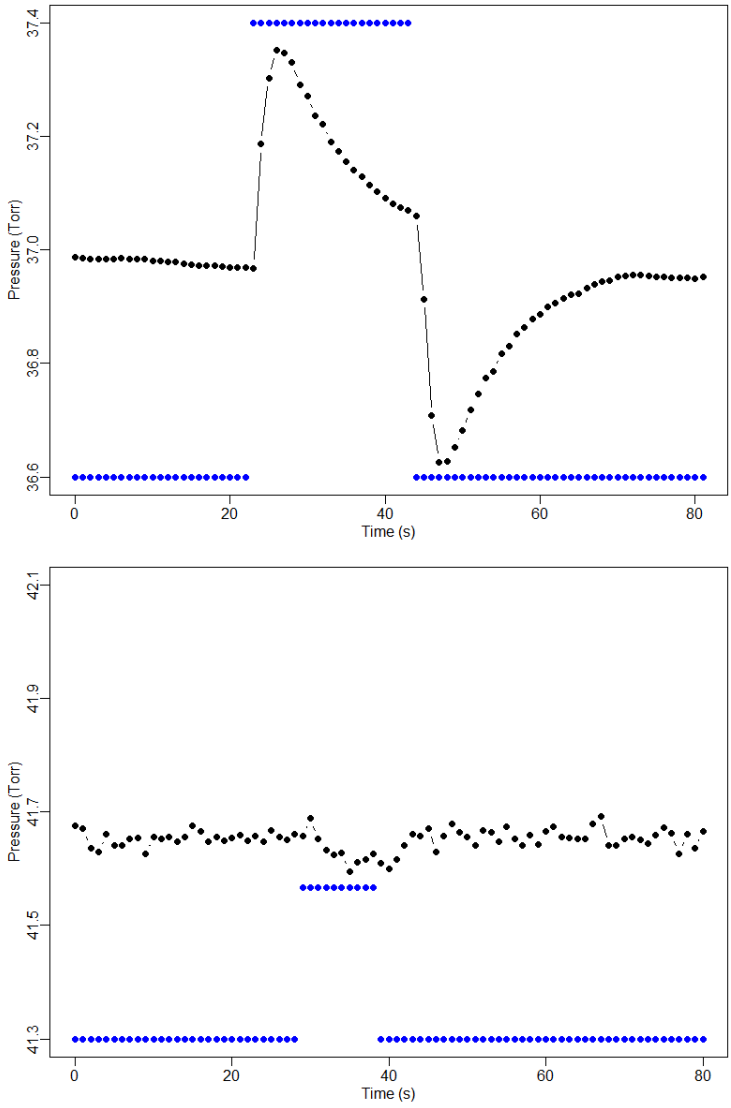

Figure 3.2: Cell pressure (black) in response to actuating a solenoid and sampling a standard cylinder (blue indicates solenoid position). The pressure control setup (top panel), including excess flow, exhibits significant pressure perturbations and residual transients that persist longer than desired calibration time. The mass flow control setup (bottom panel) shows pressure perturbations of shorter duration and on the order of 0.04 Torr, 20 times smaller than with pressure control.

high-span standard and the other as a low-span.

We sequentially sampled these cylinders for multiple cycles, and compared the measured mixing ratios for each gas to the reported value on the WMO scale. We consider known values X_{true} against the measured values $X_{measured}$, and a linear fit provides the slope m and intercept b such that $X_{true} = m^*X_{measured} + b$.

We filled the two in-flight calibration tanks used with the FCHAOS for FEAST with a separate custom mixture that contained atmospheric levels of N_2O, CO_2, and CO. We calibrated the mixing ratios using the WMO standard cylinders by sampling the target cylinders in between the WMO standards. During flights, we used one tank as a single-point calibration gas, while the other was used as a check gas to assess the instrument's traceability. We elaborate on these processes in Sect. 3.3.2 and 3.4.1.

We assessed the stability in slope of the instrument by performing calibrations separated by months before and after the FEAST campaign. Over the course of four months, the slopes for N_2O, CO_2, and CO changed by 0.4%, 0.01%, and 0.5%. The impact of any variation in slope depends on the difference between ambient levels and calibration gas values. For the operation of FCHAOS, we use calibration gas with mixing ratios near ambient levels. Typical atmospheric ambient levels of N_2O are ∼335 ppb, so with a calibration gas at ∼330 ppb, the long-term variation due to linearity is 0.4% of 5 ppb, or 0.02 ppb, an uncertainty that is within our 1 Hz precision as reported in Sect. 3.4.1. For CO_2 and CO, which have ambient atmospheric levels of ∼400 ppm and ∼155 ppb, we use calibration gases with ∼390 ppm and ∼150 ppb, and the impacts due to variation in slope are 0.01 ppm and 0.025 ppb, respectively. If zero air were used instead, the impact on N_2O would be on the order of 0.4% of 335 ppb, or 1.3 ppb, an order of magnitude larger, with similar impacts for CO_2 and CO. By using calibration gases close to ambient levels we eliminate our sensitivity to drift in the instrument's slope and thus can a single gas target for in-flight calibration to correct only for intercept variability.

3.2.4 Water vapor

Spectroscopic measurements of atmospheric species are sensitive to dilution and broadening effects due to water vapor (*Chen et al.*, 2010, 2013; *Rella et al.*, 2013). TDLWintel, in its retrieval algorithm, corrects for water dilution and uses H_2O broadening coefficients to mitigate the effect of water vapor on the spectral lines, directly reporting dry molar fractions for N_2O, CO_2, and CO (*Lebegue et al.*, 2016; *Pitt et al.*, 2016). This coefficient is the ratio of spectral line broadening due to water pressure compared to air pressure broadening. To determine the coefficients, we conducted a test where dry tank air was sampled with varying amounts of water vapor. We used a similar approach as in *Lebegue et al.* (2016). We used a moist filter along with variable flow through parallel dry tubing, enabling some control of the water vapor content by modulating the relative flows over the moist filter compared to the dry tubing. We sampled at varying humidity starting at $\sim$1.6% H_2O and decreasing to near 0, spanning a typical range of atmospheric water vapor. Using spectral playback in TDLWintel, we were able to re-analyze the spectra with various broadening coefficients until we found the optimum values as in *Pitt et al.* (2016). Figure 3.3 shows the measurement data from the test using our optimized broadening coefficients of 1.33, 1.93, and 1 for N_2O, CO_2, and CO, respectively. The dry value is determined from prolonged sampling of dry air only from the standard tank. The deviation from this is shown as a function of water vapor. The gray line shows a moving average with a 10 s window. The RMS difference in N_2O, CO_2, and CO was 0.023 ppb, 0.076 ppm, and 0.75 ppb, respectively. These are used as the uncertainty in water vapor correction, as in *Pitt et al.* (2016). For CO, a coefficient of 1 corresponds to purely a dilution correction. Larger values of the coefficient do not improve the dependency. As highlighted by *Pitt et al.* (2016), water broadening coefficients must be determined by users for their own instrument as these can vary for each analyzer and can introduce substantial errors in correcting to dry air mole fraction.

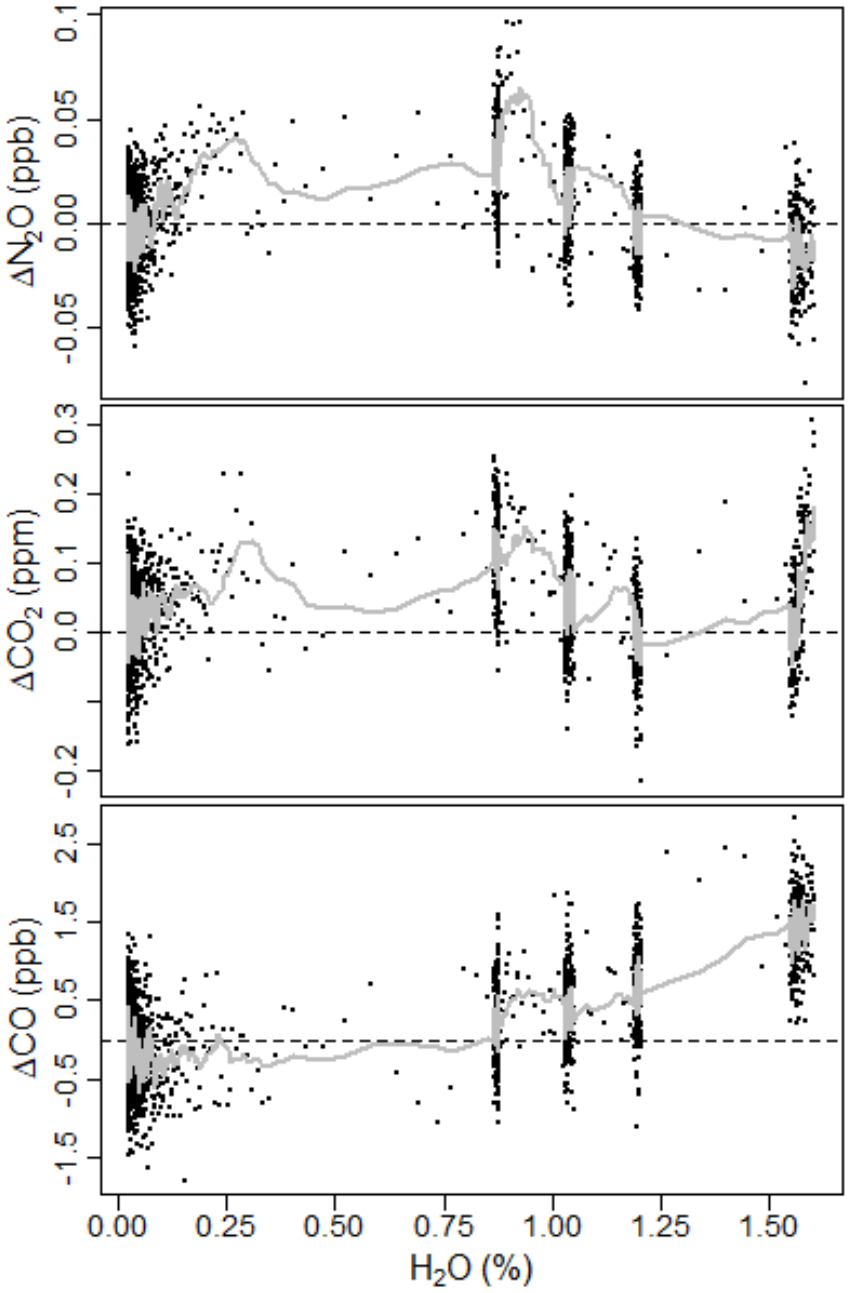

Figure 3.3: Residual uncertainty in water vapor correction for N_2O, CO_2, and CO with broadening coefficients of 1.33, 1.93, and 1, respectively. Black dots are the deviation from the dry value, with a moving average (10 s) depicted in gray.

3.3 In-flight operation

3.3.1 Null Test

For an instrument to be well-suited for airborne observation, resistance to environmental effects is paramount. A "null test," where an instrument samples air with known mixing ratios in flight while subject to variation in cabin pressure, air temperature, etc., can be useful in evaluating its robustness as shown in *Chen et al.* (2010) and *Karion et al.* (2013). We conducted two null tests using the FCHAOS, once during a test flight in Colorado, once during a research flight in our target region in the lower Mississippi River basin. Figure 3.4 shows N_2O, CO_2, and CO mixing ratios observed by the FCHAOS while sampling tank air during a vertical profile descent. As the altitude decreases, there is a clear dependence due to the cabin pressure changing similar to what was reported in *Pitt et al.* (2016). As mentioned in Sect. 3.2, though the cell is pressurized, the rest of the instrument is not, and since the aircraft cabin is not pressurized, our system thus experiences any change in ambient pressure. Correcting or mitigating this cabin pressure artifact is necessary for FCHAOS to be capable of accurate airborne in-situ sampling.

3.3.2 Frequent calibration correction

The cause of the cabin pressure dependence is not immediately evident. One possible explanation could be an optical fringe pattern in the absorption spectrum that moves with changing cabin pressure. Acceleration during altitude change could also create g-force or electrical (via engine surges) changes that propagate through the instrument system. Without needing to pinpoint the cause, we know the time period of the artifact presents on the order of many minutes, with a typical aircraft climb rate of 500 ft/min. Thus a correction that occurs on a shorter time spacing could remedy the drift. To account for both spectral drift in the instrument that

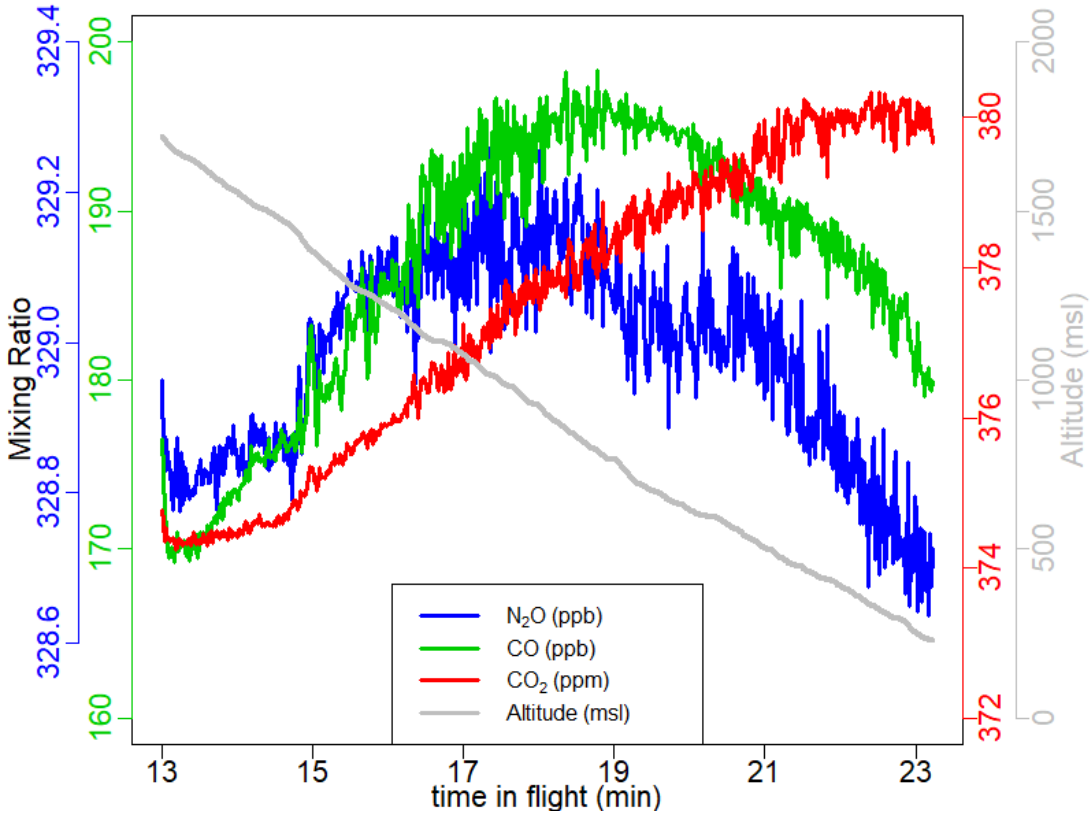

Figure 3.4: A null test demonstrates artifacts when operating the instrument in an off-the-shelf manner. Drift occurs in N_2O, CO_2, and CO due to changes in cabin pressure that occur with changing aircraft altitude.

occurs on the order of hours and cabin pressure-related artifacts that emerge on the order of minutes, we developed an empirical correction procedure using frequent measurements of a calibration gas.

The procedure is as follows. Every 2 min, we actuate the solenoid valve to sample tank air for 10 s. We determined the calibration frequency of 2 min through a sensitivity test using null test data. By adjusting the calibration frequency and measuring the precision, we found similar 1σ uncertainties at 1 min and 2 min frequencies, but an increase in uncertainty at 4 min and beyond, making 2 min good for reducing gas consumption while maintaining high precision. We allow 5 s of flush time, leaving 5 s of measurement time. We determined the flush time duration of 5 s by sampling tank air in a lab setting at the same flow-rate and cell pressure as in-flight operation and measuring equilibration time. We calculate the average measured mole fraction of N_2O, CO_2, and CO in these 5 s. Figure 3.5 demonstrates a typical in-flight calibration.

For each species we then interpolated in time using a Forsythe, Malcom, and Moler cubic spline between each measured calibration gas value and subtracted the known "true" value from this interpolation, giving us correction as a function of time. We then subtract this calibration curve from the raw data. Figure 3.6 shows both raw CO_2 data and the correction we derive using the frequent calibration method from one of our flights. As mentioned above, the gas was on for 10 s, along with 5 s of post-calibration time removed to account for equilibration back to ambient sampling, resulting in a loss of 15 s of atmospheric observations every 120 s for an 87.5% duty cycle. As mentioned in Sect. 3.2.3, the calibration cylinder mixing ratios are near atmospheric values. As seen in *Santoni et al.* (2014), N_2O can take a long time to equilibrate between measurement sources due to its propensity to stick to tubing. Thus, choosing calibration values close to ambient is critical for maintaining short flush times. This also holds for CO_2, though less so for CO. Artifacts that occur on

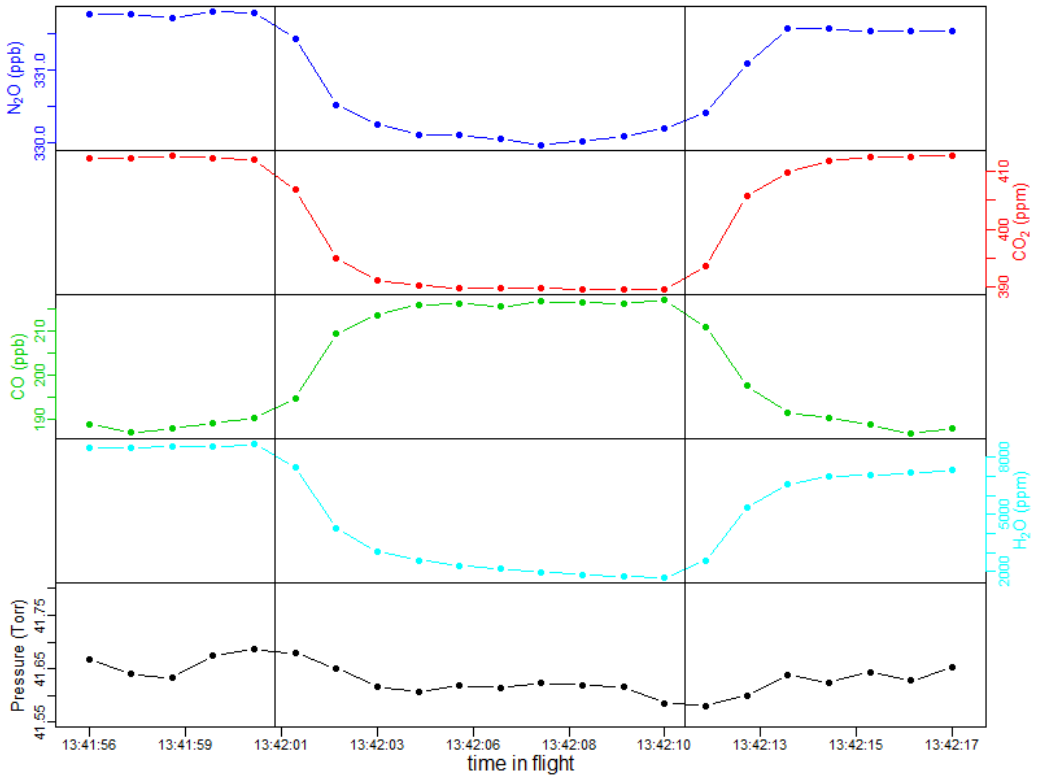

Figure 3.5: Example of in-flight calibration, showing time series of N_2O, CO_2, CO, H_2O, and cell pressure. Vertical lines indicate when the solenoid valve was actuated or closed. The first 5 seconds of each calibration are treated as equilibration time, and the last 5 seconds are used to find a mean calibration value.

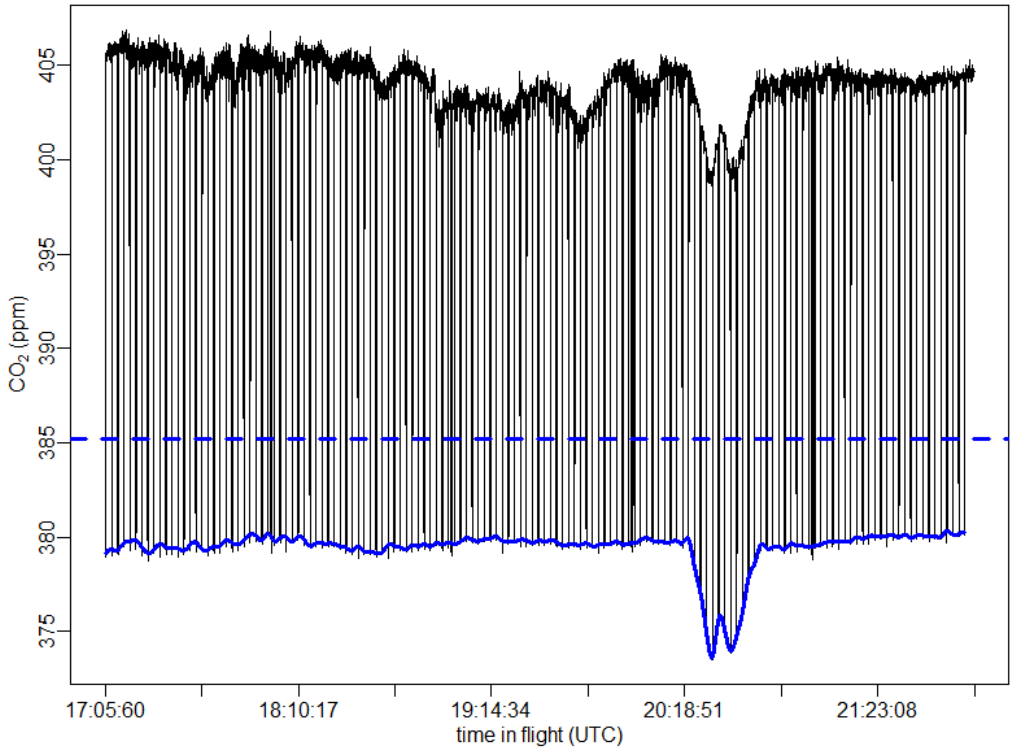

Figure 3.6: Raw CO_2 (black) measured by the FCHAOS for an entire flight, with frequent low dips due to calibrations. The blue dashed line indicates the "true" value of the calibration gas, the blue solid line shows the calibration curve obtained by interpolating between each calibration instance. The difference between the dashed and solid blue lines is used to correct for drift.

shorter time-frames, such as those induced by a short-duration turbulence event, will not be corrected with this method.

3.4 Calibration results and comparison with Picarro G2301-f

Figure 3.7 shows measurements from two null tests, one on April 26, 2017 in Colorado and one on May 2, 2017 in the Mississippi River Valley, the same null test as from Fig. 3.4. For each null test, the figure shows both the raw N_2O, CO, and CO_2 measurements and the corrected data following our calibration, along with the aircraft altitude. Our calibration method accounts for the clear cabin pressure/altitude dependence. During a null test FCHAOS samples tank air uninterrupted, rather

than making a calibration measurement every 2 min as in the frequent calibration procedure described in Sect. 3.3.2. Thus, we average 5 s of data from every 120 s to simulate the normal operation mode. Even after correction there is some residual coherent variability evident at the 15 min mark of the null test shown in the bottom 2 rows of Fig. 3.7, but this potential feature remains still within our 1 Hz precision.

Given the repeatable, smooth nature of the cabin pressure artifact, it would seem possible to use just the cabin pressure data to empirically correct for the artifact, without running frequent calibrations. This method would not account for long-term spectral drift however or traceability, and relies on the assumption that the cabin pressure artifact will be stable and repeatable. These weaknesses compromise such an approach.

Figure 3.8 compares the raw CO_2 data from the Picarro G2301-f and FCHAOS during a research flight along with altitude, and a second comparison once the FCHAOS data is corrected. The difference between the two instruments is shown in the top 2 panels. The most significant discrepancies occur during the vertical profile section of the flight. Following calibration, the deviation during profiling is eliminated, and the 1σ uncertainty in the difference is reduced from 1.15 ppm to 0.28 ppm.

For the FEAST campaign, in post-processing it became evident that a persistent offset of 0.51 ppm existed for CO_2 between the Picarro and FCHAOS. For the CO_2 comparisons in this manuscript, we have corrected for this bias. We believe the origin of this offset to be related to regulator contamination of a calibration gas cylinder and/or tubing used in conjunction with the regulator. With subsequent investigation it has been difficult to identify the exact cause. We do note that in comparing the Picarro and FCHAOS instruments, they both are calibrated with dry tank air, whereas the in-flight comparison is while measuring wet ambient air. Any residual water vapor sensitivity not corrected for either analyzer can manifest as an apparent

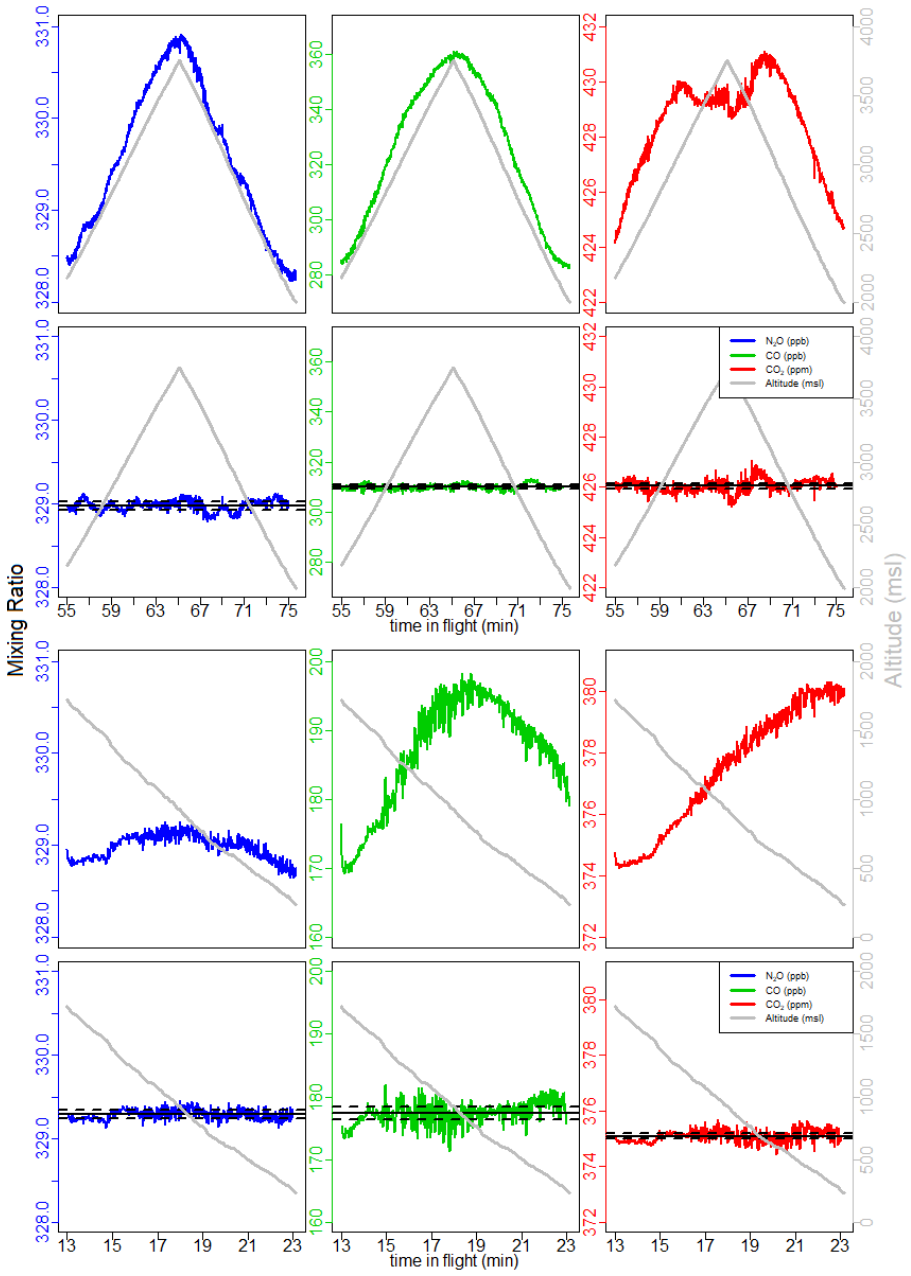

Figure 3.7: Top two rows show FCHAOS data from a null test on April 26, 2017, bottom two rows shows data from a null test on May 2, 2017, the same seen in Fig. 3.4. Rows 1 and 3 show N_2O, CO, and CO_2 during the null test before any calibration, rows 2 and 4 show the gas data following the frequent calibration correction. The procedure removes cabin pressure dependence and calibrates for linear drift. Black horizontal lines show mean and 1σ uncertainty.

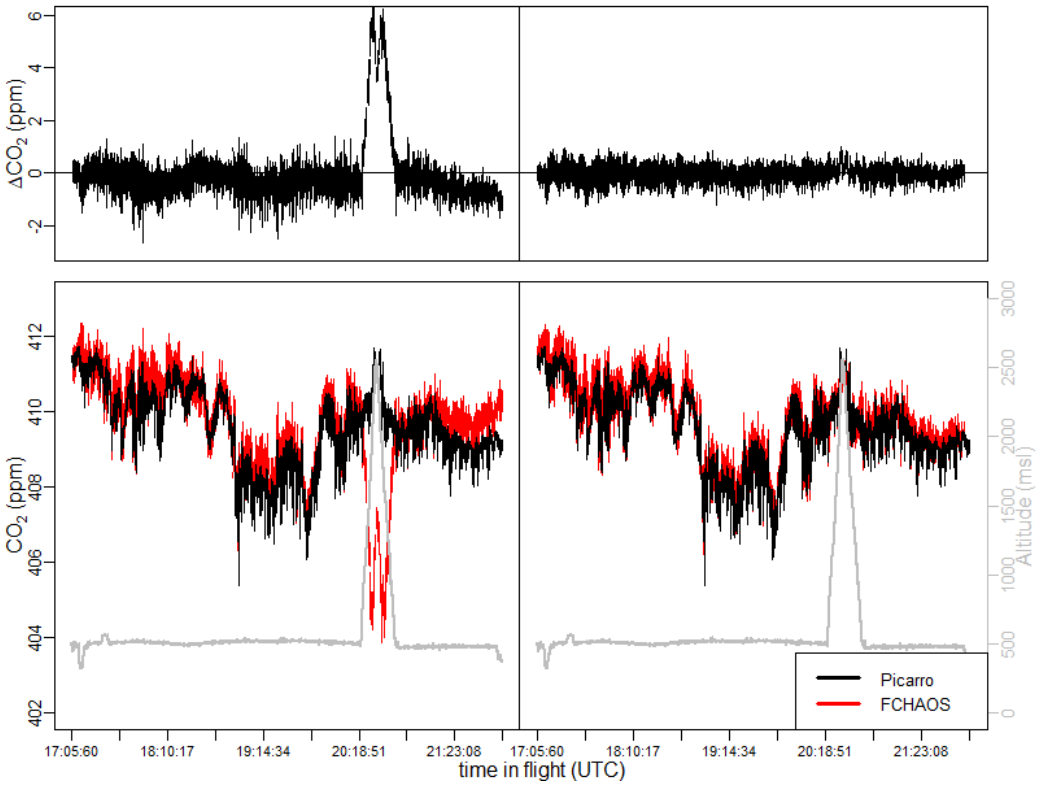

Figure 3.8: Bottom panels show Picarro G2301-f and uncalibrated FCHAOS CO_2 time series on left, Picarro G2301-f and calibrated FCHAOS CO_2 on right. Top panels show difference between the two instruments with and without FCHAOS calibration. The calibration procedure corrects for any artifacts in the FCHAOS data correlated with aircraft altitude.

bias, and this further emphasizes the need to validate water vapor corrections, as pointed out by *Pitt et al.* (2016), and further outlined for FCHAOS above in the discussion of the water vapor correction.

The raw H_2O measurements exhibit good agreement between FCHAOS and the Picarro G2301-f. The H_2O data was not calibrated or adjusted in any way, as there appeared to be small impact from cabin pressure variance and it is not well characterized. Figure 3.9 shows a histogram of the differences in FCHAOS and Picarro G2301-f H_2O and CO_2 (following calibration) for ∼40 hours of research flight time. Figure 3.10 shows the differences as a function of time for all flight data. For H_2O, we find a mean difference between the two instruments of 180 ppm, a median of 180 ppm, and 1σ of 340 ppm, shown in the figures as solid and dashed lines. In-flight 1σ precision for H_2O from the Picarro G2301-f has been reported as 100 ppm (*Crosson*, 2008), while the in-flight 1σ precision for the FCHAOS was found to be 10 ppm.

Why does water vapor not exhibit the same sensitivities as the other gases? To assess the sensitivity for water vapor to cabin pressure is more challenging given the long equilibration time. In Fig. 3.11 we show H_2O during the null test. On the null test where water vapor has previously equilibrated, some altitude-dependent sensitivity is apparent (∼60 ppm). Our calibration approach cannot well address this potential residual sensitivity given the long equilibration time required for H_2O. Does this potential artifact matter? In comparison with the Picarro analyzer (Fig. 3.11) we see no evident residual sensitivity to altitude. Given relative uncertainties, we cannot eliminate the presence of a vertical sensitivity of 10s ppm for water vapor.

3.4.1 Precision and Accuracy

To assess the FCHAOS precision, we consider flight data during a null test when the altitude did not significantly change. We find 1 s precisions of ±0.05 ppb, ±0.10 ppm, ±1.00 ppb, and ±10 ppm for N_2O, CO_2, CO, and H_2O respectively. This is

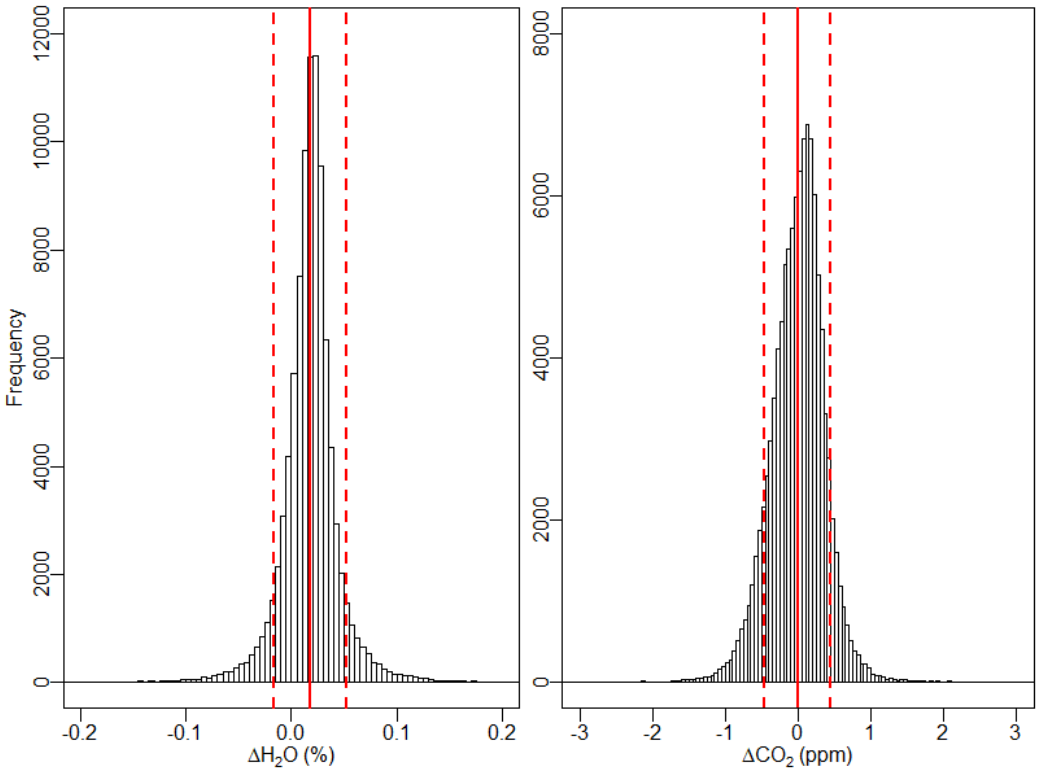

Figure 3.9: Histogram of difference between H_2O and CO_2 mixing ratios from FCHAOS and the Picarro G2301-f. FCHAOS CO_2 has been calibrated, while H_2O has not. For H_2O, mean of 0.018% or 180 ppm, median of 0.018% or 180 ppm, 1σ of 0.034% or 340 ppm, where Picarro G2301-f precision is 100 ppm. For CO_2, mean of 0 ppm, median of 0.024 ppm, 1σ of 0.45 ppm.

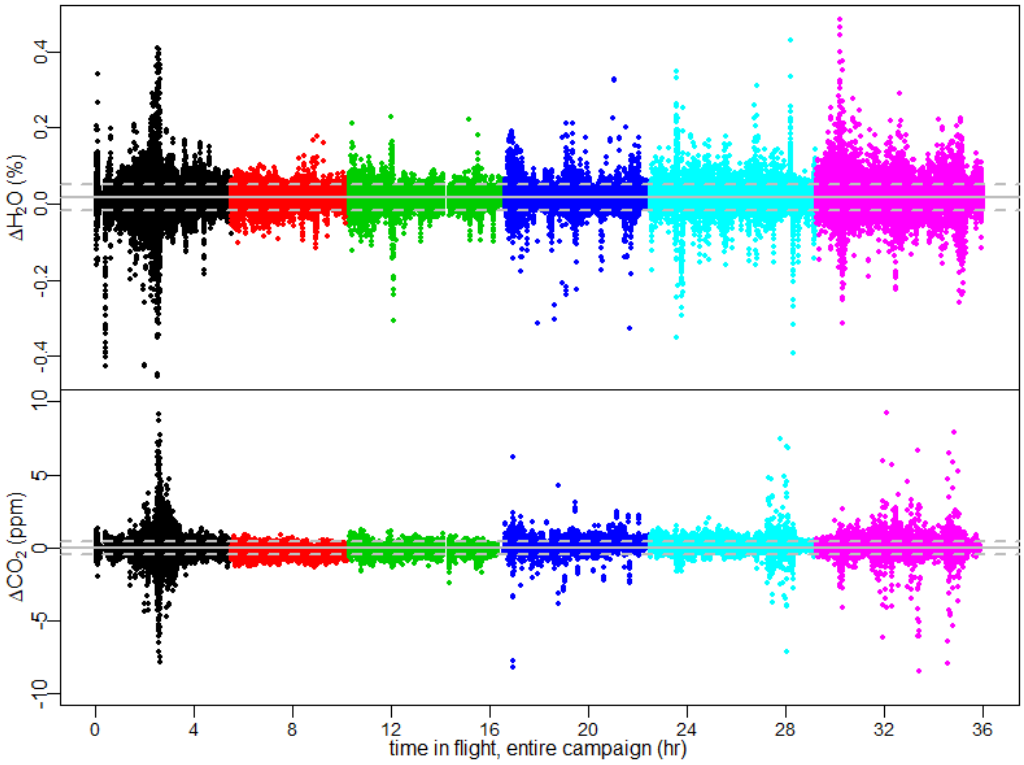

Figure 3.10: Difference as function of flight time for FCHAOS and Picarro G2301-f H_2O and CO_2 for all research flights. Colors separate flight days, gray lines indicate mean and 1σ uncertainty. Largest deviations occur when sampling in the immediate near-field of large point sources where some mismatched lag times contribute to deviations.

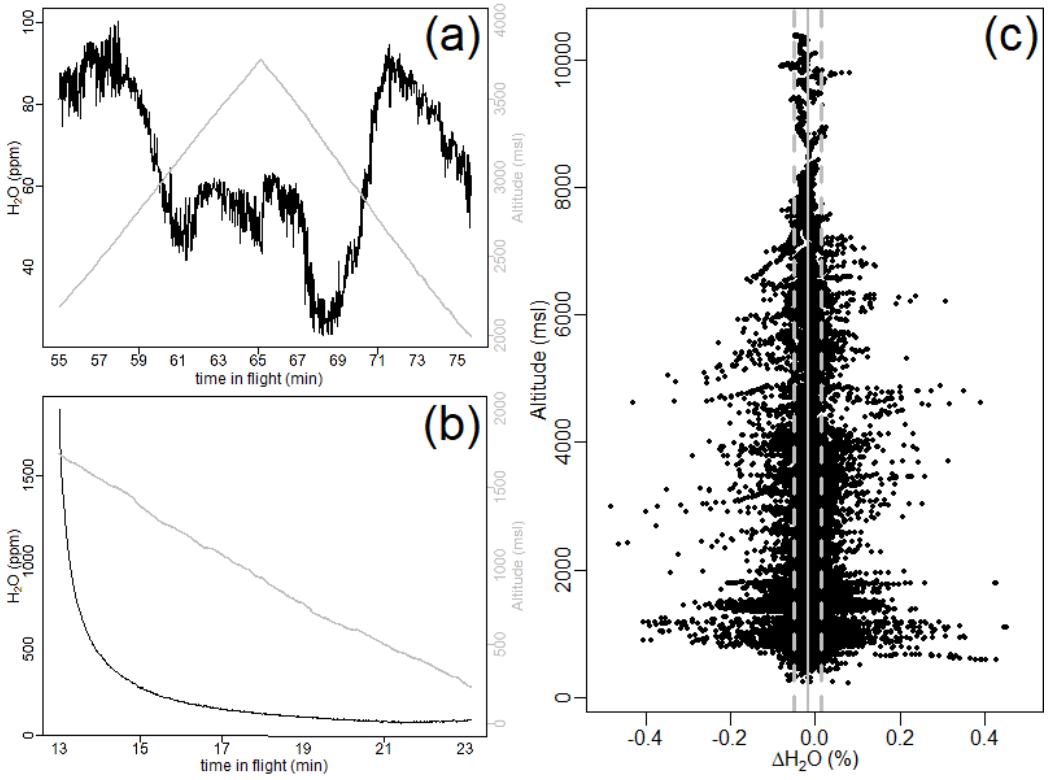

Figure 3.11: Panels (a) and (b) show H_2O during null tests from Fig. 3.7. In panel (b) H_2O hasn't fully equilibrated. In panel (a), H_2O previously equilibrated and there does appear to be a dependence on altitude on the order of 60 ppm. As seen in panel (c), the difference in H_2O between the Picarro and FCHAOS over the entire campaign does not exhibit an altitude dependence, so while there may be some altitude sensitivity, the effect is relatively small compared to typical atmospheric concentrations of H_2O and our overall water vapor uncertainty.

about a factor of 2 greater than the performance on the ground in a lab setting, with 1σ precisions of 0.02 ppb, 0.05 ppm, 0.50 ppb, and 7 ppm. Considering an Allan variance analysis of both the in-flight null test and in-lab study, the same result holds, in that the Allan variance in the air closely matches the ground, with performance degraded by a factor of 2.

In addition to the frequent calibrations every two minutes, a second cylinder is sampled every hour for 25 s as a "check gas" to test the traceability of the in-flight system. The last 5 s of each check gas period is used to calculate a mean value for each species. Figure 3.12 shows each instance of N_2O, CO_2, and CO check gas sampling, along with histograms for the difference from the known value. The time series show the last 5 s of each check gas period, along with a horizontal line indicating the known value of the air tank calibrated with the WMO standards as in Sect. 3.2.3. Note that the "check gas" and "calibration gas" cylinders were switched halfway through the campaign due to gas consumption, as reflected by the horizontal line. Looking at the difference of each check gas period from the known value, we find median offsets of 0.06 ppb, 0.06 ppm, and 0.03 ppb for N_2O, CO_2, and CO respectively, representative of possible bias between the flight system and the WMO scale. The 1σ values for the check gas points are 0.1 ppb, 0.3 ppm, and 1.62 ppb for N_2O, CO_2, and CO, representative of traceability of individual 1 s observations to the WMO scale. Table 3.1 summarizes the precision and accuracy for the four gases, though we were unable to measure H_2O traceability because we calibrated with dry tank air. We do report water vapor (and carbon dioxide) performance in comparison with the Picarro. Total instrument 1 s uncertainty is derived from summing in quadrature the 1σ accuracy to WMO, water vapor correction, and standard tank calibration uncertainty.

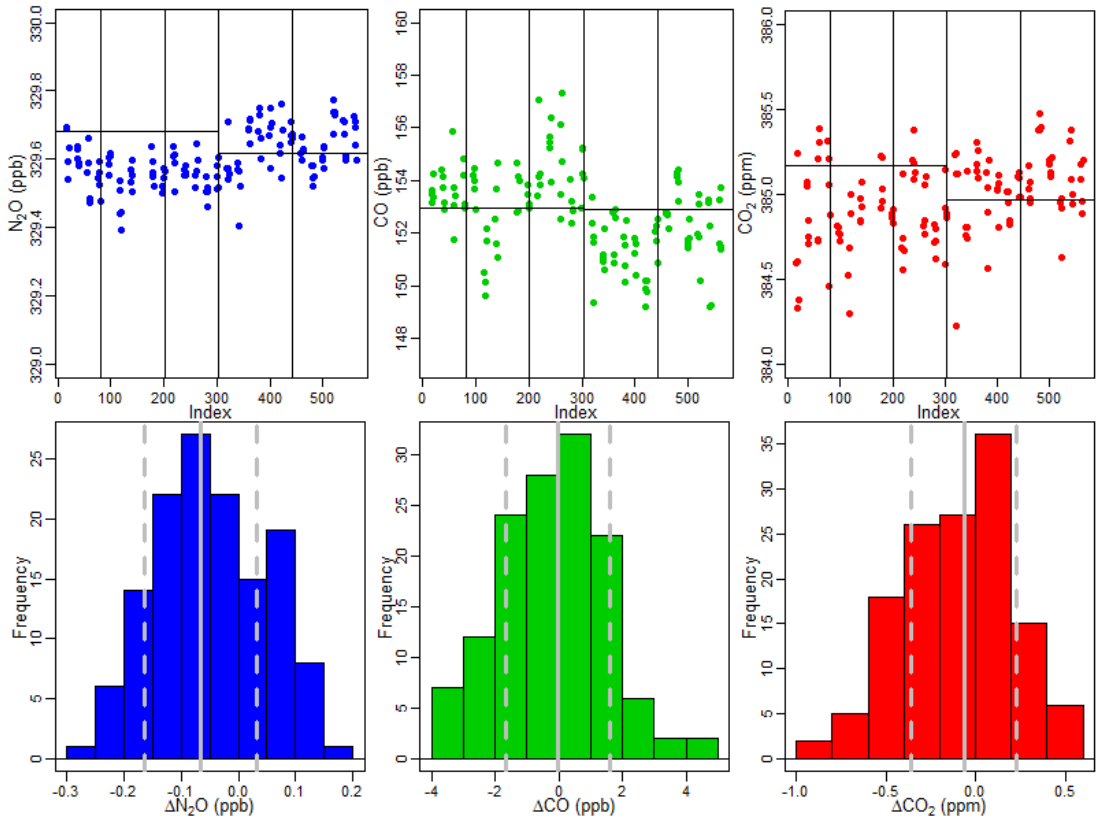

Figure 3.12: Top row: the last 5 s of each check gas period, black horizontal line indicating the value of the sampled gas traced to the WMO scale. Vertical lines separate the individual research flights. Bottom row: histograms of difference between known check gas value and last 5 s of measured check gas value, with solid gray lines indicating median and dashed lines showing 1σ uncertainty.

Table 3.1: Precision and accuracy for N_2O, CO_2, CO, and H_2O.

	N_2O (ppb)	CO_2 (ppm)	CO (ppb)	H_2O (ppm)
1σ Precision	0.05	0.1	1	10
Accuracy (median offset)	0.06	0.06	0.03	NA
1σ comparison with Picarro	NA	0.45	NA	340
Accuracy (1σ check gas)	0.1	0.3	1.62	NA
Water vapor correction	0.023	0.076	0.75	NA
WMO standard calibration	0.26	0.11	0.71	NA
Total 1σ uncertainty	0.28	0.33	1.92	NA

3.5 Applications

Continuous airborne N_2O observations can be useful for quantifying fluxes and estimating emissions on a facility-to-regional scale. Mass balances techniques, which have been utilized to estimate emissions of other atmospheric gases as in *Karion et al.* (2013), *Smith et al.* (2015), *Peischl et al.* (2015a), and *Kort et al.* (2016), could similarly be applied for N_2O. Figure 3.13 shows the path flown during a research flight on May 6, 2017, with measured N_2O mole fraction in color, white arrows indicating wind direction and speed, and blue and black arrows showing the direction of the flight route and the upwind and downwind transects. The downwind transect was flown at a mean altitude of 1515 msl, 1σ of 14 m, and the upwind transect at a mean altitude of 1501 msl, 1σ of 14m. The bottom right panel of the figure shows N_2O from this flight as a function of latitude with the upwind and downwind transects in blue and black, while the top right panel shows the difference in N_2O between the downwind and upwind at each latitude. There is a distinct enhancement in the downwind transect relative to the upwind transect in the lower latitudes, from about 31.5° N to 32° N. This enhancement disappears at higher latitudes and the N_2O measurement tracks well between upwind and downwind transects, even with a substantial latitudinal gradient. This flight illustrates the ability of this instrument to accurately measure small variations and link to local emissions (to the south) or larger scale gradients (to

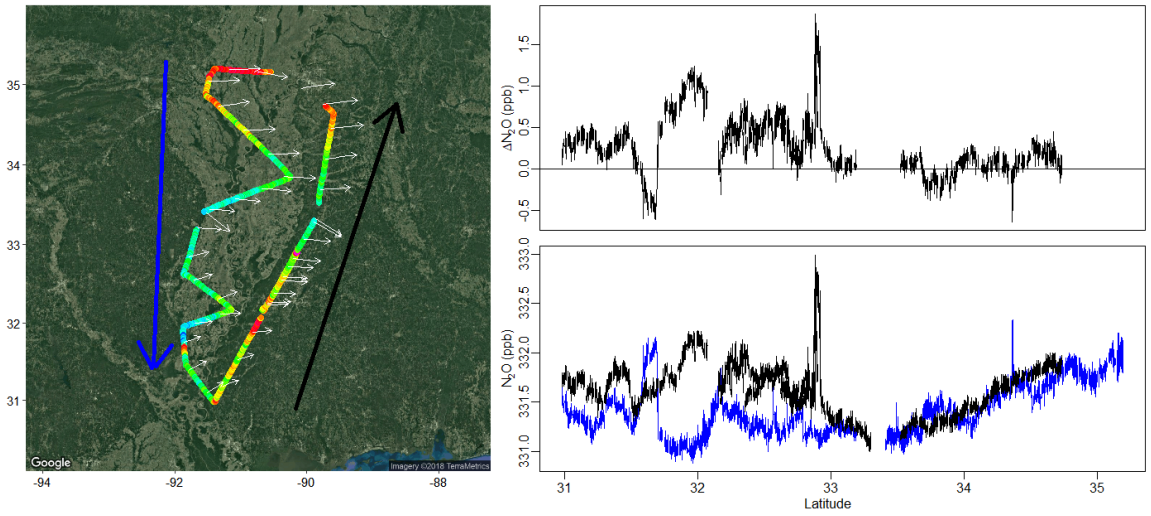

Figure 3.13: Left panel: flight path with N_2O signal and wind direction (white arrows). Blue and black arrows show the direction of the planes route and indicate upwind and downwind transects. Bottom right panel: N_2O signal as a function of latitude with upwind and downwind transects colored by blue and black, respectively. Top right panel: Difference in N_2O between downwind and upwind transects as a function of latitude.

the north). Future analyses of this data can involve mass balance flux quantification and/or regional model comparisons, both to quantify emissions and link to driving factors such as soil moisture or crop type.

As a fast-response sensor, FCHAOS can also be used for point source quantifications, as first explained in *Conley et al.* (2017) and further analyzed in *Mehrotra et al.* (2017); *Vaughn et al.* (2017). During FEAST, we circled several fertilizer plants with significant N_2O emissions, and future analyses can leverage these observations to better quantify emissions from the large point sources.

3.6 Conclusions

We present a continuous-wave, mid-IR laser spectrometer system that can measure continuous 1 Hz airborne mole fractions of N_2O, CO_2, CO, and H_2O. The commercial analyzer, when operated off-the-shelf, exhibits a dependence of N_2O, CO_2, and CO

on cabin pressure. We correct for this artifact by employing an updated calibration procedure with mass flow control at a high flow rate enabling high-frequency, short-duration calibrations. While modern systems conventionally use pressure control and infrequent, long-duration zeros, our method expands on these previous approaches and opens up uses for the instrument in ways that have not yet been realized. We solve the inability of other systems to operate with large changes in cabin pressure by mitigating the cabin pressure effect while maintaining a ∼90% duty cycle. In-flight 1σ precisions are estimated to be ±0.05 ppb, ±0.1 ppm, ±1 ppb, and ±10 ppm for N_2O, CO_2, CO, and H_2O, with total uncertainty in traceability estimated at 0.28 ppb, 0.33 ppm, and 1.92 ppb for N_2O, CO_2, and CO. We then validate our method by comparing FCHAOS data to CO_2 and H_2O measurements from a flight-proven cavity ring-down spectrometer, seeing excellent agreement. This flight-proven system can provide key insights into N_2O emissions processes by providing observational support for facility-quantification, for mass-balance flux estimates, and for inverse modeling. As presented, this system can be utilized for precise, accurate, continuous 1 Hz airborne observations of N_2O, CO_2, CO, and H_2O.

CHAPTER IV

Fertilizers: Greenhouse gas emissions from fertilizer production and agriculture

Chapter in preparation for submission to *Global Biogeochemical Cycles*. It was coauthored with Eric A. Kort, Mackenzie L. Smith, and Stephen Conley.

Abstract

Agricultural activity is a significant source of greenhouse gas emissions. The fertilizer production process emits N_2O, CO_2, and CH_4, and croplands with applied fertilizer emit N_2O. We present continuous airborne observations of these three trace gases in the Lower Mississippi River Basin to quantify emissions from both fertilizer plants and croplands during the growing season. Observed hourly emission rates from two fertilizer plants are compared with reported inventory values, showing good agreement in N_2O and CO_2 emissions but large underestimation in CH_4 by up to a factor of 100. These CH_4 emissions would be consistent with loss rates of 0.6–1.2%. We quantify regional emissions fluxes of N_2O using the airborne mass balance technique, a first application for N_2O. The effect of crop type, fertilizer application, soil moisture, and soil temperature on emissions is investigated. We find soil moisture and total area planted of soybean, cotton, and rice to be the strongest predictors of N_2O fluxes. We report average regional fluxes of 1.8 ± 1.4 g N_2O-N ha^{-1} hr^{-1}.

4.1 Introduction

Nitrous oxide (N_2O) is the third most important long-lived anthropogenic greenhouse gas (*Myhre et al.*, 2013). It is also currently the most significant anthropogenic source of stratospheric ozone depletion (*Ravishankara et al.*, 2009). An estimated 16 Tg N_2O-N yr^{-1} was emitted globally in the 1990s, with about half coming from anthropogenic sources including agricultural land management, sewage, and biomass burning (*Reay et al.*, 2012). The estimated magnitude of agricultural emissions ranges from 4–7 Tg N yr^{-1} and is predicted to rise in the next decade as developing nations improve their agricultural productivity (*FAO*, 2017). The large uncertainty in emissions estimates is a result of infrequent measurements with limited geographical coverage for emissions that exhibit high spatial and temporal variability (*Monni et al.*, 2007) combined with a lack of direct measurements to get accurate emission factors from all sources (*Brown et al.*, 2001).

A dominant source of anthropogenic N_2O has been the mass application of fertilizer. Since 1908 the Haber-Bosch process of synthesizing ammonia and producing nitric acid, ammonium nitrate, and other compounds has allowed for mass production of synthetic fertilizer, with current global production levels near 100 Tg N yr^{-1} (*Erisman et al.*, 2008; *Smil*, 2011). Between 1961–2013 global N fertilizer consumption increased by a factor of nearly 10, with 5 countries accounting for over 60% of the consumption (*Lu and Tian*, 2017). In the United States the current fertilizer application rate is 11.4 Tg N yr^{-1}, a $\sim$40 times increase since 1940 (*Cao et al.*, 2018). Fertilizers provide essential nutrients to plants that enhance their growth and yield but soils have a limit nutrient uptake capacity, and so over-application of nitrogen fertilizer can cause a nonlinear increase in N_2O emissions (*Grant et al.*, 2006).

Fertilizer production itself also emits greenhouse gases and differences in production type and efficiency affect the total footprint of synthetic fertilizer (*Fossum*, 2014). Ammonia production is energy-intensive, requiring the combustion of natu-

ral gas or other fuels to synthesize nitrogen and hydrogen (*Gellings and Parmenter*, 2016). Plants may then oxidize ammonia to produce nitric acid, which is used to manufacture ammonium nitrate fertilizer (*EFMA*, 2000). Ammonia oxidation emits waste gases, including N_2O (*EFMA*, 2000). In 2017 23 million metric tons (MMT) of CO_2 equivalent (CO_2e) greenhouse gas emissions were emitted by fertilizer plants accounting for 73% of total US nitrogen production capacity (*TFI*, 2017). N_2O and CH_4 emissions are converted to CO_2e values by multiplying by global warming potential values of 298 and 25, respectively. Though facilities report their emissions, independent objective observations of production sources have been limited.

While fertilizer is arguably the strongest driver of N_2O soil emissions, various factors including climate, soil conditions, and management practices can impact N_2O emissions. Increased N_2O emissions can positively correlate with higher soil temperature and moisture, particularly after precipitation (*Dobbie et al.*, 1999; *Griffis et al.*, 2017). The positive relationship between N_2O emissions and soil moisture has been observed in various environments and soil conditions (*Smith et al.*, 1998, 2003; *Marinho et al.*, 2004; *Schindlbacher et al.*, 2004; *Pattey et al.*, 2008). Crop species and type of residue crop cover can also affect emissions (*Parkin and Kaspar*, 2006; *Lemke et al.*, 2018).

Flux chambers are a commonly-used method to quantify N_2O emissions. They are relatively inexpensive and easy to deploy, but they measure small areas, can perturb the area of study, and are constrained by manpower (*Rapson and Dacres*, 2014). Scaling up singular chamber measurements for greater representation of emissions is hampered by soil diversity and spatial variability (*Parkin et al.*, 2012; *Scaroni et al.*, 2014), necessitating data at larger regional spatial resolution. Studies at larger scales can also capture indirect emissions from nitrogen runoff and leaching. Process-based models have good coverage (*Del Grosso et al.*, 2006; *Tian et al.*, 2012) but also demand high computational power and often have large input uncertainties, relying

on constraints from observational data to reduce uncertainty (*Butterbach-Bahl et al.*, 2013; *Ehrhardt et al.*, 2017).

Many studies have investigated N_2O emissions in the Corn Belt region of the Upper Mississippi River Basin (*Parkin and Kaspar*, 2006; *Chen et al.*, 2016; *Nevison et al.*, 2018). Relatively less attention has been paid to the Lower Mississippi River Basin (LMRB) downstream in the southeast US. The region was added to the USDA's Long-Term Agroecosystem Research (LTAR) network in 2014 (*USDA ARS*, 2014). With ∼20 million acres—∼30% of total area—as cropland, much of it intensely developed and irrigated, it is a highly productive agricultural region responsible for a quarter of the US's corn production and two-thirds of its rice (*USDA ARS*, 2012; *Lund et al.*, 2013). A better quantification of emissions and improved understanding of the heterogeneous processes on fields including applied fertilizer and soil conditions can aid in mitigating atmospheric N_2O emissions.

Here we analyze continuous airborne observations of N_2O, CO_2, and CH_4 from research flights in the LMRB in May 2017 during the growing season (*Padgitt et al.*, 2000; *Snipes et al.*, 2004). The campaign took place immediately following a historic heavy rainfall/flooding event in the northern part of the region (*Heimann et al.*, 2018). We quantify emissions of N_2O, CO_2, and CH_4 from two large fertilizer plant point sources and compare to reported emissions from the Greenhouse Gas Reporting Program (GHGRP). We apply the airborne mass balance technique for the first time to quantify N_2O emission fluxes, and compare with gridded data sets of crop type, applied fertilizer, soil moisture, and soil temperature.

4.2 Methods

4.2.1 Flights

Research flights were conducted on a Mooney M20R single-engine aircraft (Scientific Aviation, Inc.) as part of the Fertilizer Emissions Airborne STudy (FEAST). There were six research flights from May 2–10, 2017, based out of West Memphis, Arkansas. Each flight typically lasted ∼6 hours from 12:00–18:00 local time (17:00–23:00 UTC), allowing a well-mixed boundary layer to develop. Combined, the flights covered most of the LMRB region, from 31° to 38°N and 88° to 93°W. The plane flew at an average altitude of 550 meters above ground level (magl), with multiple cross-wind transects designed to capture emissions plumes from agricultural activity in the river valley. During each flight at least one vertical profile was completed, circling the plane up past the mixing layer and back down while tracking atmospheric conditions and trace gases to determine the mixed layer depth. On the last two flights, two high-production fertilizer plants were circled to quantify point source emissions. Figure 4.1 shows the region of study with flight paths, along with land use for four major crops: soybean, corn, cotton, and rice.

4.2.2 Instrumentation

An Aerodyne laser absorption spectrometer measured N_2O, CO_2, CO, and H_2O mole fractions at 1 Hz frequency with an in-flight high-frequency flow-controlled calibration method as described in *Gvakharia et al.* (2018). In-flight 1 s precisions were ±0.05 ppb, ±0.10 ppm, ±1.00 ppb, and ±10 ppm respectively for N_2O, CO_2, CO, and H_2O. Water vapor corrections were applied to the data in post-processing to eliminate the effect of dilution and water line broadening—all measurements reported herein are dry molar fractions.

Additional payload on the aircraft, listed in *Conley et al.* (2014, 2017), included

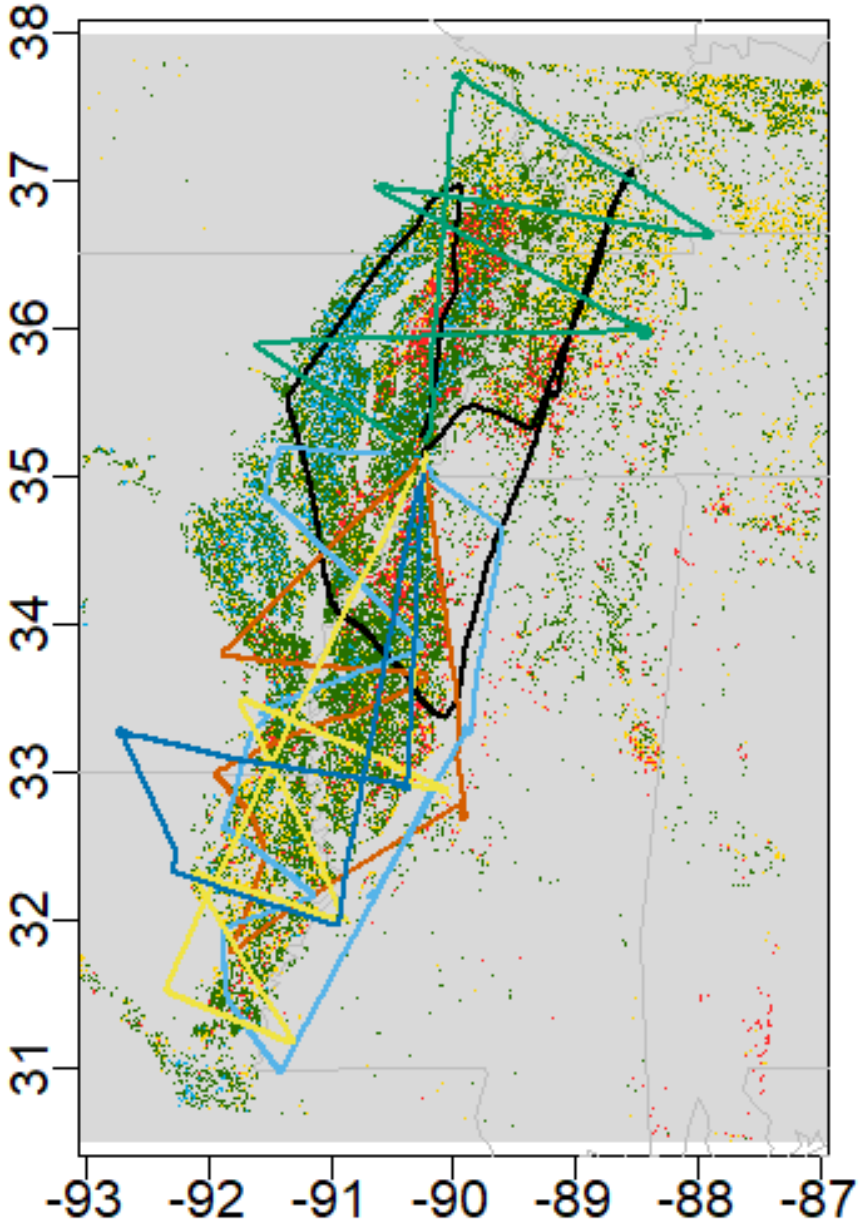

Figure 4.1: Map of the LMRB. FEAST research flights paths are traced with colors for individual flights. Green, yellow, red, and blue pixels respectively indicate cropland for soybean, corn, cotton, and rice at 30 m by 30 m resolution (*USDA*, 2017).

a Picarro G2301-f cavity ringdown spectrometer to measure CH_4, CO_2, and H_2O, a Vaisala HMP60 probe to measure temperature and relative humidity, and a 2B Technologies 202 ozone monitor. The Picarro measurements were sampled at 0.5 Hz and interpolated to acquire 1 Hz data. The Picarro was calibrated on the ground by sequentially sampling two gravimetrically-prepared NOAA WMO standards (*Dlugokencky et al.*, 2005). Wind speed and direction were calculated using a differential GPS system as described in *Conley et al.* (2014). Ambient air was sampled from an inlet installed underneath the aircraft wing, and traveled through ∼5 m of tubing to the instruments. Lag time between when air enters the inlet line and when it is sampled by the instruments was determined by breathing near the inlet and observing spikes in CO_2 and H_2O, resulting in lag times of 3 and 5 s for the Aerodyne and Picarro instruments respectively. These lag times were confirmed in flight by comparing peaks in CO_2 and H_2O from both instruments. The lag times are used in post-processing to align all instruments and sensors on a unified time basis.

4.2.3 Gridded Data

Crop land cover for 2017 is provided by the Cropland Data Layer (CDL) (*USDA*, 2017). The CDL uses satellite imagery to provide information on land use at 30 m by 30 m resolution for the United States. Data is transformed from USA Contiguous Albers Equal Area to a WGS84 projection, but land use values are not significantly changed by the re-projection.

A 5 km by 5 km gridded dataset of annual applied nitrogen fertilizer provides nitrogen input information (*Cao et al.*, 2017). The data used is from 2015, the most recent year available in the dataset. As of writing, gridded U.S. fertilizer application data with high spatial resolution for 2017 had not been identified.

Two soil moisture data sets are used in this analysis. The first is the SMAP Enhanced L3 Radiometer Global Daily 9 km EASE-Grid Soil Moisture, Version 2

data product from the Soil Moisture Active Passive (SMAP) satellite (*O'Neill et al.*, 2018). The satellite retrieves a surface volumetric water content value from soil thermal emissions measured with a radiometer. The product has a spatial resolution of 9 km by 9 km following interpolation of brightness temperature from the radiometer at 36 km by 36 km resolution. Data is reported at 06:00 and 18:00 local time. This analysis uses the 06:00 data set, as research flights landed around 18:00 local time and made most of the observations before that time. While the satellite provides good spatial resolution, the area it scans on each pass of the earth does not always coincide with the flight path. In order to estimate regional soil moisture during a flight, the SMAP products from May 1–10, 2017 are averaged over the LMRB region. The second soil moisture data set is the North American Regional Reanalysis (NARR) product which combines model output and assimilated precipitation data (*Mesinger et al.*, 2006). The dataset is spatially gridded at approximately 0.3 degree by 0.3 degree resolution and values are reported at 3-hour intervals for several layers of soil. Values at 19:00 UTC time are used, coinciding with the middle of FEAST flights, and at the 0 cm surface level. To complement volumetric water content, water-filled pore space (WFPS) is also calculated to better relate soil properties. WFPS is defined by *Linn and Doran* (1984) in Equation 4.1

$$WFPS = \frac{\Theta_v}{1 - \frac{P_B}{P_P}} \tag{4.1}$$

where Θ_v is volumetric water content, P_P is soil particle density, and P_B is soil bulk density. A common P_P value of 2.65 g cm^{-3} is used (*Soane*, 1990). For P_B, an average value of 1.385 g cm^{-3} is used based on measurements of soil density in the LMRB (*Römkens et al.*, 1986; *Selim et al.*, 1987; *Scott et al.*, 1998).

NARR is also used for soil temperature data (*Mesinger et al.*, 2006). Like the soil moisture product, the dataset is spatially gridded at 0.3 degree by 0.3 degree

resolution, with 3-hourly values of temperature for several layers of soil. The 19:00 UTC time and 0 cm surface level values are used in this analysis.

4.2.4 Point Source Quantification

Emission rates from point sources are quantified following the methodology first described in *Conley et al.* (2017) and used by *Mehrotra et al.* (2017); *Vaughn et al.* (2017). Figure 4.2 illustrates the technique. The plane circles a source at constant radius and discrete altitudes, starting near 200 magl and ascending until the plume is no longer detected, then descending back down. By measuring the atmospheric concentration upwind and downwind of the source simultaneously with the wind, an emission rate is calculated for a given trace gas.

Due to the frequent calibration of the FCHAOS system, 15 s of data was not sampled every 120 s. When quantifying N_2O and CO_2 emission rates, the FCHAOS data was interpolated to fill in gaps throughout the loops. As seen in Table 4.1, CO_2 estimates agree between the FCHAOS and the Picarro, supporting the interpolation and use of FCHAOS measurements in this analysis.

Table 4.1: CO_2 emission rates

Plant	FCHAOS CO_2 (mt hr^{-1})	Picarro CO_2 (mt hr^{-1})
Plant 1	98.3±24	94.6±21.4
Plant 1	94.4±17.6	109.1±24.7
Plant 2	73.6±15.7	88.1±19.3

4.2.5 Mass Balance Technique

Using the mass balance method (*White et al.*, 1976), atmospheric N_2O fluxes are quantified for regions in the LMRB. The usefulness of this approach has been well-documented in estimates of methane (*Karion et al.*, 2015; *Peischl et al.*, 2015a; *Smith et al.*, 2017a), ethane (*Smith et al.*, 2015; *Kort et al.*, 2016), and black carbon (*Schwarz et al.*, 2015) emissions from oil and natural gas activity. The flux during a

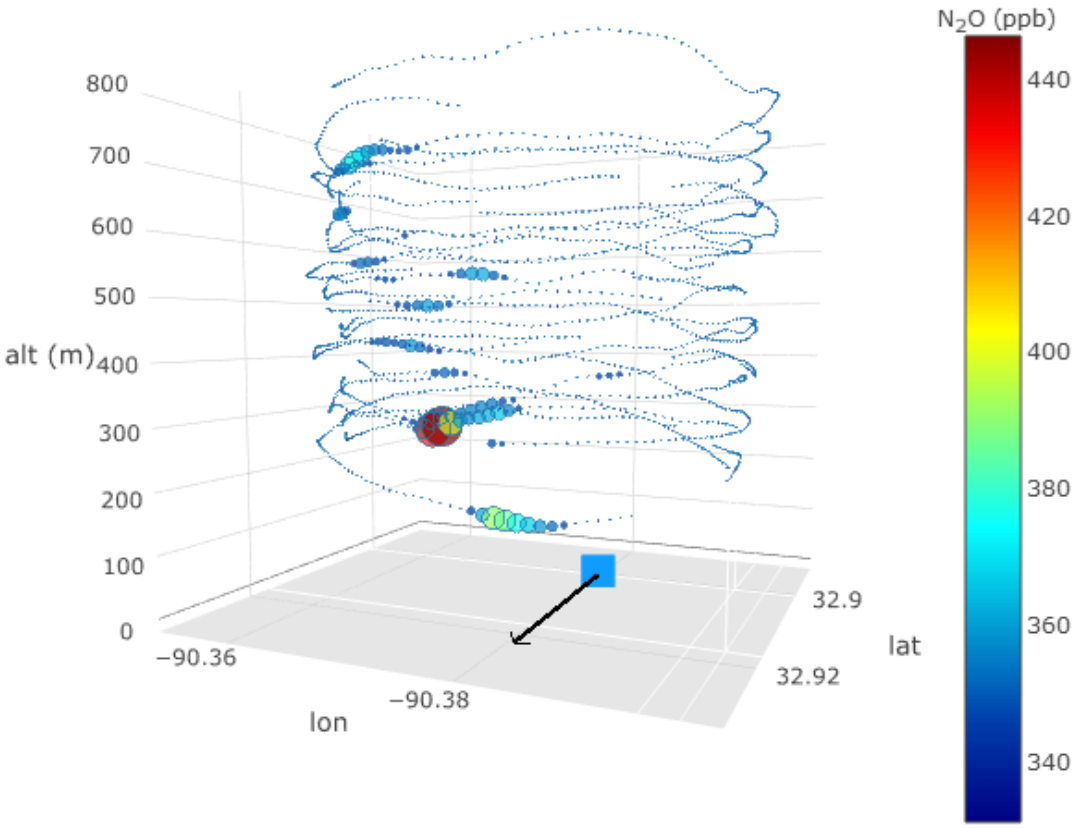

Figure 4.2: Flight pattern during point source quantification. The blue square shows the location of the emitting source, in this case a fertilizer plant, and the black arrow indicates wind direction. N_2O molar fraction is given both by the color bar and the point size. The plane circles the source upwind and downwind at several altitudes, capturing the emissions plume, and the data is then processed to quantify emissions fluxes.

flight transect is given by Equation 4.2

$$flux_{N_2O} = \nu\, cos\theta \int_{x_i}^{x_f} X_{N_2O}\, \mathrm{d}x \int_{z_g}^{z_1} n_{air}\, \mathrm{d}z. \tag{4.2}$$

where $\nu\, cos\theta$ is the horizontal wind component perpendicular to the airplane's heading, x_i and x_f define the width of the flight transect over ground, X_{N_2O} is the N_2O molar fraction enhancement over background during the transect, and z_g is the terrain height above sea level. z_1 is the adjusted mixed layer height as defined in *Peischl et al.* (2015a), $z_1 = (3z_{PBL} + z_e)/4$ where z_{PBL} is the planetary boundary layer depth and z_e is the entrainment height at which mixing below the boundary layer finally reaches free troposphere levels. n_{air} is the molar density of air. Background N_2O is determined by averaging 30 s of data at the start and end of a plume. Uncertainty for mixing layer height is defined as Δz=z_1-z_{PBL}, while for the other components it is defined by the 1σ value. All uncertainties are then propagated by summing in quadrature for the total flux uncertainty.

For each flight mass balance transects are identified and an N_2O flux is calculated using Equation 4.2. Emissions are then quantified from a subregion bounded by two transects by subtracting the flux of the upwind transect (or "flux in") from the flux of the downwind transect (or "flux out"). Transects are chosen such that a transect with length l_i and mean angle of wind normal to the aircraft θ_i has a similar $l_i\, cos\theta_i$ value as another transect with $l_j\, cos\theta_j$. The air mass passes through two planes with equal areas defined by $l\, cos\theta\, z_1$, allowing comparison of fluxes from different transects.

4.3 Results

4.3.1 Fertilizer Plant Emissions

Two large fertilizer plants with significant greenhouse gas emissions are investigated. These are 2 of 19 facilities in the US with reported N_2O emissions greater

than 100,000 mt CO_2e (*EPA*, 2017). Plant 1 was responsible for 5% of all US CO_2e emissions of N_2O in 2017, and Plant 2 contributed 1% (*EPA*, 2017). In terms of ammonia production, 32 plants in the US accounted for 10,500 thousand mt N (*USGS*, 2018). Plant 1's ammonia production capacity is equal to 4% of the total US ammonia production, while Plant 2's capacity is 3.5% (*Nutrien*, 2018). Figure 4.3 shows N_2O and CO_2 quantified emission rates from the FCHAOS system, CO_2 and CH_4 emission rates from the Picarro, and reported GHGRP emissions for both plants. The GHGRP emissions are scaled down from Tg yr^{-1} to kg hr^{-1}, as fertilizer production facilities typically run non-stop throughout the year with some periodic maintenance, resulting in low temporal variability (*TFI*, 2017). Plant 1 was observed on both May 9 and May 10, while Plant 2 was observed only on May 10. Estimates for N_2O and CO_2 agree well within uncertainty with emissions reported in the GHGRP. For Plant 1, there is consistency in emissions from one day to the next.

CH_4 estimates are several orders of magnitude larger than the reported values, by a factor of 100 for Plant 1 and 20 for Plant 2. According to the GHGRP, 100% of the CH_4 emissions from both plants is a result of stationary fuel combustion (*EPA*, 2017). Using the amount of gas combusted, a leakage rate is calculated to account for the discrepancy in observed and reported emissions. Plant 1 directly reports the amount of natural gas consumed while Plant 2 does not, but the value is calculated using reported emissions and GHGRP-defined emission factors. Using a typical natural gas composition range of 70–90% CH_4 (*Speight*, 2007) results in a range in leakage rates of 0.6–0.8% for Plant 1 and 0.9–1.2% for Plant 2. CH_4 accounts for $\sim$0.01% of total GHGRP-reported CO_2e emissions for both plants, with N_2O and CO_2 contributing essentially all of the GHG emissions. Adding in observed CH_4 emissions changes the contribution of methane to 0.9% for Plant 1, a factor of 90 increase, and 1.8% for Plant 2, a factor of 180 increase.

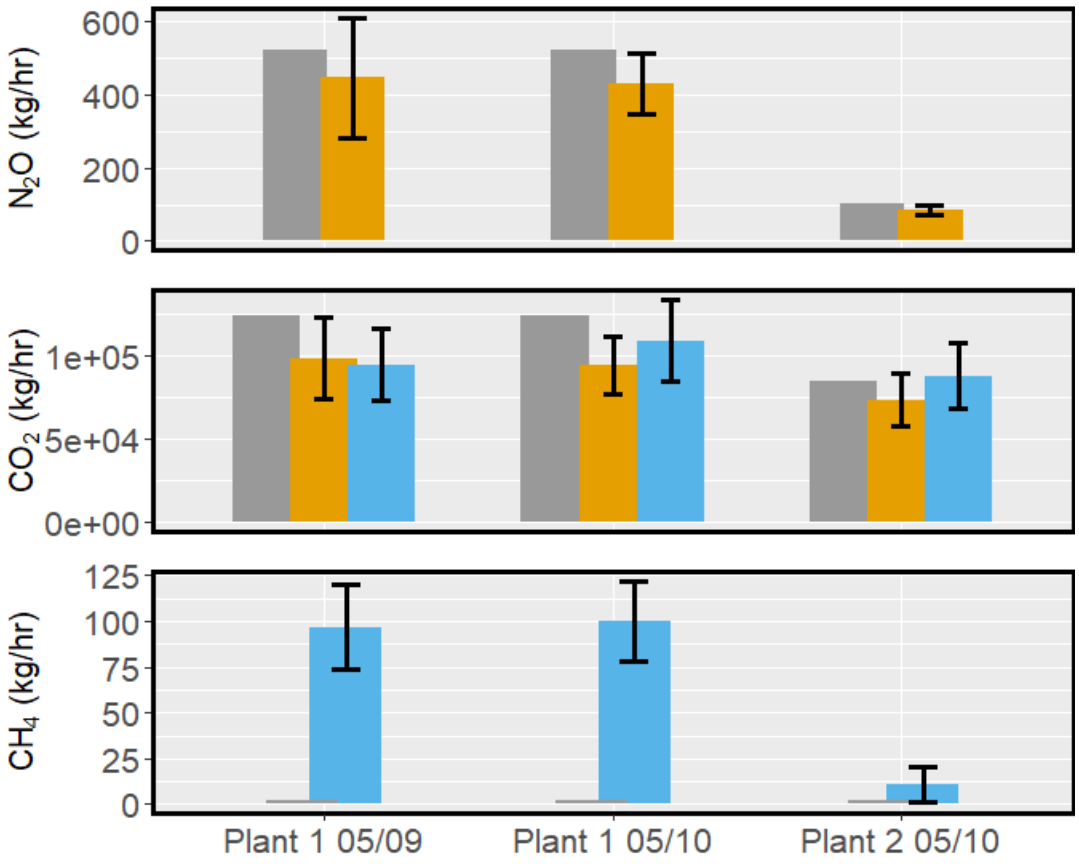

Figure 4.3: Observed emissions for N_2O, CO_2, and CH_4 (FHCAOS in orange, Picarro in blue) along with 2017 GHGRP data (gray) for two fertilizer plants from *EPA* (2017). Black error bars indicate 1σ uncertainty.

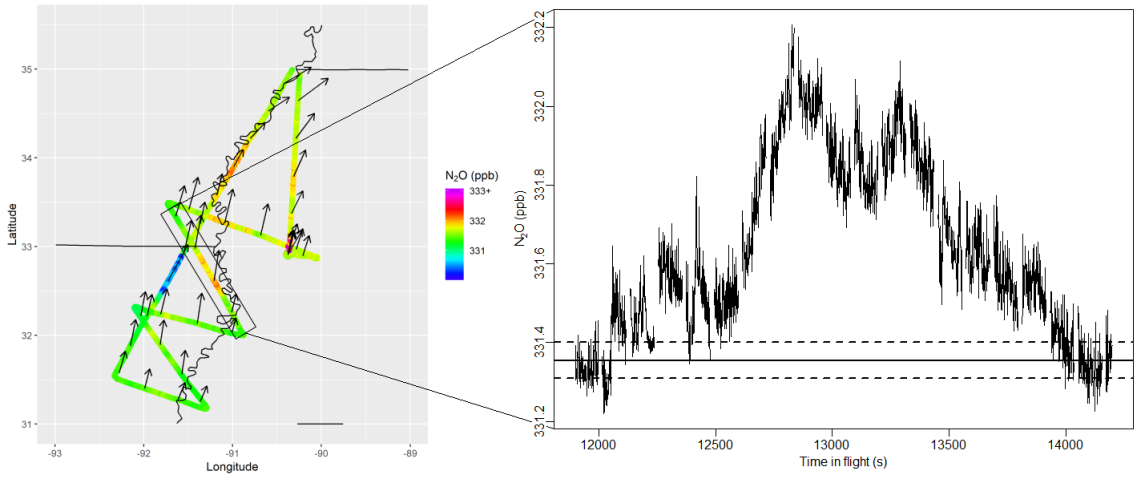

Figure 4.4: a) Flight path for May 9, 2017, colored by N_2O mole fraction. Black arrows indicate wind direction and relative magnitude. The black box highlights a transect used for mass balance. b) The N_2O mole fraction along the transect indicated by the black box in a). The first and last 30 s of the transect are used to find the mean background and its 1σ uncertainty (solid black line and dashed lines, respectively).

4.3.2 Regional N_2O Fluxes

N_2O fluxes are calculated from mass balance transects for 26 regions, ranging from the northern end of the LMRB near the Missouri/Kentucky border down to the southern end of the valley in northern Louisiana. Figure 4.4 illustrates an example flight path and N_2O plume from May 9. Five transects are quantified from this flight, from which six flux regions are identified. A plume's behavior may affect the choice of background. The typical approach is to use the edges of the plume, as shown in Figure 4.4. For some plumes the aircraft did not fully exit the area of enhancement in the valley, and so edge values for plumes are higher than those from earlier transects further upwind. In these situations, background values from upwind transects are used to account for passive enhancement captured in the downwind transect. Figure 4.5 shows all 26 flux regions, dividing the LMRB into north, middle, and south subregions.

For all regions, the mean emission flux is 1.8 ± 1.4 g N_2O-N ha^{-1} hr^{-1}. *Marinho*

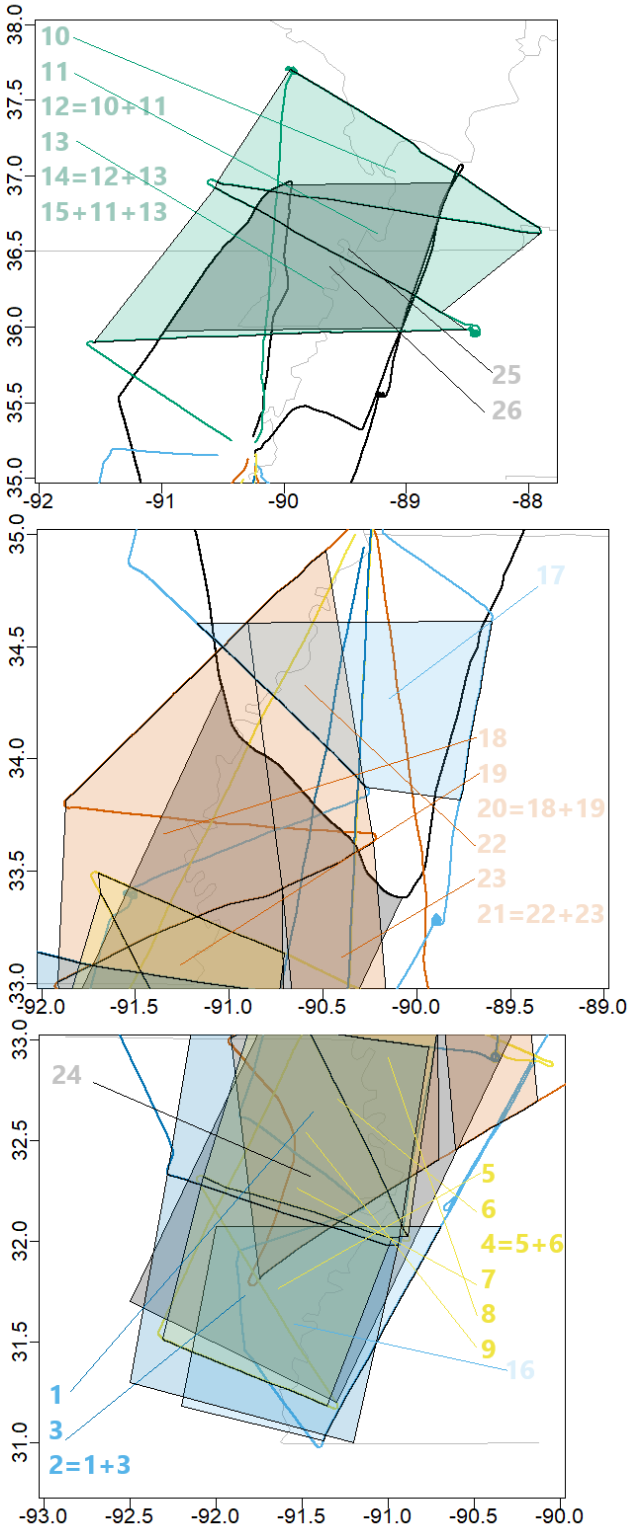

Figure 4.5: Flux regions used for N_2O emissions quantification. Polygons and numbers denote flux regions, colors denote distinct research flights from Figure 4.1.

et al. (2004) observed emissions from Mississippi Alluvial Plain soils of 1.5 g N_2O-N ha^{-1} hr^{-1} following rainfall in mid-June during the growing season, while *Scaroni et al.* (2014) reported emissions of 0.1 g N_2O-N ha^{-1} hr^{-1} from soils in the Louisiana river basin in June and July. From a flux chamber study in Iowa, *Parkin and Kaspar* (2006) reported soybean emissions of ∼2500 g N_2O-N ha^{-1} yr^{-1}, with typical hourly fluxes on the order of 1.5–2.4 g N_2O-N ha^{-1} hr^{-1} from soybean, consistent with the results of this analysis. *Parkin and Kaspar* (2006) report fertilizer application in Iowa occurring on day 155 of the year, while the FEAST campaign took place from day 122 to 130. However, crop planting in the LMRB typically occurs earlier than the Corn Belt according to the USDA's Crop Progress Reports (*USDA NASS*, 2017a). By May 7, 2017, based on fraction of state crop acreage for a particular crop, Arkansas, Kentucky, Louisiana, Mississippi, Missouri, and Tennessee had planted 50–76% of soybean, 50–77% of corn, 7–68% of cotton, and 67–92% of rice (*USDA NASS*, 2017a,b).

4.3.2.1 Fluxes and Environmental Factors

N_2O fluxes are plotted against crop type in Figure 4.6. The left panel shows what percent of total crop area is occupied by soybean, corn, cotton, and rice. On average these four crops account for 85% of land designated as crops by the CDL in a given subregion, with the rest primarily used for grassland/pasture, hay/non-alfalfa, winter wheat/soybean double crop, fallow/idle land, and various miscellaneous crops. On average, the ratio of cropland was 55:18:8:4 for soybean, corn, cotton, and rice, respectively. The right panel of Figure 4.6 shows crops by total area, with soybean having the greatest variability in total area. *Marinho et al.* (2004) reported mean flux values from soybean crops in the Mississippi Alluvial Plain of 0.2 g N_2O-N ha^{-1} hr^{-1}. The highest fluxes, 1.1 g N_2O-N ha^{-1} hr^{-1}, occurred immediately following a heavy rainfall event similar to the one before the FEAST campaign (*Heimann et al.*,

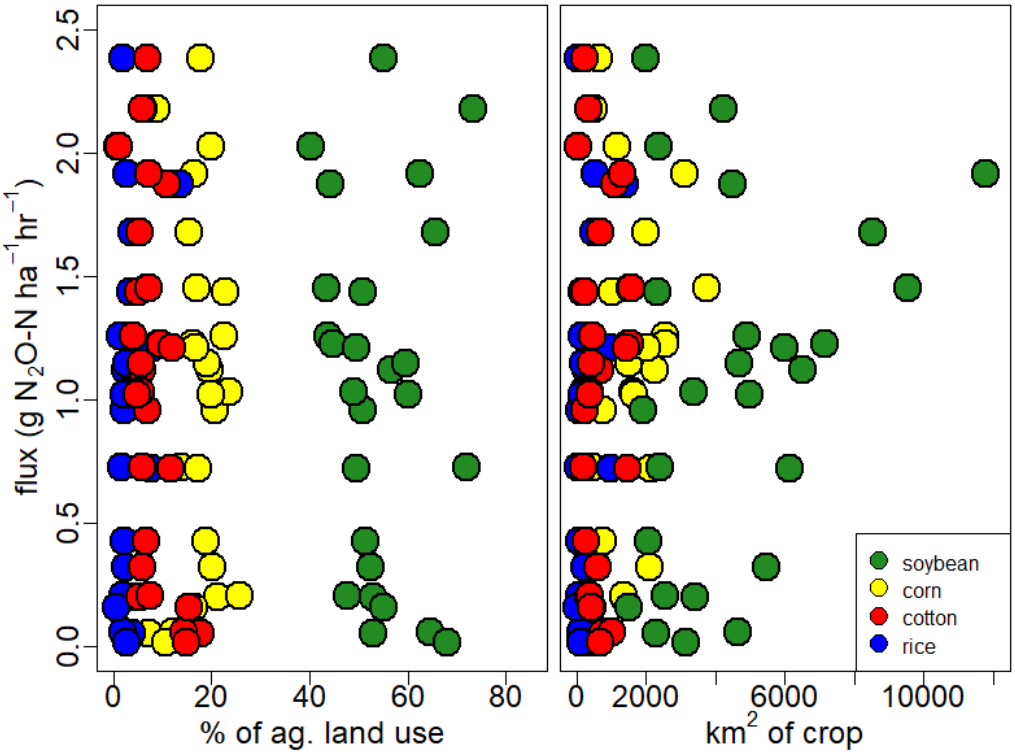

Figure 4.6: Emissions of N_2O-N in g ha^{-1} hr^{-1} for regions in the LMRB plotted against the major crops in the corresponding region: soybean, corn, cotton, and rice. On the left crops are represented as percentage of cropland occupied by each crop, and on the right the crops are represented as total area in km^2.

2018). As soybeans occupy a majority of the cropland in our studied regions, the mean hourly emission estimate of 1.8±1.4 g N_2O-N ha^{-1} hr^{-1} appears to be consistent with *Marinho et al.* (2004).

Fluxes are plotted against fertilizer application rate in Figure 4.7, although the N_2O emissions are hourly and the fertilizer emissions are annual. The fertilizer data is limited as we know annual application rates and how they vary spatially, but not temporally. However, about 75% of fertilizer is applied before or at planting time, with the rest being applied in the fall, intended for crops the following spring (*Padgitt et al.*, 2000). Though the IPCC uses a linear emission factor to estimate N_2O emissions from fertilizer, an analysis by *Shcherbak et al.* (2014) of multiple studies suggests a non-linear, exponential relationship. There is not a clear dependence of

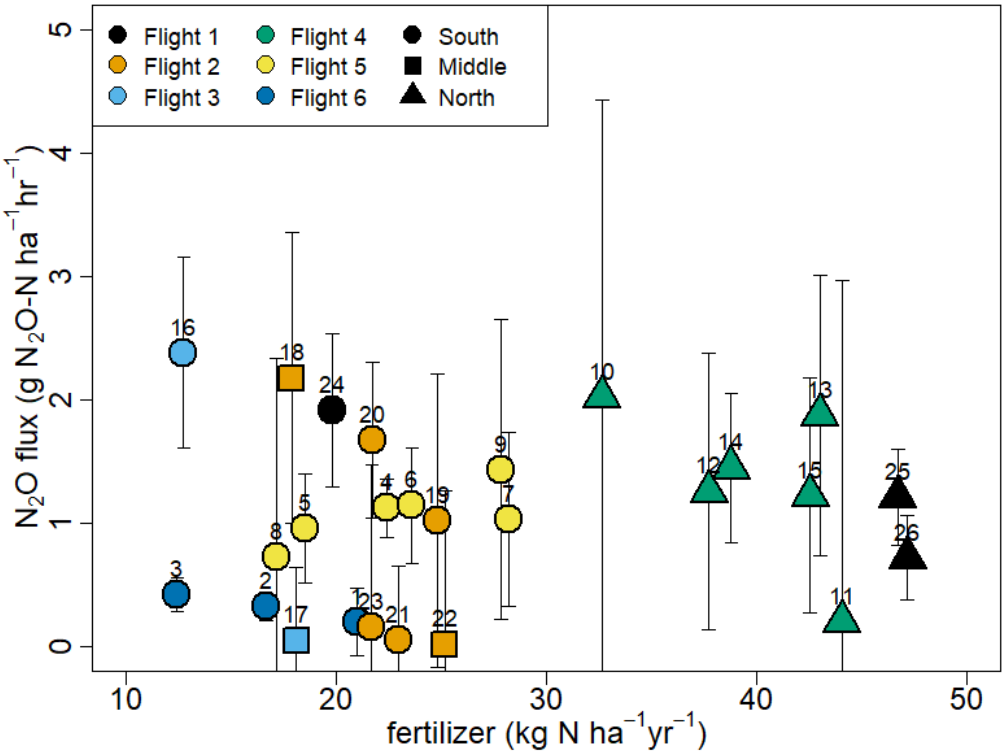

Figure 4.7: Emissions of N_2O-N in g ha^{-1} hr^{-1} for flux regions plotted against annual N from applied fertilizer in 2015 (*Cao et al.*, 2017). Colors denote distinct flights, shapes denote LMRB region, numbers identify each flux region, error bars show 1σ uncertainty.

N_2O flux on fertilizer from our observations. Flights 1 and 4 sampled the northern end of the LMRB which has higher average applied fertilizer than the south, but there is no significant effect on N_2O flux.

Figure 4.8 shows N_2O flux plotted against soil moisture and WFPS from both SMAP and NARR, with a linear fit for soil moisture and an exponential curve from *Smith et al.* (1998) for WFPS. There is a 0.11 cm^3/cm^3 difference in average volumetric water content between SMAP and NARR data. For soil moisture a weak linear dependence is present, as expected from literature (*Dobbie et al.*, 1999; *Smith et al.*, 1998; *Schindlbacher et al.*, 2004). Fitting a regression line confirms the weak relationship, with $R^2 = 0.19$, $p = 0.02$. NARR has no clear dependence, with $R^2 = 0.03$, $p = 0.39$. N_2O flux and WFPS from SMAP agree with the relationship observed

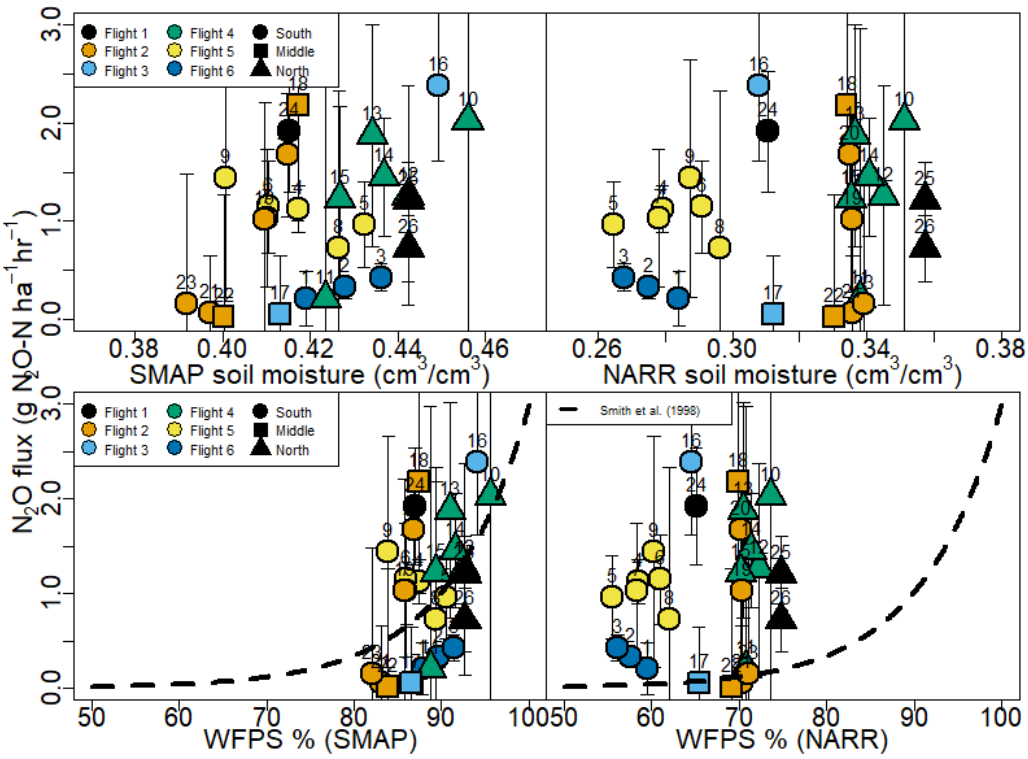

Figure 4.8: Top row: emissions of N_2O-N in g ha^{-1} hr^{-1} in the LMRB plotted against soil moisture as volumetric water content from SMAP and NARR. Bottom row: emissions of N_2O-N plotted against WFPS calculated from SMAP and NARR soil moisture data. Dashed line denotes fit from *Smith et al.* (1998). Colors denote distinct flights, shapes denote LMRB region, numbers identify each flux region, error bars show 1σ uncertainty.

by *Smith et al.* (1998), but WFPS calculated using NARR does not.

Figure 4.9 shows N_2O-N fluxes plotted against soil temperature, along with the exponential relationship observed by *Smith et al.* (1998) using flux chambers. There is a temporal gradient, with higher temperatures during later flights. Flights 5 and 6 also both sampled the southern end of the LMRB and coincided with an observed rise in air temperature throughout the week. Though there was a heavy rain event in late April (*Heimann et al.*, 2018), it primarily affected the northern part of the LMRB, so evaporative cooling is not a likely explanation. Comparing to the relationship from *Smith et al.* (1998), temperature alone does not seem to be a strong factor for N_2O flux.

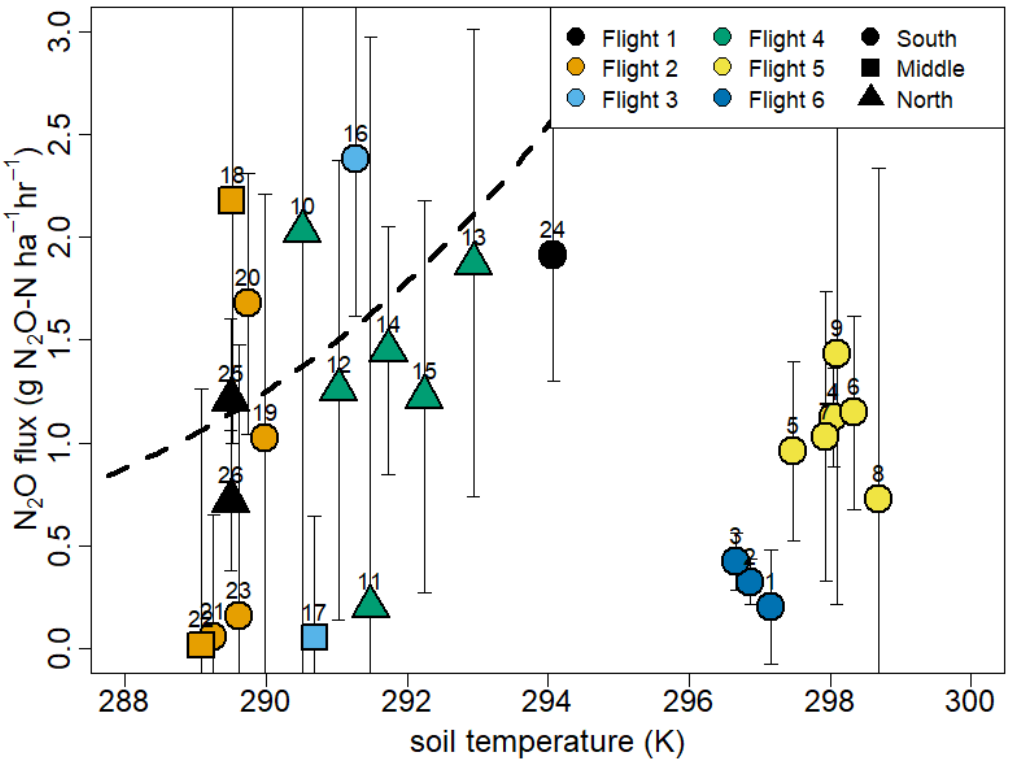

Figure 4.9: Emissions of N_2O-N in g ha^{-1} hr^{-1} in the LMRB plotted against the soil temperature from NARR. Dashed line denotes fit from *Smith et al.* (1998). Colors denote distinct flights, shapes denote LMRB region, numbers identify each flux region, error bars show 1σ uncertainty.

To assess the relative emergent role of these driving variables, we perform a multiple linear regression analysis with crop type, applied fertilizer, soil moisture, and soil temperature to predict N_2O flux. The resultant fit produced an R^2 value of 0.64, and a p value of 0.01. The strongest predictors that emerge from this analysis are soil moisture from SMAP, and total planted area of soybean, cotton, and rice. A multiple linear regression model with only those four variables had an $R^2 = 0.54$, $p = 0.001$. Although fertilizer is expected to be a strong driver of N_2O emissions, the temporal elements of its application are not represented by annual data. Since this analysis relates hourly N_2O emissions to annual fertilizer application, it is understandable that the fertilizer does not significantly predict N_2O. The crop type may be acting as a proxy for the actual applied fertilizer amount, capturing fertilizer timing and variation in management practice. While previous studies have observed a positive relationship between emissions and soil temperature, it is possible that the soil temperature effect is being dwarfed by other factors such as soil moisture.

4.4 Implications

Observed N_2O and CO_2 emissions from two productive fertilizer plants agree with reported emissions, showing no evidence that emissions of these greenhouse gases are under- or over-estimated in inventories. Our observed emissions of CH_4 from the two plants, however, are greatly in excess of reported emissions. Though emissions exceeding expectation by multiple orders of magnitude may appear to be unrealistic, these emissions are consistent with a fugitive emission rate of $\sim$1%, a leakage rate consistent with observations from other portions of the natural gas supply chain (*Schwietzke et al.*, 2014). Although the observed emissions are orders of magnitude higher than expected, the increased CH_4 emissions do not significantly impact the overall footprint of the fertilizer plants, corresponding to a 0.9% increase in total CO_2e emissions for Plant 1 and a 0.2% increase for Plant 2. The large emissions

of CO_2 and N_2O render the loss of CH_4 relatively unimportant. The fugitive CH_4 emissions may be modest in this case, but it is an addressable emissions source and is under-estimated in current CH_4 inventories, thus representing another discrepancy in inventory representation of CH_4 emissions.

Regional sampling of the LMRB enabled the investigation of emissions at a unique spatial scale. Surprisingly, we observed significant variability in N_2O emissions in the various sub-regions sampled. Though the emissions magnitude and variability we observed is consistent with flux chamber measurements, we would have expected far less variability in the regional flights that integrate over many fields with different crops and farming practices. Considering the variability we observed, soil moisture and crop type proved to be the strongest emergent predictors of emissions. This suggests knowing the crop (and inherently thus the soil type and fertilizer practice) combined with soil moisture can predict N_2O variability, and highlights the role of soil moisture in predicting N_2O flux. Future work evaluating how process-based models predict N_2O emissions to vary in this domain will enable evaluation of process representations on regional spatial scales.

4.5 Conclusions

This work highlights the capability of continuous airborne observations to quantify atmospheric greenhouse gas emissions from agricultural activity similar to what has been done in the oil and gas sector. We quantify two productive fertilizer plants with significant production capacity of ammonia and nitric acid and find good agreement with GHGRP-reported emissions and observed N_2O and CO_2 emission rates. Observed CH_4 emissions are several orders of magnitude higher, and suggest a natural gas leakage rate of $\sim$1%. Replacing GHGRP-reported values with the observed emissions raises the CH_4 fractional contribution to total plant emissions by a factor of 100, but the overall footprint is not significantly increased.

We quantify regional N_2O fluxes using the mass balance technique, the first example of this approach to agricultural N_2O emissions, demonstrating proof-of-concept. We find fluxes on the order of 1.8±1.4 g N_2O-N ha^{-1} hr^{-1}, with large variability between regions. We investigate relationships between emissions and several factors known to impact N_2O: crop type, nitrogen from fertilizer application, soil moisture, and soil temperature. For our flights we find the strongest predictors of N_2O emissions are soil moisture, soybean area, cotton area, and rice area. Soil temperature and annual applied fertilizer appear less predictive. The emission fluxes are broadly consistent with fluxes reported in literature. Our method encompasses all emissions from the agricultural regions, with total areas ranging from 5000 to 37000 km^2.

Future studies would benefit from observations of more fertilizer plants. A larger dataset could reveal if CH_4 leakage is a persistent phenomenon at fertilizer facilities. Direct knowledge of a facility's production rate would help reduce variability in scaling from annual to hourly emissions, though that information may not be easily available. Comparing the results of these flights with output from a process-based model for May 2017 in the region of interest would allow direct comparison with expected N_2O fluxes as well as evaluation of the models' predicted sensitivity to underlying variables such as applied fertilizer, soil moisture, or soil temperature. The type of airborne observations presented here could potentially be used to assess the efficiency of various management practices by farms, evaluating if whole field emissions vary depending on specific practices.

CHAPTER V

Conclusions

5.1 Summary

This dissertation focuses on using airborne observations to quantify greenhouse gas emissions from the energy and agricultural sectors. Deployment on an airborne platform enables both broad regional sampling as well as the capability to target particular sources or areas. The use of mid-infrared laser spectroscopy provides high-accuracy and high-precision measurements of key trace gas species on a 1 Hz time basis, allowing for in-flight tracking and improved attribution of emissions.

We conducted the largest in-field study of flaring efficiency. In the Bakken Shale we evaluated flaring emissions of CH_4, C_2H_6, and BC. We discovered emissions of all three gases followed a skewed distribution, with the top 25% of flares contributing $\sim$66% of CH_4 and C_2H_6 emissions, though BC emissions are lower than expected and do not correlate with emissions of CH_4. With the skewed distribution, total emissions from flaring could account for 21% of CH_4 emitted from the Bakken region and 17% of C_2H_6, more than double the fraction if standard flare efficiency is assumed. Global emissions of CH_4 from flaring could be $\sim$2.5 times higher than estimated, suggesting the need to consider variation in flare efficiency for inventories and estimates and the possibility of disproportionate emissions.

We integrated an N_2O, CO_2, CO, and H_2O laser spectrometer into a new airborne

measurement system, FCHAOS. A repeatable cabin pressure-dependency was diagnosed and resolved with high-frequency calibrations, achieving in-flight 1σ precisions of 0.05 ppb, 0.1 ppm, 1 ppb, and 10 ppm for N_2O, CO_2, CO, and H_2O respectively, and traceability to WMO standards (1σ) of 0.28 ppb, 0.33 ppm, and 1.92 ppb for N_2O, CO_2, and CO. This instrument provides the current best airborne N_2O measurements in terms of duty cycle, precision, and accuracy, enabling airborne N_2O studies not previously possible.

Using this newly developed airborne system, we quantified greenhouse gas emissions from fertilizer production and agricultural sources in the Lower Mississippi River Basin. Two fertilizer plants were sampled and rates of emissions were quantified. When compared with reported emissions from the GHGRP, N_2O and CO_2 emissions agreed well within uncertainty. The CO_2 emissions between two instruments also agreed, and observations made for one plant on two consecutive days were consistent. However, CH_4 emissions were 20 times larger than reported emissions for one plant and 100 times larger for the other. These emissions are consistent with a loss rate of 0.6–1.2%. Regional N_2O fluxes were calculated for the first time using the airborne mass balance approach, and compared with crop type, applied fertilizer, soil temperature, and soil moisture. We found the most significant predictors of N_2O flux were soil moisture and total crop area of soybean, cotton, and rice. N_2O fluxes were consistent with expected values based on literature, and this approach allows for the possibility to directly quantify total emissions from farms and large agricultural regions without having to scale up flux chamber data.

5.2 Further Directions

There are several avenues to build upon this thesis. While we report efficiency for the largest ever sample of real-world flares, it is still 37 out of $\sim$5500 in the Bakken. More observations of flares in real-world settings with varying operating conditions

and gas compositions in different environments are needed to improve global efficiency calculations.

The fertilizer plant analysis would also be significantly improved by more observations. Quantifying emissions from more than two fertilizer plants on multiple days or throughout the year would help define any temporal variability in the results and identify common characteristics among fertilizer plants. It is unknown if the higher CH_4 emissions we observed are present in all fertilizer plants.

Due to seasonality in N_2O, our regional N_2O fluxes could not be scaled up to estimate annual emissions. Model output would allow for a direct comparison for our seasonal observations. The temporal variability could also be elucidated with airborne campaigns during other key periods in N_2O soil emissions such as thawing at the end of winter and post-harvest. Using a particle dispersion model to better attribute emissions and estimate footprints as seen in *Xiang et al.* (2013) would improve linkages of observed N_2O to controlling processes. There is also the potential to investigate CH_4 emissions from rice using the FEAST data set.

BIBLIOGRAPHY

BIBLIOGRAPHY

Abdulkareem, A., J. Odigure, and S. Abenege (2009), Predictive model for pollutant dispersion from gas flaring: a case study of oil producing area of Nigeria, *Energy Sources, Part A*, *31*(12), 1004–1015.

Aikin, A., J. Herman, E. Maier, and C. McQuillan (1982), Atmospheric chemistry of ethane and ethylene, *Journal of Geophysical Research: Oceans*, *87*(C4), 3105–3118.

Aleksandrowicz, L., R. Green, E. J. M. Joy, P. Smith, and A. Haines (2016), The impacts of dietary change on greenhouse gas emissions, land use, water use, and health: A systematic review, *PLOS ONE*, *11*(11), 1–16, doi:10.1371/journal.pone.0165797.

Allen, D. T. (2014), Methane emissions from natural gas production and use: reconciling bottom-up and top-down measurements, *Curr. Opin. Chem. Eng.*, *5*, 78 – 83, doi:http://dx.doi.org/10.1016/j.coche.2014.05.004.

Allen, D. T., D. Smith, V. M. Torres, and F. C. Saldaña (2016), Carbon dioxide, methane and black carbon emissions from upstream oil and gas flaring in the United States, *Current Opinion in Chemical Engineering*, *13*, 119–123.

Alvarez, R. A., S. W. Pacala, J. J. Winebrake, W. L. Chameides, and S. P. Hamburg (2012), Greater focus needed on methane leakage from natural gas infrastructure, *Proceedings of the National Academy of Sciences*.

Amann, M., Z. Klimont, and K. Kupiainen (2011), Integrated assessment of black carbon and tropospheric ozone.

Anenberg, S. C., K. Talgo, S. Arunachalam, P. Dolwick, C. Jang, and J. J. West (2011), Impacts of global, regional, and sectoral black carbon emission reductions on surface air quality and human mortality, *Atmospheric Chemistry and Physics*, *11*(14), 7253–7267, doi:10.5194/acp-11-7253-2011.

Anenberg, S. C., et al. (2012), Global air quality and health co-benefits of mitigating near-term climate change through methane and black carbon emission controls, *Environ. Health Perspect*, *120*(6), 831–839.

Balcombe, P., N. Brandon, and A. Hawkes (2018), Characterising the distribution of methane and carbon dioxide emissions from the natural gas supply chain, *Journal of Cleaner Production*, *172*, 2019 – 2032, doi:https://doi.org/10.1016/j.jclepro.2017.11.223.

Bennetzen, E. H., P. Smith, and J. R. Porter (2016), Decoupling of greenhouse gas emissions from global agricultural production: 1970–2050, *Global Change Biology*, *22*(2), 763–781, doi:10.1111/gcb.13120.

Beychok, M. R. (2005), *Fundamentals Of Stack Gas Dispersion*, fourth ed., 1–193 pp., Milton R. Beychok, 10 Marquette, Apt. 121.

Blake, D. R., and F. S. Rowland (1986), Global atmospheric concentrations and source strength of ethane, *Nature*, *321*(6067), 231.

Blake, N. J., et al. (2003), The seasonal evolution of NMHCs and light alkyl nitrates at middle to high northern latitudes during TOPSE, *Journal of Geophysical Research: Atmospheres*, *108*(D4).

Boissard, C., B. Bonsang, M. Kanakidou, and G. . Lambert (1996), TROPOZ II: Global distributions and budgets of methane and light hydrocarbons, *Journal of atmospheric chemistry*, *25*(2), 115–148.

Bond, T. C., and H. Sun (2005), Can reducing black carbon emissions counteract global warming?

Bond, T. C., et al. (2013), Bounding the role of black carbon in the climate system: A scientific assessment, *Journal of Geophysical Research: Atmospheres*, *118*(11), 5380–5552, doi:10.1002/jgrd.50171.

Bouwman, A. F., K. W. Van der Hoek, and J. G. J. Olivier (1995), Uncertainties in the global source distribution of nitrous oxide, *Journal of Geophysical Research: Atmospheres*, *100*(D2), 2785–2800, doi:10.1029/94JD02946.

Bouwman, A. F., L. J. M. Boumans, and N. H. Batjes (2002), Emissions of N_2O and NO from fertilized fields: Summary of available measurement data, *Global Biogeochemical Cycles*, *16*(4), 6–1–6–13, doi:10.1029/2001GB001811.

Braker, G., and R. Conrad (2011), Chapter 2 - diversity, structure, and size of n_2o-producing microbial communities in soils—what matters for their functioning?, pp. 33 – 70, Academic Press, doi:https://doi.org/10.1016/B978-0-12-387046-9.00002-5.

Brandt, A., T. Yeskoo, S. McNally, K. Vafi, H. Cai, and M. Wang (2015), Energy intensity and greenhouse gas emissions from crude oil production in the Bakken formation: Input data and analysis methods.

Brandt, A. R., G. A. Heath, and D. Cooley (2016), Methane leaks from natural gas systems follow extreme distributions, *Environmental Science & Technology*, *50*(22), 12,512–12,520.

Brandt, A. R., et al. (2014), Methane leaks from North American natural gas systems, *Science*, *343*(6172), 733–735, doi:10.1126/science.1247045.

Brentrup, F., J. Küsters, J. Lammel, and H. Kuhlmann (2000), Methods to estimate on-field nitrogen emissions from crop production as an input to LCA studies in the agricultural sector, *The International Journal of Life Cycle Assessment*, *5*(6), 349, doi:10.1007/BF02978670.

Brentrup, F., C. Pallière, et al. (2008), GHG emissions and energy efficiency in European nitrogen fertiliser production and use., in *Proceedings-International Fertiliser Society*, 639, pp. 1–25, International Fertiliser Society.

Brown, L., S. Armstrong Brown, S. C. Jarvis, B. Syed, K. W. T. Goulding, V. R. Phillips, R. W. Sneath, and B. F. Pain (2001), An inventory of nitrous oxide emissions from agriculture in the UK using the IPCC methodology: emission estimate, uncertainty and sensitivity analysis, *Atmospheric Environment*, *35*, 1439–1449, doi:10.1016/S1352-2310(00)00361-7.

Burney, J. A., S. J. Davis, and D. B. Lobell (2010), Greenhouse gas mitigation by agricultural intensification, *Proceedings of the National Academy of Sciences*, *107*(26), 12,052–12,057, doi:10.1073/pnas.0914216107.

Butler, J. H., and S. A. Montzka (2018), The NOAA Annual Greenhouse Gas Index (AGGI), *NOAA Earth System Research Laboratory*.

Butterbach-Bahl, K., E. M. Baggs, M. Dannenmann, R. Kiese, and S. Zechmeister-Boltenstern (2013), Nitrous oxide emissions from soils: how well do we understand the processes and their controls?, *Philosophical Transactions of the Royal Society B: Biological Sciences*, *368*(1621), 20130,122, doi:10.1098/rstb.2013.0122.

Cambaliza, M., et al. (2014), Assessment of uncertainties of an aircraft-based mass balance approach for quantifying urban greenhouse gas emissions, *Atmospheric Chemistry and Physics*, *14*(17), 9029–9050.

Cao, P., C. Lu, and Z. Yu (2017), Agricultural nitrogen fertilizer uses in the continental U.S. during 1850–2015: a set of gridded time-series data, doi:10.1594/PANGAEA.883585, supplement to: Cao, P et al. (in review): Historical Nitrogen Fertilizer Use in Agricultural Ecosystem of the Continental U.S. during 1850-2015: Application rate, Timing, and Fertilizer Types. Earth System Science Data.

Cao, P., C. Lu, and Z. Yu (2018), Historical nitrogen fertilizer use in agricultural ecosystems of the contiguous United States during 1850–2015: application rate, timing, and fertilizer types, *Earth System Science Data*, *10*(2), 969–984, doi:10.5194/essd-10-969-2018.

Caulton, D. R., P. B. Shepson, M. O. Cambaliza, D. McCabe, E. Baum, and B. H. Stirm (2014a), Methane destruction efficiency of natural gas flares associated with shale formation wells, *Environ. Sci. Technol.*, *48*(16), 9548–9554.

Caulton, D. R., et al. (2014b), Toward a better understanding and quantification of methane emissions from shale gas development, *Proceedings of the National Academy of Sciences*, *111*(17), 6237–6242, doi:10.1073/pnas.1316546111.

Cavigelli, M. A., S. J. D. Grosso, M. A. Liebig, C. S. Snyder, P. E. Fixen, R. T. Venterea, A. B. Leytem, J. E. McLain, and D. B. Watts (2012), US agricultural nitrous oxide emissions: context, status, and trends, *Frontiers in Ecology and the Environment*, *10*(10), 537–546.

Chadwick, D., et al. (2014), Optimizing chamber methods for measuring nitrous oxide emissions from plot-based agricultural experiments, *European Journal of Soil Science*, *65*(2), 295–307.

Chen, H., A. Karion, C. W. Rella, J. Winderlich, C. Gerbig, A. Filges, T. Newberger, C. Sweeney, and P. P. Tans (2013), Accurate measurements of carbon monoxide in humid air using the cavity ring-down spectroscopy (CRDS) technique, *Atmospheric Measurement Techniques*, *6*(4), 1031–1040, doi:10.5194/amt-6-1031-2013.

Chen, H., et al. (2010), High-accuracy continuous airborne measurements of greenhouse gases (CO_2 and CH_4) using the cavity ring-down spectroscopy (CRDS) technique, *Atmospheric Measurement Techniques*, *3*(2), 375–386, doi:10.5194/amt-3-375-2010.

Chen, Z., et al. (2016), Partitioning N_2O emissions within the U.S. Corn Belt using an inverse modeling approach, *Global Biogeochemical Cycles*, *30*(8), 1192–1205, doi:10.1002/2015GB005313, 2015GB005313.

Ciais, P., et al. (2013), *Carbon and other biogeochemical cycles*, pp. 465–570, Cambridge University Press.

Clark, M., and D. Tilman (2017), Comparative analysis of environmental impacts of agricultural production systems, agricultural input efficiency, and food choice, *Environmental Research Letters*, *12*(6), 064,016.

Collins, W., R. Derwent, C. Johnson, and D. Stevenson (2002), The oxidation of organic compounds in the troposphere and their global warming potentials, *Climatic Change*, *52*(4), 453–479.

Conley, S., et al. (2017), Application of Gauss's theorem to quantify localized surface emissions from airborne measurements of wind and trace gases, *Atmospheric Measurement Techniques*, *10*(9), 3345–3358, doi:10.5194/amt-10-3345-2017.

Conley, S. A., I. C. Faloona, D. H. Lenschow, A. Karion, and C. Sweeney (2014), A low-cost system for measuring horizontal winds from single-engine aircraft, *Journal of Atmospheric and Oceanic Technology*, *31*(6), 1312–1320, doi:10.1175/JTECH-D-13-00143.1.

Crosson, E. (2008), A cavity ring-down analyzer for measuring atmospheric levels of methane, carbon dioxide, and water vapor, *Applied Physics B*, *92*(3), 403–408, doi:10.1007/s00340-008-3135-y.

Curl, R. F., F. Capasso, C. Gmachl, A. A. Kosterev, B. McManus, R. Lewicki, M. Pusharsky, G. Wysocki, and F. K. Tittel (2010), Quantum cascade lasers in chemical physics, *Chemical Physics Letters*, *487*(1-3), 1–18.

Dalal, R. C., W. Wang, G. P. Robertson, and W. J. Parton (2003), Nitrous oxide emission from Australian agricultural lands and mitigation options: a review, *Australian Journal of Soil Research*, *41*(2), 165, doi:10.1071/sr02064.

Davidson, E. A. (2009), The contribution of manure and fertilizer nitrogen to atmospheric nitrous oxide since 1860, *Nature Geoscience*, *2*, 659, article.

Davidson, E. A., and D. Kanter (2014), Inventories and scenarios of nitrous oxide emissions, *Environmental Research Letters*, *9*(10), 105,012.

De Prins, S., et al. (2014), Airway oxidative stress and inflammation markers in exhaled breath from children are linked with exposure to black carbon, *Environment international*, *73*, 440–446.

Del Grosso, S., W. J Parton, A. Mosier, M. K Walsh, D. S Ojima, and P. E Thornton (2006), DAYCENT national-scale simulations of nitrous oxide emissions from cropped soils in the United States, *Journal of Environmental Quality*, *35*, 1451–60.

Denmead, O. T. (2008), Approaches to measuring fluxes of methane and nitrous oxide between landscapes and the atmosphere, *Plant and Soil*, *309*(1), 5–24, doi: 10.1007/s11104-008-9599-z.

Desjardins, R., S. Kulshreshtha, B. Junkins, W. Smith, B. Grant, and M. Boehm (2001), Canadian greenhouse gas mitigation options in agriculture, *Nutrient Cycling in Agroecosystems*, *60*(1), 317–326, doi:10.1023/A:1012697912871.

Dlugokencky, E., et al. (2009), Observational constraints on recent increases in the atmospheric CH_4 burden, *Geophysical Research Letters*, *36*(18).

Dlugokencky, E. J., R. C. Myers, P. M. Lang, K. A. Masarie, A. M. Crotwell, K. W. Thoning, B. D. Hall, J. W. Elkins, and L. P. Steele (2005), Conversion of NOAA atmospheric dry air CH_4 mole fractions to a gravimetrically prepared standard scale, *Journal of Geophysical Research: Atmospheres*, *110*(D18), doi: 10.1029/2005JD006035.

Dobbie, K. E., I. P. McTaggart, and K. A. Smith (1999), Nitrous oxide emissions from intensive agricultural systems: Variations between crops and seasons, key driving variables, and mean emission factors, *Journal of Geophysical Research: Atmospheres*, *104*(D21), 26,891–26,899, doi:10.1029/1999JD900378.

Du, Z., S. Zhang, J. Li, N. Gao, and K. Tong (2019), Mid-infrared tunable laser-based broadband fingerprint absorption spectroscopy for trace gas sensing: A review, *Applied Sciences*, *9*(2), 338.

Duffy, P. B., et al. (2019), Strengthened scientific support for the endangerment finding for atmospheric greenhouse gases, *Science*, *363*(6427), eaat5982.

EFMA (2000), *Production of Nitric Acid. Booklet No. 2 of 8: Best Available Techniques for Pollution Control in the European Fertilizer Industry*, European Fertilizer Manufacturers' Association, Ave. E van Nieuwenhuyse 4, B-1160 Brussels, Belgium.

Ehrhardt, F., et al. (2017), Assessing uncertainties in crop and pasture ensemble model simulations of productivity and N_2O emissions, *Global Change Biology*, *24*(2), e603–e616, doi:10.1111/gcb.13965.

EIA (2016), Natural gas gross withdrawals and production, `https://www.eia.gov/dnav/ng/ng_prod_sum_a_EPG0_VGV_mmcf_a.htm`.

EIA (2019a), Natural gas gross withdrawals and production, `https://www.eia.gov/dnav/ng/ng_prod_sum_a_EPG0_FGW_mmcf_a.htm`.

EIA (2019b), Crude oil production, `https://www.eia.gov/dnav/pet/pet_crd_crpdn_adc_mbbl_a.htm`.

EIA (2019c), Eia adds new play production data to shale gas and tight oil reports, `https://www.eia.gov/todayinenergy/detail.php?id=38372`.

EIA (2019d), *Annual Energy Outlook 2019*, Government Printing Office.

Elvidge, C. D., D. Ziskin, K. E. Baugh, B. T. Tuttle, T. Ghosh, D. W. Pack, E. H. Erwin, and M. Zhizhin (2009), A Fifteen Year Record of Global Natural Gas Flaring Derived from Satellite Data, *Energies*, *2*(3), 595, doi:10.3390/en20300595.

Elvidge, C. D., M. Zhizhin, K. Baugh, F.-C. Hsu, and T. Ghosh (2016), Methods for Global Survey of Natural Gas Flaring from Visible Infrared Imaging Radiometer Suite Data, *Energies*, *9*(1), 14.

EPA (1998), Basis and purpose document on specifications for hydrogen-fueled flares, `http://www.tceq.state.tx.us/assets/public/implementation/air/rules/Flare/Resource_5.pdf`.

EPA (2017), Greenhouse Gas Reporting Program (GHGRP) FLIGHT Data system, `http://ghgdata.epa.gov/ghgp/`.

EPA (2018), Inventory of U.S. greenhouse gas emissions and sinks: 1990-2016.

EPA OAQPS (2012), Parameters for properly designed and operated flares, *Tech. rep.*, U.S. EPA Office of Air Quality Planning and Standards (OAQPS).

Erisman, J., M. Sutton, J. Galloway, Z. Klimont, and W. Winiwarter (2008), How a century of ammonia synthesis changed the world, *Nature Geoscience*, *1*(10), 636–639, doi:10.1038/ngeo325.

FAO (2017), World fertilizer trends and outlook to 2020.

FAO (2019), Food and Agriculture Organization of the United Nations statistical database, `http://www.fao.org/faostat/en`, accessed January 15, 2019.

FAO, IFAD, UNICEF, WFP, and WHO (2018), *The State of Food Security and Nutrition in the World 2018. Building climate resilience for food security and nutrition.*, FAO, Rome, license: CC BY-NC-SA 3.0 IGO.

Fawole, O. G., X.-M. Cai, and A. MacKenzie (2016), Gas flaring and resultant air pollution: A review focusing on black carbon, *Environmental pollution*, *216*, 182–197.

Filges, A., C. Gerbig, H. Chen, H. Franke, C. Klaus, and A. Jordan (2015), The IAGOS-core greenhouse gas package: a measurement system for continuous airborne observations of CO_2, CH_4, H_2O and CO, *Tellus B: Chemical and Physical Meteorology*, *67*(1), 27,989, doi:10.3402/tellusb.v67.27989.

Flamant, C., et al. (2018), The dynamics–aerosol–chemistry–cloud interactions in West Africa field campaign: Overview and research highlights, *Bulletin of the American Meteorological Society*, *99*(1), 83–104.

Flanner, M. G., C. S. Zender, J. T. Randerson, and P. J. Rasch (2007), Present-day climate forcing and response from black carbon in snow, *Journal of Geophysical Research: Atmospheres*, *112*(D11).

Flechard, C., et al. (2007), Effects of climate and management intensity on nitrous oxide emissions in grassland systems across Europe, *Agriculture, Ecosystems & Environment*, *121*(1), 135 – 152, doi:https://doi.org/10.1016/j.agee.2006.12.024, the Greenhouse Gas Balance of Grasslands in Europe.

Foley, J. A., et al. (2011), Solutions for a cultivated planet, *Nature*, *478*(7369), 337.

Fossum, J.-P. (2014), Calculation of carbon footprint of fertilizer production, `http://www.yara.com/doc/122597_2013_Carbon_footprintof_AN_Method_of_calculation.pdf`.

Franco, B., et al. (2015), Retrieval of ethane from ground-based FTIR solar spectra using improved spectroscopy: Recent burden increase above Jungfraujoch, *Journal of Quantitative Spectroscopy and Radiative Transfer*, *160*, 36–49.

Franco, B., et al. (2016), Evaluating ethane and methane emissions associated with the development of oil and natural gas extraction in North America, *Environmental Research Letters*, *11*(4), 044,010.

Frankenberg, C., S. S. Kulawik, S. C. Wofsy, F. Chevallier, B. Daube, E. A. Kort, C. O'Dell, E. T. Olsen, and G. Osterman (2016a), Using airborne HIAPER Pole-to-Pole Observations (HIPPO) to evaluate model and remote sensing estimates of atmospheric carbon dioxide, *Atmospheric Chemistry and Physics*, *16*(12), 7867–7878, copyright - Copyright Copernicus GmbH 2016; Last updated - 2018-01-23.

Frankenberg, C., et al. (2016b), Airborne methane remote measurements reveal heavy-tail flux distribution in Four Corners region, *Proceedings of the National Academy of Sciences*, *113*(35), 9734–9739, doi:10.1073/pnas.1605617113.

Fried, A., and D. Richter (2007), *Infrared Absorption Spectroscopy*, chap. 2, pp. 72–146, John Wiley & Sons, Ltd, doi:10.1002/9780470988510.ch2.

Fried, A., G. Diskin, P. Weibring, D. Richter, J. Walega, G. Sachse, T. Slate, M. Rana, and J. Podolske (2008), Tunable infrared laser instruments for airborne atmospheric studies, *Applied Physics B*, *92*(3), 409–417, doi:10.1007/s00340-008-3136-x.

Gellings, C. W., and K. E. Parmenter (2016), Energy efficiency in fertilizer production and use, *Efficient Use and Conservation of Energy; Gellings, CW, Ed.; Encyclopedia of Life Support Systems*, pp. 123–136.

Ghormley, J., R. Ellsworth, and C. Hochanadel (1973), Reaction of excited oxygen atoms with nitrous oxide. Rate constants for reaction of ozone with nitric oxide and with nitrogen dioxide, *The Journal of Physical Chemistry*, *77*(11), 1341–1345.

Grace, P. R., G. P. Robertson, N. Millar, M. Colunga-Garcia, B. Basso, S. H. Gage, and J. Hoben (2011), The contribution of maize cropping in the Midwest USA to global warming: A regional estimate, *Agricultural Systems*, *104*(3), 292–296.

Grant, R., E. Pattey, T. Goddard, L. Kryzanowski, and H. Puurveen (2006), Modeling the effects of fertilizer application rate on nitrous oxide emissions, *Soil Science Society of America Journal*, *70*, 235–248., doi:10.2136/sssaj2005.0104.

Griffis, T. J., Z. Chen, J. M. Baker, J. D. Wood, D. B. Millet, X. Lee, R. T. Venterea, and P. A. Turner (2017), Nitrous oxide emissions are enhanced in a warmer and wetter world, *Proceedings of the National Academy of Sciences*, *114*(45), 12,081–12,085, doi:10.1073/pnas.1704552114.

Gvakharia, A., E. A. Kort, A. Brandt, J. Peischl, T. B. Ryerson, J. P. Schwarz, M. L. Smith, and C. Sweeney (2017), Methane, Black Carbon, and Ethane Emissions from Natural Gas Flares in the Bakken Shale, North Dakota, *Environmental Science & Technology*, *51*(9), 5317–5325, doi:10.1021/acs.est.6b05183, pMID: 28401762.

Gvakharia, A., E. A. Kort, M. L. Smith, and S. Conley (2018), Testing and evaluation of a new airborne system for continuous N_2O, co_2, CO, and H_2O measurements: the Frequent Calibration High-performance Airborne Observation System (FCHAOS), *Atmospheric Measurement Techniques*, *11*(11), 6059–6074, doi:10.5194/amt-11-6059-2018.

Haines, A., and K. Ebi (2019), The imperative for climate action to protect health, *New England Journal of Medicine*, *380*(3), 263–273.

Hall, B. D., G. S. Dutton, and J. W. Elkins (2007), The NOAA nitrous oxide standard scale for atmospheric observations, *Journal of Geophysical Research: Atmospheres*, *112*(D9), doi:10.1029/2006JD007954.

Hasler, K., S. Bröring, S. Omta, and H.-W. Olfs (2015), Life cycle assessment (LCA) of different fertilizer product types, *European Journal of Agronomy*, *69*, 41 – 51, doi:https://doi.org/10.1016/j.eja.2015.06.001.

Haus, R., R. Wilkinson, J. Heland, and K. Schafer (1998), Remote sensing of gas emissions on natural gas flares, *Pure and Applied Optics: Journal of the European Optical Society Part A*, *7*(4), 853.

Hausmann, P., R. Sussmann, and D. Smale (2016), Contribution of oil and natural gas production to renewed increase in atmospheric methane (2007–2014): top–down estimate from ethane and methane column observations, *Atmospheric Chemistry and Physics*, *16*(5), 3227–3244.

Heard, D. (2008), *Analytical Techniques for Atmospheric Measurement*, John Wiley & Sons.

Heimann, D. C., R. R. Holmes Jr., and T. E. Harris (2018), Flooding in the southern Midwestern United States, April–May 2017, *Tech. rep.*, USGS, Reston, VA, report.

Helmig, D., et al. (2016), Reversal of global atmospheric ethane and propane trends largely due to US oil and natural gas production, *Nature Geoscience*, *9*(7), 490.

Hink, L., C. Gubry-Rangin, G. W. Nicol, and J. I. Prosser (2018), The consequences of niche and physiological differentiation of archaeal and bacterial ammonia oxidisers for nitrous oxide emissions, *The ISME Journal*, *12*(4), 1084–1093, doi:10.1038/s41396-017-0025-5.

Hodnebrog, Ø., S. B. Dalsøren, and G. Myhre (2018), Lifetimes, direct and indirect radiative forcing, and global warming potentials of ethane (C_2H_6), propane (C_3H_8), and butane (C_4H_{10}), *Atmospheric Science Letters*, *19*(2).

Hofmann, D. J., J. H. Butler, E. J. Dlugokencky, J. W. Elkins, K. Masarie, S. A. Montzka, and P. Tans (2006), The role of carbon dioxide in climate forcing from 1979 to 2004: introduction of the Annual Greenhouse Gas Index, *Tellus B: Chemical and Physical Meteorology*, *58*(5), 614–619.

Holmes, C. D. (2018), Methane feedback on atmospheric chemistry: Methods, models, and mechanisms, *Journal of Advances in Modeling Earth Systems*, *10*(4), 1087–1099.

Hu, H.-W., J.-Z. He, and D. Chen (2015), Microbial regulation of terrestrial nitrous oxide formation: understanding the biological pathways for prediction of emission rates, *FEMS Microbiology Reviews*, *39*(5), 729–749, doi:10.1093/femsre/fuv021.

IEA (2018a), *Key World Energy Statistics 2018*, 51 pp., International Energy Agency, doi:https://doi.org/https://doi.org/10.1787/key_energ_stat-2018-en.

IEA (2018b), *World Energy Balances 2018*, 762 pp., International Energy Agency, doi:https://doi.org/10.1787/world_energy_bal-2018-en.

IEA (2018c), *World Energy Outlook 2018*, 661 pp., International Energy Agency, doi:https://doi.org/10.1787/weo-2018-en.

Inoue, M., et al. (2016), Bias corrections of GOSAT SWIR XCO_2 and XCH_4 with TCCON data and their evaluation using aircraft measurement data, *Atmospheric Measurement Techniques*, *9*(8), 3491–3512, doi:10.5194/amt-9-3491-2016.

IPCC (2013), Summary for Policymakers, in *Climate Change 2013: The Physical Science Basis. Contribution of Working Group I to the Fifth Assessment Report of the Intergovernmental Panel on Climate Change*, edited by T. Stocker, D. Qin, G.-K. Plattner, M. Tignor, S. Allen, J. Boschung, A. Nauels, Y. Xia, V. Bex, and P. Midgley, book section SPM, p. 1–30, Cambridge University Press, Cambridge, United Kingdom and New York, NY, USA, doi:10.1017/CBO9781107415324.004.

Ismail, O., and G. Umukoro (2012), Global impact of gas flaring, *Energy and Power Engineering*, *4*(4), 290 – 302, doi:10.4236/epe.2012.44039.

Janssen, N. A., et al. (2011), Black carbon as an additional indicator of the adverse health effects of airborne particles compared with PM10 and PM2.5, *Environmental health perspectives*, *119*(12), 1691–1699.

Johnson, M., and L. Kostiuk (2000), Efficiencies of low-momentum jet diffusion flames in crosswinds, *Combustion and Flame*, *123*(1–2), 189 – 200, doi:http://dx.doi.org/10.1016/S0010-2180(00)00151-6.

Johnson, M., and L. Kostiuk (2002), A parametric model for the efficiency of a flare in crosswind, *Proceedings of the Combustion Institute*, *29*(2), 1943 – 1950, doi:http://dx.doi.org/10.1016/S1540-7489(02)80236-X.

Kahforoushan, D., E. Fatehifar, and J. Soltan (2010), The estimation of CO_2 emission factors for combustion sources in oil and gas processing plants, *Energy Sources, Part A: Recovery, Utilization, and Environmental Effects*, *33*(3), 202–210, doi:10.1080/15567031003627922.

Karion, A., C. Sweeney, S. Wolter, T. Newberger, H. Chen, A. Andrews, J. Kofler, D. Neff, and P. Tans (2013), Long-term greenhouse gas measurements from aircraft, *Atmospheric Measurement Techniques*, *6*(3), 511–526, doi:10.5194/amt-6-511-2013.

Karion, A., et al. (2015), Aircraft-based estimate of total methane emissions from the Barnett Shale region, *Environmental Science & Technology*, *49*(13), 8124–8131, doi:10.1021/acs.est.5b00217, pMID: 26148550.

Kavdir, Y., H. Hellebrand, and J. Kern (2008), Seasonal variations of nitrous oxide emission in relation to nitrogen fertilization and energy crop types in sandy soil, *Soil and Tillage Research*, *98*(2), 175 – 186, doi:https://doi.org/10.1016/j.still.2007.11.002.

Knighton, W. B., S. C. Herndon, J. F. Franklin, E. C. Wood, J. Wormhoudt, W. Brooks, E. C. Fortner, and D. T. Allen (2012), Direct measurement of volatile organic compound emissions from industrial flares using real-time online techniques: Proton Transfer Reaction Mass Spectrometry and Tunable Infrared Laser Differential Absorption Spectroscopy, *Ind. Eng. Chem. Res.*, *51*(39), 12,674–12,684, doi: 10.1021/ie202695v.

Kort, E. A., C. Frankenberg, K. R. Costigan, R. Lindenmaier, M. K. Dubey, and D. Wunch (2014), Four Corners: The largest US methane anomaly viewed from space, *Geophysical Research Letters*, *41*(19), 6898–6903.

Kort, E. A., M. L. Smith, L. T. Murray, A. Gvakharia, A. R. Brandt, J. Peischl, T. B. Ryerson, C. Sweeney, and K. Travis (2016), Fugitive emissions from the Bakken shale illustrate role of shale production in global ethane shift, *Geophysical Research Letters*, *43*(9), 4617–4623, doi:10.1002/2016GL068703, 2016GL068703.

Kort, E. A., et al. (2008), Emissions of CH_4 and N_2O over the United States and Canada based on a receptor-oriented modeling framework and COBRA-NA atmospheric observations, *Geophysical Research Letters*, *35*(18), doi:10.1029/2008GL034031.

Kort, E. A., et al. (2011), Tropospheric distribution and variability of N_2O: Evidence for strong tropical emissions, *Geophysical Research Letters*, *38*(15), doi:10.1029/2011GL047612.

Le Texier, H., S. Solomon, and R. Garcia (1988), The role of molecular hydrogen and methane oxidation in the water vapour budget of the stratosphere, *Quarterly Journal of the Royal Meteorological Society*, *114*(480), 281–295.

Leahey, D. M., K. Preston, , and M. Strosher (2001), Theoretical and observational assessments of flare efficiencies. (Technical Paper), *Journal of the Air and Waste Management Association*, *51*(12), 1610.

Lebegue, B., et al. (2016), Comparison of nitrous oxide (N_2O) analyzers for high-precision measurements of atmospheric mole fractions, *Atmospheric Measurement Techniques*, *9*(3), 1221–1238.

Lemke, R., L. Liu, V. Baron, S. Malhi, and R. Farrell (2018), Effect of crop and residue type on nitrous oxide emissions from rotations in the semi-arid Canadian prairies, *Canadian Journal of Soil Science*, *98*(3), 508–518, doi:10.1139/cjss-2018-0001.

Lewis, N. S., and D. G. Nocera (2006), Powering the planet: Chemical challenges in solar energy utilization, *Proceedings of the National Academy of Sciences*, *103*(43), 15,729–15,735.

Liang, X.-Z., Y. Wu, R. G. Chambers, D. L. Schmoldt, W. Gao, C. Liu, Y.-A. Liu, C. Sun, and J. A. Kennedy (2017), Determining climate effects on US total agricultural productivity, *Proceedings of the National Academy of Sciences*, *114*(12), E2285–E2292.

Linn, D., and J. Doran (1984), Effect of water-filled pore space on carbon dioxide and nitrous oxide production in tilled and nontilled soils1, *Soil Science Society of America Journal*, *48*, doi:10.2136/sssaj1984.03615995004800060013x.

Lipper, L., et al. (2014), Climate-smart agriculture for food security, *Nature Climate Change*, *4*, 1068, perspective.

Lu, C., and H. Tian (2017), Global nitrogen and phosphorus fertilizer use for agriculture production in the past half century: shifted hot spots and nutrient imbalance, *Earth System Science Data*, *9*(1), 181–192, doi:10.5194/essd-9-181-2017.

Lund, D., et al. (2013), Assessment of the effects of conservation practices on cultivated cropland in the Lower Mississippi River Basin, *Tech. rep.*, USDA NRCS, Washington, DC.

Marinho, E. V. A., R. D. DeLaune, and C. W. Lindau (2004), Nitrous oxide flux from soybeans grown on Mississippi alluvial soil, *Communications in Soil Science and Plant Analysis*, *35*(1-2), 1–8, doi:10.1081/CSS-120027630.

Mays, K. L., P. B. Shepson, B. H. Stirm, A. Karion, C. Sweeney, and K. R. Gurney (2009), Aircraft-based measurements of the carbon footprint of Indianapolis, *Environmental Science & Technology*, *43*(20), 7816–7823.

McElroy, M. B., and Y. X. Wang (2005), Human and animal wastes: Implications for atmospheric N_2O and NO_x, *Global Biogeochemical Cycles*, *19*(2).

McEwen, J. D. N., and M. R. Johnson (2012), Black carbon particulate matter emission factors for buoyancy-driven associated gas flares, *Journal of the Air and Waste Management Association*, *62*(3), 307–321.

McManus, J. B., P. L. Kebabian, and M. S. Zahniser (1995), Astigmatic mirror multipass absorption cells for long-path-length spectroscopy, *Appl. Opt.*, *34*(18), 3336–3348, doi:10.1364/AO.34.003336.

Mehrotra, S., I. Faloona, M. Suard, S. Conley, and M. L. Fischer (2017), Airborne Methane Emission Measurements for Selected Oil and Gas Facilities Across California, *Environ. Sci. Technol.*, *51*(21), 12,981–12,987.

Melillo, J., and G. Yohe (2014), Climate Change Impacts in the United States: The Third National Climate Assessment, *US Global Change Research Program*.

Mesinger, F., et al. (2006), North American Regional Reanalysis, *Bulletin of the American Meteorological Society*, *87*(3), 343–360, doi:10.1175/BAMS-87-3-343, nCEP Reanalysis data provided by the NOAA/OAR/ESRL PSD, Boulder, Colorado, USA, from their Web site at https://www.esrl.noaa.gov/psd/.

Miller, S. M., et al. (2012), Regional sources of nitrous oxide over the United States: Seasonal variation and spatial distribution, *Journal of Geophysical Research: Atmospheres*, *117*(D6), doi:10.1029/2011JD016951.

Mitchell, A. L., et al. (2015), Measurements of methane emissions from natural gas gathering facilities and processing plants: Measurement results, *Environ. Sci. Technol.*, *49*(5), 3219–3227, doi:10.1021/es5052809, pMID: 25668106.

Moffet, R. C., and K. A. Prather (2009), In-situ measurements of the mixing state and optical properties of soot with implications for radiative forcing estimates, *Proceedings of the National Academy of Sciences*, *106*(29), 11,872–11,877.

Monni, S., P. Perälä, and K. Regina (2007), Uncertainty in agricultural CH_4 and N_2O emissions from Finland – possibilities to increase accuracy in emission estimates, *Mitigation and Adaptation Strategies for Global Change*, *12*(4), 545–571, doi:10.1007/s11027-006-4584-4.

Montzka, S., et al. (2003), Controlled substances and other source gases, chapter 1 of the Scientific Assessment of Ozone Depletion: 2002, *Scientific Assessment of Ozone Depletion: 2002*.

Mosier, A., C. Kroeze, C. Nevison, O. Oenema, S. Seitzinger, and O. van Cleemput (1998), Closing the global N_2O budget: nitrous oxide emissions through the agricultural nitrogen cycle, *Nutrient Cycling in Agroecosystems*, *52*(2), 225–248, doi:10.1023/A:1009740530221.

Myhre, G., et al. (2013), Anthropogenic and natural radiative forcing, in *Climate Change 2013: The Physical Science Basis. Contribution of Working Group I to the Fifth Assessment Report of the Intergovernmental Panel on Climate Change*, edited by T. F. Stocker, D. Qin, G.-K. Plattner, M. Tignor, S. K. Allen, J. Doschung, A. Nauels, Y. Xia, V. Bex, and P. M. Midgley, pp. 659–740, Cambridge University Press, Cambridge, UK, doi:10.1017/CBO9781107415324.018.

Nara, H., H. Tanimoto, Y. Tohjima, H. Mukai, Y. Nojiri, and T. Machida (2014), Emissions of methane from offshore oil and gas platforms in Southeast Asia, *Scientific reports*, *4*, 6503.

Nelson, D., J. Shorter, J. McManus, and M. Zahniser (2002), Sub-part-per-billion detection of nitric oxide in air using a thermoelectrically cooled mid-infrared quantum cascade laser spectrometer, *Applied Physics B*, *75*(2), 343–350, doi:10.1007/s00340-002-0979-4.

Nelson, D. D., B. McManus, S. Urbanski, S. Herndon, and M. S. Zahniser (2004), High precision measurements of atmospheric nitrous oxide and methane using thermoelectrically cooled mid-infrared quantum cascade lasers and detectors, *Spectrochimica Acta Part A: Molecular and Bioctroscopy*, *60*(14), 3325 – 3335, doi:https://doi.org/10.1016/j.saa.2004.01.033.

Nevison, C., et al. (2018), Nitrous oxide emissions estimated with the CarbonTracker-Lagrange North American Regional Inversion Framework, *Global Biogeochemical Cycles*, *32*(3), 463–485, doi:10.1002/2017GB005759.

Nisbet, E., and R. Weiss (2010), Top-down versus Bottom-up, *Science*, *328*(5983), 1241–1243, doi:10.1126/science.1189936.

Nisbet, E., et al. (2016), Rising atmospheric methane: 2007–2014 growth and isotopic shift, *Global Biogeochemical Cycles*, *30*(9), 1356–1370.

Nisbet, E. G., E. J. Dlugokencky, and P. Bousquet (2014), Methane on the rise—again, *Science*, *343*(6170), 493–495.

North Dakota State Government (2016), North Dakota Drilling and Production Statistics, `https://www.dmr.nd.gov/oilgas/stats/statisticsvw.asp`.

Novelli, P. C., K. A. Masarie, P. M. Lang, B. D. Hall, R. C. Myers, and J. W. Elkins (2003), Reanalysis of tropospheric CO trends: Effects of the 1997–1998 wildfires, *Journal of Geophysical Research (Atmospheres)*, *108*, 4464, doi:10.1029/2002JD003031.

Nutrien (2018), Nutrien 2018 Fact Book, `https://www.nutrien.com/sites/default/files/uploads/2018-01/Nutrien%20Fact%20Book%202018_1.pdf`.

O'Neill, P., S. Chan, E. Njoku, T. Jackson, and R. Bindlish (2018), SMAP Enhanced L3 Radiometer Global Daily 9 km EASE-Grid Soil Moisture, Version 2 [L3, Passive, Day], doi:10.5067/RFKIZ5QY5ABN, [Accessed 10/31/2018].

Opdyke, M. R., N. E. Ostrom, and P. H. Ostrom (2009), Evidence for the predominance of denitrification as a source of N_2O in temperate agricultural soils based on isotopologue measurements, *Global Biogeochemical Cycles*, *23*(4).

O'Shea, S. J., S. J.-B. Bauguitte, M. W. Gallagher, D. Lowry, and C. J. Percival (2013), Development of a cavity-enhanced absorption spectrometer for airborne measurements of CH_4 and CO_2, *Atmospheric Measurement Techniques*, *6*(5), 1095–1109, doi:10.5194/amt-6-1095-2013.

O'Shea, S. J., et al. (2014), Methane and carbon dioxide fluxes and their regional scalability for the European Arctic wetlands during the MAMM project in summer 2012, *Atmospheric Chemistry and Physics*, *14*(23), 13,159–13,174, doi:10.5194/acp-14-13159-2014.

Padgitt, M., D. Newton, R. Penn, and C. Sandretto (2000), Production Practices for Major Crops in U.S. Agriculture, 1990-97, *Statistical Bulletin 262287*, United States Department of Agriculture, Economic Research Service.

Parkin, T., R. Venterea, and S. Hargreaves (2012), Calculating the detection limits of chamber-based soil greenhouse gas flux measurements, *Journal of environmental quality*, *41*, 705–15, doi:10.2134/jeq2011.0394.

Parkin, T. B., and T. C. Kaspar (2006), Nitrous oxide emissions from corn-soybean systems in the Midwest, *J. Environ. Qual.*, *35*(4), 1496–1506.

Parry, M. L., C. Rosenzweig, A. Iglesias, M. Livermore, and G. Fischer (2004), Effects of climate change on global food production under SRES emissions and socio-economic scenarios, *Global environmental change*, *14*(1), 53–67.

Pattey, E., G. Edwards, R. Desjardins, D. Pennock, W. Smith, B. Grant, and J. MacPherson (2007), Tools for quantifying N_2O emissions from agroecosystems, *Agricultural and Forest Meteorology*, *142*(2), 103 – 119, doi:https://doi.org/10.1016/j.agrformet.2006.05.013, the Contribution of Agriculture to the State of Climate.

Pattey, E., L. G. Blackburn, I. B. Strachan, R. Desjardins, and D. Dow (2008), Spring thaw and growing season N_2O emissions from a field planted with edible peas and a cover crop, *Canadian Journal of Soil Science*, *88*(2), 241–249, doi:10.4141/CJSS06035.

Peischl, J., et al. (2015a), Quantifying atmospheric methane emissions from the Haynesville, Fayetteville, and northeastern Marcellus shale gas production regions, *Journal of Geophysical Research: Atmospheres*, *120*(5), 2119–2139, doi:10.1002/2014JD022697.

Peischl, J., et al. (2015b), Quantification of methane emissions from oil and natural gas extraction regions in the Central/Western US and comparison to previous studies, in *AGU Fall Meeting Abstracts*.

Peischl, J., et al. (2016), Quantifying atmospheric methane emissions from oil and natural gas production in the Bakken shale region of North Dakota, *Journal of Geophysical Research: Atmospheres*, pp. n/a–n/a, doi:10.1002/2015JD024631.

Pennock, D., R. Farrell, R. Desjardins, E. Pattey, and J. I. MacPherson (2005), Upscaling chamber-based measurements of N_2O emissions at snowmelt, *Canadian Journal of Soil Science*, *85*(1), 113–125, doi:10.4141/S04-040.

Pinker, S. (2018), *Enlightenment Now: The Case for Reason, Science, Humanism, and Progress*, Penguin Books.

Pitt, J. R., et al. (2016), The development and evaluation of airborne in situ N_2O and CH_4 sampling using a quantum cascade laser absorption spectrometer (QCLAS), *Atmospheric Measurement Techniques*, *9*(1), 63–77, doi:10.5194/amt-9-63-2016.

Popp, A., H. Lotze-Campen, and B. Bodirsky (2010), Food consumption, diet shifts and associated non-CO_2 greenhouse gases from agricultural production, *Global Environmental Change*, *20*(3), 451–462.

Portmann, R., J. Daniel, and A. Ravishankara (2012), Stratospheric ozone depletion due to nitrous oxide: influences of other gases, *Philosophical Transactions of the Royal Society B: Biological Sciences*, *367*(1593), 1256–1264.

Prather, M., G. Flato, P. Friedlingstein, C. Jones, J. Lamarque, H. Liao, and P. Rasch (2013), Annex II: Climate System Scenario Tables, in *Climate Change 2013: The Physical Science Basis. Contribution of Working Group I to the Fifth Assessment Report of the Intergovernmental Panel on Climate Change*, edited by T. F. Stocker, D. Qin, G.-K. Plattner, M. Tignor, S. K. Allen, J. Doschung, A. Nauels, Y. Xia, V. Bex, and P. M. Midgley, Cambridge University Press, Cambridge, UK and New York, NY, USA.

Ramana, M., V. Ramanathan, Y. Feng, S. Yoon, S. Kim, G. Carmichael, and J. Schauer (2010), Warming influenced by the ratio of black carbon to sulphate and the black-carbon source, *Nature Geoscience*, *3*(8), 542.

Ramanathan, V., and G. Carmichael (2008), Global and regional climate changes due to black carbon, *Nature geoscience*, *1*(4), 221.

Rannik, U., et al. (2015), Intercomparison of fast response commercial gas analysers for nitrous oxide flux measurements under field conditions, *Biogeosciences*, *12*(2), 415–432, doi:10.5194/bg-12-415-2015.

Rapson, T. D., and H. Dacres (2014), Analytical techniques for measuring nitrous oxide, *TrAC Trends in Analytical Chemistry*, *54*, 65 – 74, doi:https://doi.org/10.1016/j.trac.2013.11.004.

Ravishankara, A. R., J. S. Daniel, and R. W. Portmann (2009), Nitrous oxide (N_2O): The dominant ozone-depleting substance emitted in the 21st century, *Science*, *326*(5949), 123–125, doi:10.1126/science.1176985.

Reay, D. S., E. A. Davidson, K. A. Smith, P. Smith, J. M. Melillo, F. Dentener, and P. J. Crutzen (2012), Global agriculture and nitrous oxide emissions, *Nature Climate Change*, *2*(6), 410–416, doi:10.1038/nclimate1458.

Reay, D. S., P. Smith, T. R. Christensen, R. H. James, and H. Clark (2018), Methane and global environmental change, *Annual Review of Environment and Resources*, *43*(1), 165–192, doi:10.1146/annurev-environ-102017-030154.

Rella, C. W., et al. (2013), High accuracy measurements of dry mole fractions of carbon dioxide and methane in humid air, *Atmospheric Measurement Techniques*, *6*(3), 837–860, doi:10.5194/amt-6-837-2013.

Richter, D., P. Weibring, J. G. Walega, and A. Fried (2013), Airborne atmospheric laser spectroscopy, in *CLEO: Applications and Technology*, pp. ATh1I–3, Optical Society of America.

Rigby, M., et al. (2017), Role of atmospheric oxidation in recent methane growth, *Proceedings of the National Academy of Sciences*, *114*(21), 5373–5377.

Ritchie, H., and M. Roser (2019), Energy production & changing energy sources, *Our World in Data*, https://ourworldindata.org/energy-production-and-changing-energy-sources.

Römkens, M., H. Selim, H. Scott, R. Phillips, and F. Whisler (1986), Physical characteristics of soils in the Southern Region: Captina, Gigger, Grenada, Loring, Olivier and Sharkey series, *Southern Cooperative Series Bulletin*, *264*.

Roser, M. (2019), Life expectancy, *Our World in Data*, https://ourworldindata.org/life-expectancy.

Rosling, H., O. Rosling, and A. R. Rönnlund (2018), *Factfulness: Ten Reasons We're Wrong about the World–and why Things are Better Than You Think*, St Martin's Press.

Rothman, L. S., et al. (2013), The HITRAN2012 molecular spectroscopic database, *Journal of Quantitiative Spectroscopy and Radiative Transfer*, *130*, 4–50, doi:10.1016/j.jqsrt.2013.07.002.

Rudolph, J. (1995), The tropospheric distribution and budget of ethane, *Journal of Geophysical Research: Atmospheres*, *100*(D6), 11,369–11,381, doi:10.1029/95JD00693.

Ruser, R., H. Flessa, R. Russow, G. Schmidt, F. Buegger, and J. Munch (2006), Emission of N_2O, N_2 and CO_2 from soil fertilized with nitrate: effect of compaction, soil moisture and rewetting, *Soil Biology and Biochemistry*, *38*(2), 263 – 274, doi:https://doi.org/10.1016/j.soilbio.2005.05.005.

Santoni, G. W., et al. (2014), Evaluation of the airborne quantum cascade laser spectrometer (QCLS) measurements of the carbon and greenhouse gas suite - CO_2, CH_4, N_2O, and CO - during the CalNex and HIPPO campaigns, *Atmospheric Measurement Techniques*, *7*(6), 1509–1526, doi:10.5194/amt-7-1509-2014.

Saunois, M., et al. (2016), The global methane budget 2000–2012, *Earth System Science Data*, *8*(2), 697–751.

Scaroni, A. E., S. Ye, C. W. Lindau, and J. A. Nyman (2014), Nitrous oxide emissions from soils in Louisiana's Atchafalaya River Basin, *Wetlands*, *34*(3), 545–554, doi:10.1007/s13157-014-0521-6.

Schaefer, H., et al. (2016), A 21st-century shift from fossil-fuel to biogenic methane emissions indicated by $^{13}CH_4$, *Science*, *352*(6281), 80–84.

Schindlbacher, A., S. Zechmeister-Boltenstern, and K. Butterbach-Bahl (2004), Effects of soil moisture and temperature on NO, NO_2, and N_2O emissions from European forest soils, *Journal of Geophysical Research: Atmospheres*, *109*(D17), doi:10.1029/2004JD004590.

Schmidt, T. M., and C. Waldron (2015), Microbial diversity in soils of agricultural landscapes and its relation to ecosystem function, *The ecology of agricultural landscapes: long-term research on the path to sustainability. Oxford University Press, New York*, pp. 135–157.

Schwarz, J. P., J. S. Holloway, J. M. Katich, S. McKeen, E. A. Kort, M. L. Smith, T. B. Ryerson, C. Sweeney, and J. Peischl (2015), Black carbon emissions from the Bakken oil and gas development region, *Environmental Science & Technology Letters*, *2*(10), 281–285, doi:10.1021/acs.estlett.5b00225.

Schwarz, J. P., et al. (2010), The detection efficiency of the Single Particle Soot Photometer, *Aerosol Science and Technology*, *44*(8), 612–628, doi:10.1080/02786826.2010.481298.

Schwietzke, S., W. M. Griffin, H. S. Matthews, and L. M. Bruhwiler (2014), Natural gas fugitive emissions rates constrained by global atmospheric methane and ethane, *Environmental science & technology*, *48*(14), 7714–7722.

Scott, H. D., J. A. Ferguson, L. Hanson, T. Fugitt, and E. Smith (1998), Agricultural water management in the Mississippi Delta Region of Arkansas.

Selim, H., B. Davidoff, H. Fluhler, and R. Schulin (1987), Variability of in situ measured mechanical impedance for a fragipan soil, *Soil science*, *144*(6), 442–452.

Shcherbak, I., N. Millar, and G. P. Robertson (2014), Global metaanalysis of the nonlinear response of soil nitrous oxide (N_2O) emissions to fertilizer nitrogen, *Proceedings of the National Academy of Sciences*, doi:10.1073/pnas.1322434111.

Shindell, D., et al. (2012), Simultaneously mitigating near-term climate change and improving human health and food security, *Science*, *335*(6065), 183–189.

Shindell, D. T., G. Faluvegi, D. M. Koch, G. A. Schmidt, N. Unger, and S. E. Bauer (2009), Improved attribution of climate forcing to emissions, *Science*, *326*(5953), 716–718, doi:10.1126/science.1174760.

Signor, D., and C. E. P. Cerri (2013), Nitrous oxide emissions in agricultural soils: a review, *Pesquisa AgropecuÃ¡ria Tropical*, *43*, 322 – 338, doi:10.1590/S1983-40632013000300014.

Simpson, I. J., M. P. S. Andersen, S. Meinardi, L. Bruhwiler, N. J. Blake, D. Helmig, F. S. Rowland, and D. R. Blake (2012), Long-term decline of global atmospheric ethane concentrations and implications for methane, *Nature*, *488*(7412), 490.

Singh, H. B., and P. L. Hanst (1981), Peroxyacetyl nitrate (PAN) in the unpolluted atmosphere: An important reservoir for nitrogen oxides, *Geophysical Research Letters*, *8*(8), 941–944.

Smil, V. (2011), Nitrogen cycle and world food production, *World Agriculture*, *2*(1), 9–13.

Smith, C. J., W. Wang, and G. Wysocki (2013), Real-time calibration of laser absorption spectrometer using spectral correlation performed with an in-line gas cell, *Optics express*, *21*(19), 22,488–22,503.

Smith, K., P. Thomson, H. Clayton, I. Mctaggart, and F. Conen (1998), Effects of temperature, water content and nitrogen fertilisation on emissions of nitrous oxide by soils, *Atmospheric Environment*, *32*(19), 3301 – 3309, doi:https://doi.org/10.1016/S1352-2310(97)00492-5.

Smith, K. A., T. Ball, F. Conen, K. E. Dobbie, J. Massheder, and A. Rey (2003), Exchange of greenhouse gases between soil and atmosphere: interactions of soil physical factors and biological processes, *European Journal of Soil Science*, *54*(4), 779–791, doi:10.1046/j.1351-0754.2003.0567.x.

Smith, M. L., E. A. Kort, A. Karion, C. Sweeney, S. C. Herndon, and T. I. Yacovitch (2015), Airborne ethane observations in the Barnett Shale: Quantification of ethane flux and attribution of methane emissions, *Environmental Science & Technology*, *49*(13), 8158–8166, doi:10.1021/acs.est.5b00219, pMID: 26148554.

Smith, M. L., et al. (2017a), Airborne quantification of methane emissions over the Four Corners Region, *Environmental Science & Technology*, *51*(10), 5832–5837, doi:10.1021/acs.est.6b06107, pMID: 28418663.

Smith, P., et al. (2014), Agriculture, forestry and other land use (AFOLU), in *Climate Change 2014: Mitigation of Climate Change. Contribution of Working Group III to the Fifth Assessment Report of the Intergovernmental Panel on Climate Change*, Cambridge University Press.

Smith, T. M., A. L. Goodkind, T. Kim, R. E. O. Pelton, K. Suh, and J. Schmitt (2017b), Subnational mobility and consumption-based environmental accounting of US corn in animal protein and ethanol supply chains, *Proceedings of the National Academy of Sciences*, *114*(38), E7891–E7899, doi:10.1073/pnas.1703793114.

Snipes, C. E., L. P. Evans, D. H. Poston, and S. P. Nichols (2004), *Agricultural Practices of the Mississippi Delta*, chap. 4, pp. 43–60, American Chemical Society, doi:10.1021/bk-2004-0877.ch004.

Soane, B. (1990), The role of organic matter in soil compactibility: A review of some practical aspects, *Soil and Tillage Research*, *16*(1), 179 – 201, doi:https://doi.org/10.1016/0167-1987(90)90029-D, a Tribute to Prof. IR. H. Kuipers.

Speight, J. (2007), Liquid fuels from natural gas, *Handbook of Alternative Fuel Technologies*, p. 153.

Stohl, A., Z. Klimont, S. Eckhardt, K. Kupiainen, V. P. Shevchenko, V. M. Kopeikin, and A. N. Novigatsky (2013), Black carbon in the Arctic: the underestimated role of gas flaring and residential combustion emissions, *Atmospheric Chemistry and Physics*, *13*(17).

Stolarski, R. S., A. R. Douglass, L. D. Oman, and D. W. Waugh (2015), Impact of future nitrous oxide and carbon dioxide emissions on the stratospheric ozone layer, *Environmental Research Letters*, *10*(3), 034,011.

Stuart, B. (2000), Infrared spectroscopy, *Kirk-Othmer Encyclopedia of Chemical Technology*, pp. 1–18.

Subramanian, R., et al. (2015), Methane emissions from natural gas compressor stations in the transmission and storage sector: Measurements and comparisons with the EPA Greenhouse Gas Reporting Program protocol, *Environ. Sci. Technol.*, *49*(5), 3252–3261, doi:10.1021/es5060258, pMID: 25668051.

Tanaka, T., et al. (2016), Two-year comparison of airborne measurements of CO_2 and CH_4 with GOSAT at Railroad Valley, Nevada, *IEEE Transactions on Geoscience and Remote Sensing*, *54*(8), 4367–4375.

Tans, P. P., A. M. Crotwell, and K. W. Thoning (2017), Abundances of isotopologues and calibration of CO_2 greenhouse gas measurements, *Atmospheric Measurement Techniques*, *10*(7), 2669–2685, doi:10.5194/amt-10-2669-2017.

TFI (2017), 2017 State of the Fertilizer Industry.

The World Bank (2016a), Access to electricity (% of population), `https://data.worldbank.org/indicator/EG.ELC.ACCS.ZS`.

The World Bank (2016b), Life expectancy at birth, total (years), `https://data.worldbank.org/indicator/SP.DYN.LE00.IN`.

The World Bank (2016c), Zero Routine Flaring by 2030, `http://www.worldbank.org/en/programs/zero-routine-flaring-by-2030`.

The World Bank (2017), Global Gas Flaring Reduction Partnership (GGFR), `http://www.worldbank.org/en/programs/gasflaringreduction`.

Thompson, R. L., et al. (2014), Nitrous oxide emissions 1999 to 2009 from a global atmospheric inversion, *Atmospheric Chemistry and Physics*, *14*(4), 1801–1817, doi:10.5194/acp-14-1801-2014.

Tian, H., et al. (2012), Century-scale responses of ecosystem carbon storage and flux to multiple environmental changes in the southern United States, *Ecosystems*, *15*(4), 674–694.

Tian, H., et al. (2015), Global methane and nitrous oxide emissions from terrestrial ecosystems due to multiple environmental changes, *Ecosystem Health and Sustainability*, *1*(1), 1–20, doi:10.1890/EHS14-0015.1.

Tian, H., et al. (2018), Global soil nitrous oxide emissions since the preindustrial era estimated by an ensemble of terrestrial biosphere models: Magnitude, attribution, and uncertainty, *Global Change Biology*, *0*(0), doi:10.1111/gcb.14514.

Tilman, D., and M. Clark (2014), Global diets link environmental sustainability and human health, *Nature*, *515*, 518, doi:https://doi.org/10.1038/nature13959, article.

Trainer, M., B. Ridley, M. Buhr, G. Kok, J. Walega, G. Hübler, D. Parrish, and F. Fehsenfeld (1995), Regional ozone and urban plumes in the southeastern United States: Birmingham, a case study, *Journal of Geophysical Research: Atmospheres*, *100*(D9), 18,823–18,834.

Turnbull, J., et al. (2011), Assessment of fossil fuel carbon dioxide and other anthropogenic trace gas emissions from airborne measurements over Sacramento, California in spring 2009, *Atmospheric Chemistry and Physics*, *11*(2), 705–721.

Turner, A. J., C. Frankenberg, P. O. Wennberg, and D. J. Jacob (2017), Ambiguity in the causes for decadal trends in atmospheric methane and hydroxyl, *Proceedings of the National Academy of Sciences*, *114*(21), 5367–5372.

Turner, A. J., C. Frankenberg, and E. A. Kort (2019), Interpreting contemporary trends in atmospheric methane, *Proceedings of the National Academy of Sciences*, doi:10.1073/pnas.1814297116.

Turner, D. A., D. Chen, I. E. Galbally, R. Leuning, R. B. Edis, Y. Li, K. Kelly, and F. Phillips (2008), Spatial variability of nitrous oxide emissions from an Australian irrigated dairy pasture, *Plant and Soil*, *309*(1), 77–88, doi:10.1007/s11104-008-9639-8.

United Nations (2017), World Population Prospects: The 2017 Revision, Key Findings and Advance Tables, eSA/P/WP/248.

USDA (2017), USDA National Agricultural Statistics Service Cropland Data Layer, Published crop-specific data layer [Online]. Available at `https://nassgeodata.gmu.edu/CropScape/`. Last accessed October 2018.

USDA ARS (2012), Lower Mississippi River Basin, *Tech. rep.*, United States Department of Agriculture, Agricultural Research Service.

USDA ARS (2014), LMRB, `https://ltar.ars.usda.gov/sites/lmrb/`.

USDA NASS (2017a), May 8, 2017 Crop Progress Report, `https://downloads.usda.library.cornell.edu/usda-esmis/files/8336h188j/jw827d33p/kh04dr233/CropProg-05-08-2017.pdf`.

USDA NASS (2017b), May 15, 2017 Crop Progress Report, `https://downloads.usda.library.cornell.edu/usda-esmis/files/8336h188j/k0698890n/wp988m39m/CropProg-05-15-2017.pdf`.

USGS (2018), NITROGEN (FIXED)—AMMONIA, `https://minerals.usgs.gov/minerals/pubs/commodity/nitrogen/mcs-2018-nitro.pdf`.

Vaughn, T. L., et al. (2017), Comparing facility-level methane emission rate estimates at natural gas gathering and boosting stations, *Elem Sci Anth*, *5*(0), 71, doi:10.1525/elementa.257.

Wang, Q., X. Chen, A. N. Jha, and H. Rogers (2014a), Natural gas from shale formation–the evolution, evidences and challenges of shale gas revolution in United States, *Renewable and Sustainable Energy Reviews*, *30*, 1–28.

Wang, Q., et al. (2014b), Global budget and radiative forcing of black carbon aerosol: Constraints from pole-to-pole (HIPPO) observations across the Pacific, *Journal of Geophysical Research: Atmospheres*, *119*(1), 195–206.

Werle, P. (2011), Accuracy and precision of laser spectrometers for trace gas sensing in the presence of optical fringes and atmospheric turbulence, *Applied Physics B*, *102*(2), 313–329.

Weyant, C. L., P. B. Shepson, R. Subramanian, M. O. Cambaliza, A. Heimburger, D. McCabe, E. Baum, B. H. Stirm, and T. C. Bond (2016), Black carbon emissions from associated natural gas flaring, *Environ. Sci. Technol.*

White, W., J. Anderson, D. Blumenthal, R. Husar, N. Gillani, J. Husar, and W. Wilson (1976), Formation and transport of secondary air pollutants: ozone and aerosols in the St. Louis urban plume, *Science*, *194*(4261), 187–189, doi: 10.1126/science.959846.

WMO, W. (2015), 18th WMO/IAEA meeting on carbon dioxide, other greenhouse gases and related tracers measurement techniques (GGMT-2015), *GAW Report-No. 229*.

Wofsy, S. C. (2011), HIAPER Pole-to-Pole Observations (HIPPO): fine-grained, global-scale measurements of climatically important atmospheric gases and aerosols, *Philosophical Transactions of the Royal Society of London A: Mathematical, Physical and Engineering Sciences*, *369*(1943), 2073–2086, doi:10.1098/rsta.2010.0313.

Wollenberg, E., et al. (2016), Reducing emissions from agriculture to meet the 2 C target, *Global Change Biology*, *22*(12), doi:10.1111/gcb.13340.

Worden, J. R., A. A. Bloom, S. Pandey, Z. Jiang, H. M. Worden, T. W. Walker, S. Houweling, and T. Röckmann (2017), Reduced biomass burning emissions reconcile conflicting estimates of the post-2006 atmospheric methane budget, *Nature communications*, *8*(1), 2227.

Wuebbles, D. J., and K. Hayhoe (2002), Atmospheric methane and global change, *Earth-Science Reviews*, *57*(3-4), 177–210.

Xiang, B., et al. (2013), Nitrous oxide (N_2O) emissions from California based on 2010 CalNex airborne measurements, *Journal of Geophysical Research: Atmospheres*, *118*(7), 2809–2820, doi:10.1002/jgrd.50189.

Xiao, Y., J. A. Logan, D. J. Jacob, R. C. Hudman, R. Yantosca, and D. R. Blake (2008), Global budget of ethane and regional constraints on U.S. sources, *Journal of Geophysical Research: Atmospheres*, *113*(D21), doi:10.1029/2007JD009415.

Yacovitch, T. I., et al. (2014), Demonstration of an ethane spectrometer for methane source identification, *Environ. Sci. Technol.*, *48*(14), 8028–8034, doi: 10.1021/es501475q, pMID: 24945706.

Yuan, B., et al. (2015), Airborne flux measurements of methane and volatile organic compounds over the Haynesville and Marcellus shale gas production regions, *Journal of Geophysical Research: Atmospheres*, *120*(12), 6271–6289, doi: 10.1002/2015JD023242, 2015JD023242.

Zannetti, P. (1990), *Air Pollution Modeling*, 1 ed., Springer US, New York City, NY.

Zavala-Araiza, D., et al. (2015), Reconciling divergent estimates of oil and gas methane emissions, *Proceedings of the National Academy of Sciences*, *112*(51), 15,597–15,602.

Zhang, J., C. Müller, and Z. Cai (2015), Heterotrophic nitrification of organic n and its contribution to nitrous oxide emissions in soils, *Soil Biology and Biochemistry*, *84*, 199 – 209, doi:https://doi.org/10.1016/j.soilbio.2015.02.028.

Zhang, L., G. Tian, J. Li, and B. Yu (2014), Applications of absorption spectroscopy using quantum cascade lasers, *Applied spectroscopy*, *68*(10), 1095–1107.

Zhang, W.-f., et al. (2013), New technologies reduce greenhouse gas emissions from nitrogenous fertilizer in China, *Proceedings of the National Academy of Sciences*, *110*(21), 8375–8380, doi:10.1073/pnas.1210447110.

Zhao, C. L., and P. P. Tans (2006), Estimating uncertainty of the WMO mole fraction scale for carbon dioxide in air, *Journal of Geophysical Research: Atmospheres*, *111*(D8), doi:10.1029/2005JD006003.

Zhao, C. L., P. P. Tans, and K. W. Thoning (1997), A high precision manometric system for absolute calibrations of CO_2 in dry air, *Journal of Geophysical Research: Atmospheres*, *102*(D5), 5885–5894, doi:10.1029/96JD03764.